HARTREE-FOCK STUDIES OF QUANTUM HALL STATES IN GRAPHENE

Braden R. Feshami

Submitted to the faculty of the University Graduate School

in partial fulfillment of the requirements

for the degree

Doctor of Philosophy

in the Department of Physics,

Indiana University

August 2020

Accepted by the Graduate Faculty, Indiana University, in partial fulfillment of the requirements for the degree of Doctor of Philosophy.

Doctoral Committee

Herbert Fertig, Ph.D. (Chair)

Charles Horowitz, Ph.D.

Babak Seradjeh, Ph.D.

Shixiong Zhang, Ph.D.

July 24, 2020

Acknowledgments

First and foremost, I would like to thank my advisor, Herbert Fertig, for his kindness and overwhelming support over the years. He has kindled my evergrowing interest in the fascinating world of graphene and condensed matter physics in general. Under his guidance, I have learned a tremendous amount about what it means to be a good researcher. He has helped me overcome many difficult obstacles along the way. I could not have hoped for a better mentor. Thank you, Herb.

I thank the faculty and staff of the Indiana University Department of Physics for their guidance and support during my time in Bloomington, as well as the many great friends I have made in this wonderful town. I especially thank Andrew and Blake for their support and friendship over the years.

I would like to thank my high school physics teacher, Tom Jennings, for inspiring me to pursue a higher education in physics. I hope that I can pass along that same inspiration to future generations.

Without the love and support of my family, I could not have come this far. I thank my mother and father for their encouragement throughout my life.

Finally, I thank my wife, Coley, for keeping me balanced and focused. Her love and inspiration have been instrumental in completing this work.

Braden R. Feshami

HARTREE-FOCK STUDIES OF QUANTUM HALL STATES IN GRAPHENE

Recent experiments involving tilted graphene samples in the quantum Hall regime have shown strong evidence of a continuous phase transition in the $\nu = 0$ bulk state. The origins of this transition are rooted in SU(4) symmetry-breaking interactions. In this work, we present a model with microscopic interactions that supports such a transition. The model is studied within a self-consistent Hartree-Fock analysis. We find that the full set of possible symmetry-breaking terms in the interactions are realized by incorporating an active window of non-zero Landau levels in the Hartree-Fock state. Additionally, the model is studied away from integer filling, in which Skyrme crystals supporting spin textures are stabilized by long range Coulomb interactions. We explore how these textures evolve with the system parameters, and construct a phase diagram within the space of the Zeeman strength and filling factor.

Herbert Fertig, Ph.D. (Chair)

Charles Horowitz, Ph.D.

Babak Seradjeh, Ph.D.

Shixiong Zhang, Ph.D.

Contents

Chapter 1

Introduction

Graphene, despite its initial discovery nearly 15 years ago, continues to be a platform for both theoretical and experimental research. The material is composed entirely of carbon atoms, which form a honeycomb lattice that is two-dimensional (2D) in the sense that the lattice itself is only one atom layer thick. Each carbon atom has six electrons, two of which completely fill the inner 1s shell. In the presence of other carbon atoms, three of the remaining electrons bond, covalently, through sp^2 hybridization, and give rise to the planar geometry of the honeycomb lattice. This kind of hybridization is a basic component in the formation of graphitic allotropes, like graphite and carbon nanotubes. The last electron occupies the $2p_z$ orbital, which is perpendicular to the plane, and is responsible for many of the electronic properties of graphene at low energies.

Two common techniques for isolating graphene is exfoliation and epitaxy, the former being the technique originally employed to synthesize a sample; Geim and Novoselov used adhesive tape to repeatedly peel back layers of graphite. The flakes were then deposited on silicon substrates, and analyzed using methods such as electron microscopy. An early study by Geim's group showed that the carrier density could be tuned by applying a gate voltage to the sample [1]. This property of an electric field effect is a key component in designing electronic devices. In more recent fabrication techniques, boron nitride has been used as a substrate for graphene, leading to higher electron mobilities than the SiO_2 substrates [2]. Because of its high carrier mobilities, among other properties, graphene has tremendous applications in electronics.

1.1 Graphene lattice

The honeycomb lattice is constructed from two independent triangular sublattices, illustrated in Fig. 1.1a. Each sublattice, denoted A and B, form a Bravais lattice, whereas the underlying

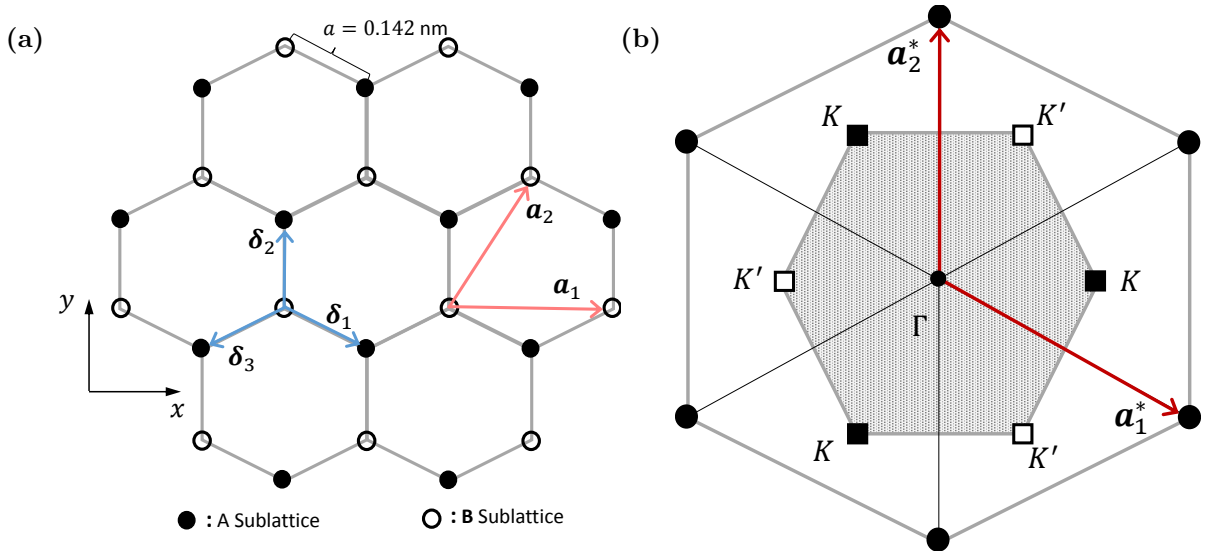

Figure 1.1: (a) Honeycomb lattice for graphene. The hexagonal lattice is constructed from two triangular Bravais sublattices, which are spanned by the vectors $\boldsymbol{a}_1$ and $\boldsymbol{a}_2$. (b) Reciprocal lattice of the triangular lattice. The shaded region denotes the first Brillouin zone, and the black and white squares denote the inequivalent K and K′ points, respectively.

honeycomb lattice does not. Atoms in one sublattice (A) have 3 nearest neighbor (NN) pairs in the other sublattice (B), with a spacing between pairs of $a = 0.142$ nm. The vectors $\boldsymbol{\delta}_i$ connect atoms from one sublattice to another.

$$\boldsymbol{\delta}_1 = \frac{a}{2}(\sqrt{3}\hat{\mathbf{x}} + \hat{\mathbf{y}}) \ , \ \boldsymbol{\delta}_2 = \frac{a}{2}(-\sqrt{3}\hat{\mathbf{x}} + \hat{\mathbf{y}}) \ , \ \boldsymbol{\delta}_3 = -a\hat{\mathbf{y}} \tag{1.1}$$

The primitive lattice vectors, which span the triangular Bravais lattice, are chosen to be

$$\boldsymbol{a}_1 = \sqrt{3}a\hat{\mathbf{x}} \text{ and } \boldsymbol{a}_2 = \frac{\sqrt{3}a}{2}(\hat{\mathbf{x}} + \sqrt{3}\hat{\mathbf{y}}). \tag{1.2}$$

The area of the unit cell is $A_c = \sqrt{3}\tilde{a}^2/2$, where $\tilde{a} = \sqrt{3}a = 0.24$ nm is the lattice spacing. Bravais lattice vectors are constructed by taking linear combinations of the primitive lattice vectors: $\boldsymbol{R} = n_1\boldsymbol{a}_1 + n_2\boldsymbol{a}_2$, with integers $n_1, n_2 \in \mathbb{Z}$.

The reciprocal lattice is spanned by the vectors

$$\boldsymbol{a}_1^* = \frac{2\pi}{\sqrt{3}a}(\hat{\mathbf{x}} - \frac{\hat{\mathbf{y}}}{\sqrt{3}}) \text{ and } \boldsymbol{a}_2^* = \frac{4\pi}{3a}\hat{\mathbf{y}}, \tag{1.3}$$

which form the reciprocal lattice vectors, or, equivalently, wave vectors $\boldsymbol{k} = m_1\boldsymbol{a}_1^* + m_2\boldsymbol{a}_2^*$ with $m_1, m_2 \in \mathbb{Z}$. These basis vectors satisfy the condition $\boldsymbol{a}_i \cdot \boldsymbol{a}_j^* = 2\pi\delta_{i,j}$. The shaded hexagon in Fig. 1.1b shows the first Brillouin zone (FBZ). Locations of two inequivalent points, K and K$'$, on the corners of the FBZ are given by

$$\boldsymbol{K} = \frac{4\pi}{3\sqrt{3}a}\hat{\mathbf{x}} \text{ and } \boldsymbol{K}' = -\frac{4\pi}{3\sqrt{3}a}\hat{\mathbf{x}}. \tag{1.4}$$

The other K (K$'$) points in the FBZ can be connected to $\boldsymbol{K}$ ($\boldsymbol{K}'$) through translations of reciprocal lattice vectors. As we will see in the next section, the low energy excitations occur around these six points.

1.2 Single particle tight-binding model

In this section, we will calculate the energy dispersion for non-interacting electrons in the context of a tight-binding model. The model will include only NN hoppings, and exclude spin labels for simplicity. The tight-binding Hamiltonian in second quantization is

$$H_{tb} = t\sum_{\boldsymbol{R},\boldsymbol{R}'}\left[c_A^\dagger(\boldsymbol{R})c_B(\boldsymbol{R}') + \text{h.c.}\right] = t\sum_{\boldsymbol{R},j}\left[c_A^\dagger(\boldsymbol{R})c_B(\boldsymbol{R}+\boldsymbol{\delta_j}) + \text{h.c}\right], \tag{1.5}$$

where the operator $c_s(\boldsymbol{R})$ removes an electron on site $s \in A, B$, and $t \simeq -3$ eV[3,4] is the hopping amplitude. The operators satisfy the usual anti-commutation relations,

$$\left\{c_s(\boldsymbol{R}), c_s^\dagger(\boldsymbol{R}')\right\} = \delta_{\boldsymbol{R},\boldsymbol{R}'} \text{ and } \left\{c_s(\boldsymbol{k}), c_s^\dagger(\boldsymbol{k}')\right\} = \delta_{\boldsymbol{k},\boldsymbol{k}'}, \tag{1.6}$$

and their Fourier transform is

$$c_s(\boldsymbol{R}) = \frac{1}{\sqrt{N_s}}\sum_{\boldsymbol{k}\in\text{FBZ}} c_s(\boldsymbol{k})e^{i\boldsymbol{k}\cdot\boldsymbol{R}}, \tag{1.7}$$

where N_s is the number of Bravais lattice sites. Inserting eq. (1.7) into eq. (1.5), and noting $\frac{1}{N_s}\sum_{\boldsymbol{R}} e^{i(\boldsymbol{k}-\boldsymbol{k}')\cdot\boldsymbol{R}} = \delta_{\boldsymbol{k},\boldsymbol{k}'}$, the tight-binding Hamiltonian becomes

$$\begin{aligned} H_{tb} &= t\sum_{\boldsymbol{k},j}\left[e^{i\boldsymbol{k}\cdot\boldsymbol{\delta}_j}c_A^\dagger(\boldsymbol{k})c_B(\boldsymbol{k}) + \text{h.c}\right] \\ &= \sum_{\boldsymbol{k}}\psi^\dagger(\boldsymbol{k})h(\boldsymbol{k})\psi(\boldsymbol{k}). \end{aligned} \tag{1.8}$$

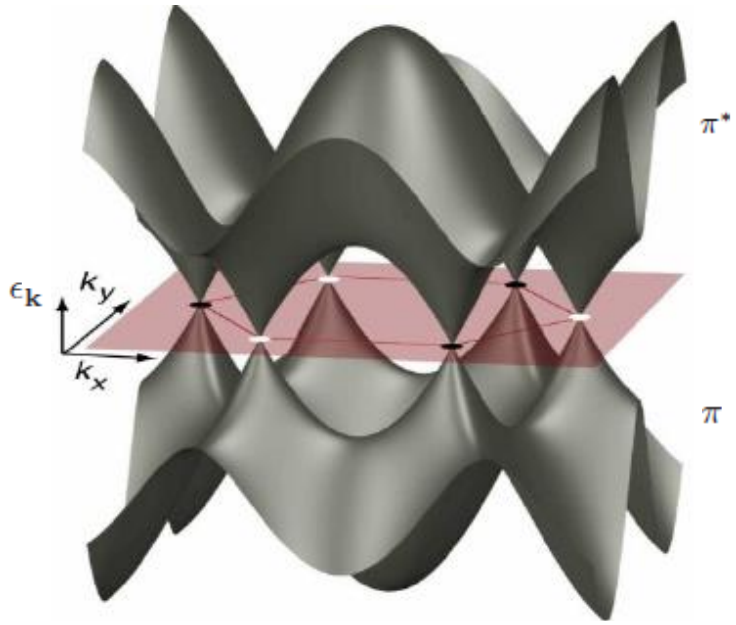

Figure 1.2: Energy dispersion for graphene in the tight binding model with nearest neighbor hopping only. The two bands, π and π^*, touch only at the Dirac points, which coincide with the K and K$'$ points. Image reproduced from Ref. [5].

In eq. (1.8), $\psi(\boldsymbol{k}) = \big(c_A(\boldsymbol{k}), c_B(\boldsymbol{k})\big)^T$, and

$$h(\boldsymbol{k}) = t \begin{pmatrix} 0 & f^*(\boldsymbol{k}) \\ f(\boldsymbol{k}) & 0 \end{pmatrix} \tag{1.9}$$

is the Bloch Hamiltonian with $f(\boldsymbol{k}) = \sum_j e^{i\boldsymbol{k}\cdot\boldsymbol{\delta}_j} = e^{-iak_y}\big[1 + 2e^{i(3ak_y/2)}\cos(\sqrt{3}ak_x/2)\big]$. Notice that $h(\boldsymbol{k}) = h^*(-\boldsymbol{k})$, so that the effective Hamiltonian respects time reversal symmetry.

The eigenvalues, $\epsilon^\lambda_{\boldsymbol{k}}$, give the dispersion energy for the π electrons, which occupy the $2p_z$ orbital. Since there are two atoms per unit cell, there will be two eigenvalues, and hence two energy bands ($\lambda = +1$ and $\lambda = -1$). The band with $\lambda = -1$ denotes the valence band, also known as the π band, and $\lambda = +1$ denotes the π^* (conduction) band.

$$\epsilon^\lambda_{\boldsymbol{k}} = \lambda t|f(\boldsymbol{k})| = \lambda t\sqrt{3 + 2\sum_{i=1}^{3} cos(\boldsymbol{k}\cdot\boldsymbol{a}_i)} \tag{1.10}$$

In order the write the dispersion in this compact way, we have introduced a third vector $\boldsymbol{a}_3 = \frac{\sqrt{3}a}{2}(\hat{\mathbf{x}} - \sqrt{3}\hat{\mathbf{y}})$. Fig. 1.2 shows the energy for each band. Solutions to $\epsilon^\lambda_{\boldsymbol{k}} = 0$ occur at the Dirac

points, $\boldsymbol{k}^D$, and are found by solving, equivalently,

$$\mathrm{Re}[f(\boldsymbol{k}^D)] = 0 \text{ and } \mathrm{Im}[f(\boldsymbol{k}^D)] = 0. \tag{1.11}$$

The latter is satisfied by $k_y^D = 0$, which then yields $k_x^D = \pm\frac{4\pi}{3\sqrt{3}a}$.

In total, there are six solutions to eq. (1.11) that all lie on the corners of the FBZ, exactly coinciding with the K and K$'$ points. The bands touch right at the Fermi level, at these zero energy locations, making graphene a gapless semiconductor. Typically, undoped semiconductors have an intrinsic gap. In the next section, we will see that low energy excitations yield a linear dispersion, giving rise to Dirac cones centered on the Dirac points.

1.3 Continuum

In the low energy theory, we expand the effective Hamiltonian (eq. (1.9)) about the Dirac points, and hence the K and K$'$ points, via the wave vector $\boldsymbol{k} = \pm\boldsymbol{K} + \boldsymbol{q}$ for $|\boldsymbol{q}| \ll |\boldsymbol{K}|$. We first start by expanding the functions $f(\boldsymbol{k})$ to linear order in $\boldsymbol{q}$:

$$\begin{aligned} f(\pm\boldsymbol{K} + \boldsymbol{q}) &= \sum_{j=1}^{3} e^{\pm i\boldsymbol{K}\cdot\boldsymbol{\delta}_j} e^{i\boldsymbol{q}\cdot\boldsymbol{\delta}_j} \\ &\approx e^{\pm i2\pi/3}\big[1 + i\boldsymbol{q}\cdot\boldsymbol{\delta}_1\big] + e^{\mp i2\pi/3}\big[1 + i\boldsymbol{q}\cdot\boldsymbol{\delta}_2\big] + \big[1 + i\boldsymbol{q}\cdot\boldsymbol{\delta}_3\big] \\ &= \mp\frac{3a}{2}\big(q_x \pm iq_y\big). \end{aligned} \tag{1.12}$$

Note that the expansion parameter here is $|\boldsymbol{q}|a \ll 1$. There will be a copy of the low energy Hamiltonian, $h^{\pm}(\boldsymbol{q})$, for each unique Dirac point. Inserting eq. (1.12) into eq. (1.9) then gives

$$\begin{aligned} h^{\pm}(\boldsymbol{q}) &= \mp\frac{3ta}{2}\begin{pmatrix} 0 & q_x \mp iq_y \\ q_x \pm iq_y & 0 \end{pmatrix} \\ h^{\tau}(\boldsymbol{q}) &= \tau\hbar v_F\big(q_x\sigma^x + \tau q_y\sigma^y\big)_{AB}, \end{aligned} \tag{1.13}$$

where σ^x and σ^y are the Pauli matrices in the sublattice (AB) basis, and $v_F \equiv -\frac{3ta}{2\hbar} > 0$ is the Fermi velocity.

$$\sigma^x = \begin{pmatrix} 0 & 1 \\ 1 & 0 \end{pmatrix}\ ,\ \sigma^y = \begin{pmatrix} 0 & -i \\ i & 0 \end{pmatrix}\ ,\ \sigma^z = \begin{pmatrix} 1 & 0 \\ 0 & -1 \end{pmatrix} \tag{1.14}$$

The label τ denotes the valley pseudospin, and takes the value $\tau = +$ for the K point, and $\tau = -$ for the K$'$ point.

The valley index can then be thought of as a two-level system, which can be mapped onto the spin-1/2 problem. Hermitian operators in this two-level space can then be written in terms of the Pauli matrices, and we define their expectation values as $\boldsymbol{S} = (S_x, S_y, S_z)$ for real spin, and $\boldsymbol{P} = (P_x, P_y, P_z)$ for pseudospin. For example, a pseudospin orientation of $\boldsymbol{P} = (0, 0, +1)$ would refer a ground state with occupation at the K point. Later in this introduction, we will use these expectations in describing broken symmetry states.

It is helpful to introduce the four component spinor,

$$\Psi(\boldsymbol{q}) = \begin{pmatrix} \psi_+^A(\boldsymbol{q}) \\ \psi_+^B(\boldsymbol{q}) \\ \psi_-^B(\boldsymbol{q}) \\ \psi_-^A(\boldsymbol{q}) \end{pmatrix}. \tag{1.15}$$

Notice that the sublattice order has been flipped for the $\xi = -$ index. Using this representation, the low energy Hamiltonian can be written as

$$\begin{aligned} h^\tau(\boldsymbol{q}) &= \tau\hbar v_F(q_x\sigma^x + q_y\sigma^y)_{AB} \\ &= \hbar v_F \sigma_\tau^z \otimes \boldsymbol{q}\cdot\boldsymbol{\sigma} \\ \rightarrow h^\tau(\boldsymbol{p}) &= v_F \sigma_\tau^z \otimes \boldsymbol{p}\cdot\boldsymbol{\sigma}, \end{aligned} \tag{1.16}$$

with momentum $\boldsymbol{p} = \hbar\boldsymbol{q}$. In eq. (1.16), σ_τ^z denotes the last Pauli matrix in eq. (1.14), written in the valley pseudospin basis. The form of eq. (1.16) is essentially two copies, one for each valley, of a massless Dirac Hamiltonian in 2D, $H_D = v_F\boldsymbol{p}\cdot\boldsymbol{\sigma}$. This result suggests that electrons in graphene behave in a relativistic way, allowing for the possibility of a bridge between condensed matter, high-energy, and even neutrino physics. Electrons governed by this massless Dirac Hamiltonian also carry charge, which is unlike most massless elementary particles that exist in nature.

To conclude this section, we analyze the form of the low energy dispersion. Using the linear

expansion for $f(\boldsymbol{k})$ in eq. (1.10), we obtain

$$\epsilon^{\lambda}_{\boldsymbol{q},\tau} = \lambda \hbar v_F |\boldsymbol{q}|. \tag{1.17}$$

Indeed, the dispersion is linear in $\boldsymbol{q}$, and is also independent of τ. The zero energy states are thus doubly degenerate with respect to the valley pseudospin. It is important to point out that only the band index, λ, and the sublattice pseudospin are directly linked; the existence of the valley pseudospin is independent of the fact that there are two sublattices.

1.4 Graphene in a magnetic field

1.4.1 Relativistic Landau levels

To introduce a magnetic field in the tight binding model above, we use the Peierls substitution, which replaces the canonical momentum $\boldsymbol{p}$ with the (gauge-invariant) kinetic momentum $\boldsymbol{\Pi}$. We then have

$$\boldsymbol{p} \to \boldsymbol{\Pi} = \boldsymbol{p} + e\boldsymbol{A}(\boldsymbol{r}), \tag{1.18}$$

where $\boldsymbol{A}(\boldsymbol{r})$ is the vector potential associated with the magnetic field $\boldsymbol{B} = \boldsymbol{\nabla} \times \boldsymbol{A}(\boldsymbol{r})$. This kind of substitution is valid as long as the magnetic length,

$$\ell \equiv \sqrt{\frac{\hbar}{eB}}, \tag{1.19}$$

is much larger than the lattice spacing, $\tilde{a}$. With the help of some elementary commutation relations, it can be shown that the components of the kinetic momentum obey the following commutation relation:

$$\big[\Pi_x, \Pi_y\big] = -i\frac{\hbar^2}{\ell^2}. \tag{1.20}$$

We can then introduce the ladder operators,

$$\hat{a} \equiv \frac{\ell}{\sqrt{2}\hbar}\big(\Pi_x - i\Pi_y\big) \text{ and } \hat{a}^{\dagger} \equiv \frac{\ell}{\sqrt{2}\hbar}\big(\Pi_x + i\Pi_y\big), \tag{1.21}$$

which satisfy the commutation relation $\left[\hat{a}, \hat{a}^\dagger\right] = 1$. They also satisfy the following raising and lowering properties:

$$\begin{aligned} \hat{a}\,|n\rangle &= \sqrt{n}\,|n-1\rangle \text{ for } n > 0, \\ \hat{a}^\dagger\,|n\rangle &= \sqrt{n+1}\,|n+1\rangle\,, \text{ and} \\ \hat{a}^\dagger\hat{a}\,|n\rangle &= n\,|n\rangle\,. \end{aligned} \tag{1.22}$$

In terms of these ladder operators, the low energy Hamiltonian (eq. (1.16)) becomes

$$h^\tau(\mathbf{\Pi}) = \tau v_F \frac{\sqrt{2}\hbar}{\ell} \begin{pmatrix} 0 & \hat{a}(\mathbf{\Pi}) \\ \hat{a}^\dagger(\mathbf{\Pi}) & 0 \end{pmatrix}. \tag{1.23}$$

The resulting eigenvalue problem is then $h^\tau \psi_n = \epsilon_n \psi_n$, where the wave function, ψ_n, is a two component spinor indexed by the sublattice.

$$\psi_n = \begin{pmatrix} u_n \\ \\ v_n \end{pmatrix} \tag{1.24}$$

With the help of eq. (1.22), the eigenvalues are

$$\epsilon_n^2 = \left(\tau v_F \frac{\sqrt{2}\hbar}{\ell}\right)^2 n \rightarrow \epsilon_n = \lambda \frac{v_F \hbar}{\ell}\sqrt{2\ |n|}, \tag{1.25}$$

where we have used the fact that $\tau^2 = 1$. Therefore, the energies are two-fold degenerate in the valley index. Later in the text, the spin will bring an additional two-fold degeneracy to the non-interacting picture, yielding single particle energies that are four-fold degenerate with respect to spin and valley.

Notice that $\epsilon_n \propto 1/\ell \propto \sqrt{B}$, unlike regular two dimensional electron gases (2DEGs), which have a linear field dependence on their energy spectrum (see Fig. 1.3a and 1.3b). The integer n is identified as the Landau level (LL) index, which is associated with both positive ($\lambda = +1$) and negative ($\lambda = -1$) energy levels. The existence of negative energy LL's is a direct consequence of the relativistic nature of the Dirac Hamiltonian. This Dirac sea of negative energy states will play an important role later when we consider interacting models.

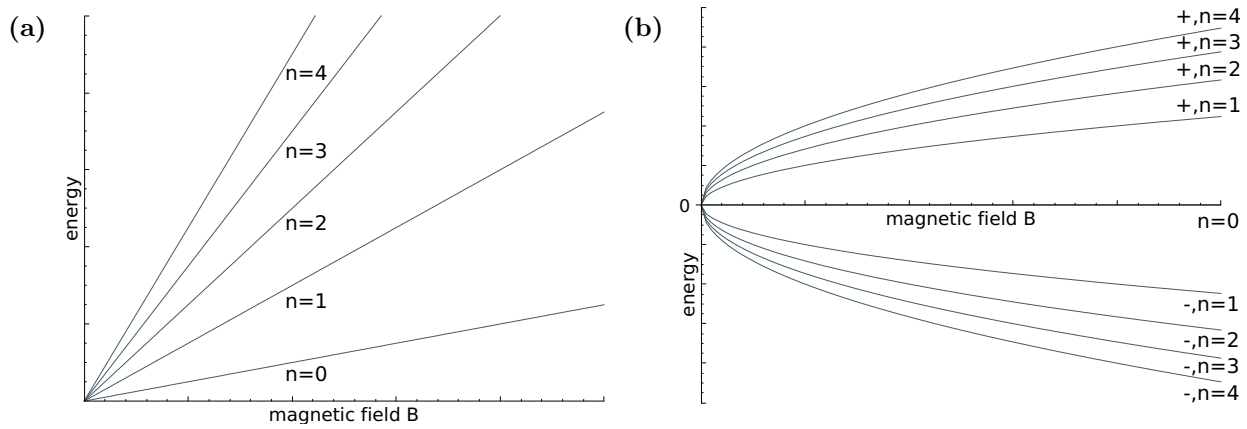

Figure 1.3: (a) Energy spectrum for non-interacting 2DEG systems in a magnetic field. The energy is linear in the magnetic field, and is characterized by only positive energy Landau levels. (b) Energy spectrum for graphene in a magnetic field. In this case, $\epsilon_n \sim \sqrt{B}$, and energy levels are indexed by $\lambda = \pm$ and n.

The components for the spinors can easily be worked out. For the special case of $n = 0$, note that $\hat{a}\,|n = 0\rangle = 0$. We choose the forms for the components to be

$$\psi_n^{\tau,\lambda} = \frac{1}{\sqrt{2}} \begin{pmatrix} \tau\lambda\,|n-1\rangle \\ |n\rangle \end{pmatrix} \text{ for } n \neq 0, \text{ and } \psi_n = \begin{pmatrix} 0 \\ |n=0\rangle \end{pmatrix} \text{ for } n = 0. \tag{1.26}$$

The last part of eq. (1.26) reveals that, when $n = 0$, all of the weight resides on a single sublattice, which is then uncoupled from the valley index. For example, when $n = 0$, the K point ($\tau = 1$) coincides with the B sublattice, and the K$'$ point ($\tau = -1$) coincides with A sublattice. The particular spatial dependence for the orbital wave functions is worked out in the next section.

1.4.2 Orbital wave functions

The low energy spectrum for graphene in a magnetic field, derived in the previous section, was found to be (necessarily) gauge independent. However, the spatial dependence on the eigenfunctions for the Dirac Hamiltonian are gauge dependent; the choice of the vector potential can break translational symmetry in the Hamiltonian in various ways. We take the magnetic field to be $\boldsymbol{B} = B\hat{\mathbf{z}}$, and choose a Landau gauge, $\boldsymbol{A}(\boldsymbol{r}) = Bx\hat{\mathbf{y}}$.

In terms of momentum and position operators, the components of the two-spinor (eq. (1.24)) satisfy the eigenvalue equations

$$\begin{aligned} v_F^2\big[\hat{p}_x + i(\hat{p}_y + eB\hat{x})\big]\big[\hat{p}_x - i(\hat{p}_y + eB\hat{x})\big]v = \epsilon^2 v, \text{ and} \\ v_F^2\big[\hat{p}_x - i(\hat{p}_y + eB\hat{x})\big]\big[\hat{p}_x + i(\hat{p}_y + eB\hat{x})\big]u = \epsilon^2 u. \end{aligned} \tag{1.27}$$

We need only focus on one of these components, as the final result will be the same for both components. Notice that the left hand side of eq. (1.27) is translationally invariant in the y-direction. Therefore the momentum $p_y = \hbar k$ is a good quantum number, and we can look for solutions of the form

$$v_{n,k}(x,y) = e^{-iky}\phi_{n,k}(x). \tag{1.28}$$

After a little more algebra, and use of some elementary commutation relations, the eigenvalue equation becomes

$$\left[\frac{\hat{p}_x^2}{2m} + \frac{1}{2}m\omega_c^2(\hat{x} - k\ell^2)^2\right]v_{n,k}(x,y) = \frac{1}{2m}\left[\frac{\epsilon_n^2}{v_F^2} + eB\hbar\right]v_{n,k}(x,y) = E_n v_{n,k}(x,y), \tag{1.29}$$

where

$$w_c = \frac{eB}{m} \tag{1.30}$$

is the cyclotron frequency.

The form of eq. (1.29) is exactly that of a harmonic oscillator with cyclotron orbits centered at $X \equiv k\ell^2$, with X as the guiding center coordinate. The energy eigenvalues are readily obtained by $E_n = \hbar\omega_c\big(n + \frac{1}{2}\big)$, which then yields the same expression for ϵ_n found in the previous section. The normalized eigenfunctions are

$$v_{n,k}(\boldsymbol{r}) = \left(\frac{1}{\pi\ell^2 L_y^2}\right)^{1/4}\frac{1}{\sqrt{2^n n!}}e^{-iky}e^{-[(x-k\ell^2)^2/(2\ell^2)]}H_n\left(\frac{x-k\ell^2}{\ell}\right), \tag{1.31}$$

where L_y is the length of the sample in the y direction, and $H_n(x)$ are Hermite polynomials.

1.4.3 Degeneracy and filling factor

There is an enormous degeneracy that emerges in this system, because the energy spectrum is independent of the momentum, $p_y = \hbar k$, carried by the plane waves. We can work out what this degeneracy is in terms of the number of states, g, contained in a finite system with periodic boundary conditions. The requirement that $e^{-ik(y+L_y)} = e^{-iky}$ yields the condition $kL_y = 2\pi g$, for integer g. Noting that $x = L_x$ corresponds to the wave vector $k = L_x/\ell^2$, the number of states in an area $S = L_x L_y$ is

$$g = \frac{S}{2\pi\ell^2}. \tag{1.32}$$

The degeneracy per unit area is determined by the flux density,

$$n_B = \frac{g}{S} = \frac{1}{2\pi\ell^2} = \frac{B}{\Phi}, \tag{1.33}$$

where $\Phi = h/e$ is a measure of flux quantum. In other words, for each LL, there is one state per flux quantum.

Since electrons obey the Pauli exclusion principle, they will first occupy the lowest energy LL, and then fill higher orbitals. To quantify this, we introduce the filling factor, ν, which denotes the number of electrons per flux quantum, and is given by

$$\nu = \frac{n_e}{n_B} = 2\pi\ell^2 n_e \sim \frac{1}{B}, \tag{1.34}$$

where n_e is the 2D density of electrons. The filling factor gives us the number of occupied LL's for non-interacting electrons. Notice that ν is inversely proportional to the magnetic field. Thus, as the field increases, the maximum occupancy for each LL grows, requiring fewer total LL's to be occupied. This is why it is a relatively good approximation in many high-field quantum Hall models to project into just a few low energy LL's, and assume the higher levels are completely unoccupied.

In the context of undoped graphene, there are as many occupied LL's ($n < 0$) as there are unoccupied ($n > 0$). In the non-interacting limit, each LL is four-fold degenerate due to the two

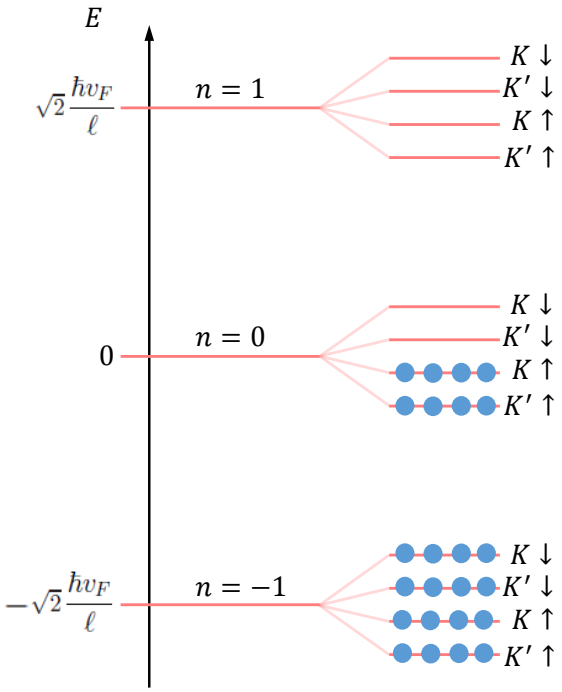

Figure 1.4: Schematic of the energy levels broken down first by LL index, then by spin and valley subbranches, in the non-interacting system. For graphene, half filling of the $n = 0$ LL corresponds to filling factor $\nu = 0$. The splitting shown here is strictly for illustration purposes. The particular configuration for the occupied levels is also for illustration purposes, which, in this case, represents a spin polarized valley singlet state. Such a state might be realized in the presence of a Zeeman field, but, in general, the occupation of energy levels can look quite different from what is shown here. Image adapted from Ref. [6].

copies of spin and valley. At zero filling, this entails occupying only two of the four configurations. Therefore, the $n = 0$ LL is exactly half filled. One particular illustration of this is shown in Fig. 1.4. We can also calculate the lowest LL, n_c, which must be filled in order to accommodate one electron per atom, which is the density of mobile electrons for undoped graphene. Its value is given by

$$n_c = \frac{2\pi\ell^2}{2A_c}. \tag{1.35}$$

The factor of 2 in the denominator comes from the fact that there are two electrons per unit cell.

1.4.4 Quantum Hall effect in graphene

The quantum Hall effect (QHE) is realized in systems of charged particles, confined to 2D, which are subject to a strong magnetic field. Before graphene, these kinds of systems had to be engineered, typically through transistor-like devices (MOSFETs) or heterostructures. As one particular example, GaAs heterostructures can be used to create a 2DEG at an interface, by trapping electrons in quantum wells with various types of 2D geometry.

Because of its high mobility, and 2D structure, graphene is an ideal platform to realize the QHE. Shortly after the material was synthesized, evidence of the integer QHE (IQHE) was observed [7,8]. The signature for this effect occurs when the Hall conductance,

$$\sigma_{xy} = \frac{e^2}{h}\nu, \tag{1.36}$$

exhibits plateaus, while the longitudinal resistance, ρ_{xx}, vanishes, as the electron density is varied. This is achieved by tuning the magnetic field, or by applying a gate voltage to the sample. The plateaus occur for certain integer values of the filling factor:

$$\nu_{_N} = \pm 4(N + \frac{1}{2}), \tag{1.37}$$

where N is a positive integer, and is equal to the highest completely filled LL. The factor of 4 is a consequence of the spin and valley degeneracy for each LL. The factor of $\frac{1}{2}$ is related to the

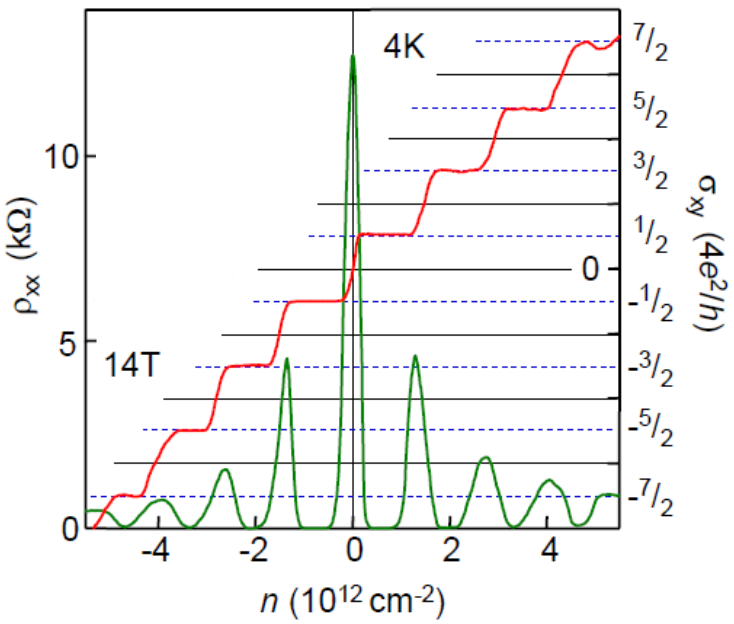

Figure 1.5: The Hall conductance, σ_{xy}, as a function of electron density, and hence the filling factor, for a sample of graphene in a fixed magnetic field. Image reproduced from Ref. [8].

pseudospin winding number. Fig. 1.5 shows a plot of the Hall conductance measured in one of the first realizations of the IQHE in graphene. At $\nu = 0$, the Hall conductance is halfway between its two nearest plateaus, confirming that the charge neutral point corresponds to a half filled LL.

The existence of plateaus in systems like this is most naturally understood by considering impurities in the sample, which can be modeled by a small, random, potential that varies slowly over the scale of the magnetic length. This disorder leads to a broadening of the energy for a particular LL. Each LL can then be occupied by states that are classified as either extended or localized. The former corresponds to states that can propagate throughout the entire sample. Localized states are spatially confined to equipotential lines of the disorder potential, and are lower (higher) in energy near the local minima (maxima).

Because the localized states are trapped, they cannot contribute to the transport across the sample. The intermediate energies correspond to the extended states, which can contribute to the Hall conductance. Therefore, as the chemical potential increases, and the localized states

become occupied within a particular LL, there is no change to the Hall conductance. Increasing the chemical potential further eventually leads to a percolation transition, in which extended states begin to contribute to the conductance. After this transition, all of the current is then carried by the edge states, within that particular LL, and there is no further change to the conductance as the rest of the LL is filled.

There will be one factor of $\frac{e^2}{h}$ added to the Hall conductance for each band that is completely filled. One way to understand where this factor comes from is by looking at the effects of an edge potential. In the following discussion, it is also helpful to restrict ourselves to the simpler case of a 2DEG. In the semi-classical picture for conventional 2DEGs, the cyclotron orbits of electrons at the edge causes a skipping motion as they collide into the wall. As a result, electrons will only move in one direction along an edge, and so the edge states are said to be chiral. It is this chiral motion that ultimately leads to the particular quantized values of the Hall conductance. To see why this happens, we introduce an edge potential which rises steeply as we approach each boundary, i.e. along the direction perpendicular to the plane wave motion of the electrons in the sample.

Following the formalism in section 1.4.2, and assuming that the edge potential, $V(x)$, varies slowly over the scale of the magnetic length, we can Taylor expand the potential about the guiding center coordinates. The Hamiltonian of eq. (1.29) becomes

$$\hat{H}_k = \frac{\hat{p}_x^2}{2m} + \frac{1}{2}m\omega_c^2(\hat{x} - k\ell^2)^2 + \frac{\partial V}{\partial x}\hat{x}, \tag{1.38}$$

where $\frac{\partial V}{\partial x}$ is evaluated at the guiding center. After completing the square and noting that the system is still translationally invariant in the y direction, the corresponding energy eigenvalues are given by

$$\bar{E}_n(k) = E_n - \frac{1}{2m\omega_c^2}\left(\frac{\partial V}{\partial x}\right)^2 + k\ell^2\frac{\partial V}{\partial x}, \tag{1.39}$$

where $E_n = \hbar\omega_c(n + \frac{1}{2})$ are the unperturbed orbital energies. For now, we will focus only on the case for a single LL; the argument is easily generalized to N filled LL's.

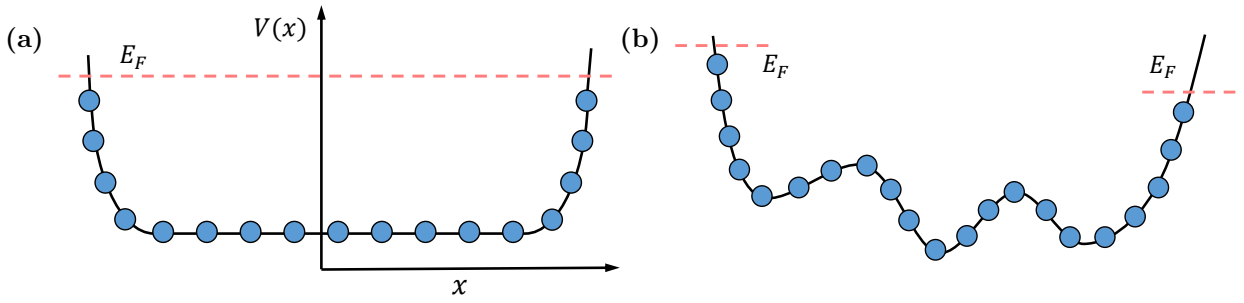

Figure 1.6: 2DEG picture for the edge potential in a single LL. Blue dots represent occupied states, and the sample's edges are modeled as a steeply rising potential. (a) Equal occupation of edge states leads to a zero net current in the system. (b) A more realistic picture with a random bulk-potential. Applying a gate voltage causes an imbalance of edge states, and leads to a Hall current localized to the sample's boundary. Both images adapted from Ref. [9].

We then introduce a chemical potential, and fill states up to the Fermi energy, E_F (see Fig. 1.6a). Notice that the group velocity,

$$\boldsymbol{v}_k = \frac{1}{\hbar}\frac{\partial \bar{E}}{\partial k}\hat{\mathbf{y}} = \frac{1}{eB}\frac{\partial V}{\partial x}\hat{\mathbf{y}}, \tag{1.40}$$

has opposite signs on either edge, corresponding to the chiral motion of the edge currents when the system is in its ground state. Furthermore, the system is insulating in the bulk, because the band is filled, but behaves as a metal at the edges. It is important to note that the form of the potential does not necessarily have to be flat in the bulk, and that impurities can, and do, randomize the potential. As long as this potential remains smoothly varying, and does not become larger than the Fermi energy, the following calculation will hold.

If a Hall voltage is applied across the x direction, a chemical potential difference, $\Delta\mu$, will form between each edge, and this will give rise to a net Hall current (Fig. 1.6b). To calculate this current, we sum the group velocity over all of the filled states:

$$I_y = -\frac{e}{L_y}\int dk \frac{L_y}{2\pi}\frac{1}{\hbar}\frac{\partial \bar{E}}{\partial k} = \frac{e}{h}\Delta\mu. \tag{1.41}$$

Noting that the Hall voltage is $eV_H = \Delta\mu$, the resulting Hall conductance for a single filled LL is

$$\sigma_{xy} = \frac{I_y}{V_H} = \frac{e^2}{h}. \tag{1.42}$$

Since the edge potential affects every filled LL in the same way, we can generalize this result to the case when there are N filled levels by simply summing over the number of filled levels in eq. (1.41). The result is precisely that of eq. (1.36) with $\nu \to N$, as long as the Fermi energy resides between LL's. Hence, there are N types of chiral modes on each edge. The edge states are also protected from back scattering to a state with opposite momentum because of the macroscopic separation of the two edges; therefore, excitations at the edge can only produce forward scattering. It should also be noted that the discussion above was presented within the context of a 2DEG. The edge state behavior can be extended to graphene quite easily, which we will do in the next section.

With fabrication techniques improving over the years, cleaner samples of graphene have been made possible. Because these samples have inherently fewer impurities in them, it is easier to resolve the symmetry-breaking effects in the $n = 0$ LL; interactions which would normally be suppressed from disorder now have a more noticeable effect. Additional quantum Hall plateaus have therefore been observed outside of the usual sequence given in eq. (1.37), particularly at $\nu = 0, \pm 1$ [10]. The states at $\nu = \pm 1$ are well understood within the context of quantum Hall ferromagnetism, which causes a charge induced gap due to strong Coulomb-driven exchange interactions [11]. This exchange interaction competes with the disorder in the sample, and causes the system to favor a ferromagnetic configuration in the discrete degrees of freedom. The quantum Hall state at $\nu = 0$, however, requires a more delicate treatment of interactions, as we will see in the next section. The precise nature of the $\nu = 0$ state, and the interactions that govern it, will be a large part of the focus for this thesis.

1.5 The quantum Hall state at $\nu = 0$

In the non-interacting picture at $\nu = 0$, the spin-valley subbranches in the $n = 0$ LL are four-fold degenerate, and are occupied on average by two electrons. The simplest way to lift this degeneracy would be to add a Zeeman interaction. The effect of this interaction on the bulk spectrum is fairly straight forward, however it is important to consider what this effect will do to the edge states. When approaching the sample boundaries, the energy dispersion for the $n = 0$ bands increases with positive slope for electron-like bands, and decreases with negative slope for hole-like bands. This behavior can be realized in the continuum model with boundary conditions appropriate for graphene's geometry at the edge[12].

Adding a Zeeman coupling of arbitrary strength, the degeneracy in the spin degree of freedom is lifted, and a gap, equal to the Zeeman energy and centered at the Fermi level, opens in the bulk. The obvious choice for the resulting bulk state is a spin polarized ferromagnet. At the edge, two bands with opposite spin orientations cross at the Fermi energy, corresponding to counter propagating edge states (Fig. 1.7a). These edge modes are protected from backscattering between spin channels because of the conservation of spin within the helical edge states. The transport direction, i.e. chirality, is linked to the orientation of the spin. Therefore, on each edge of the sample, electrons in the spin-up channel will flow opposite to those in the spin-down channel. The Hall conductance in this case is zero, because the net charge current on each edge vanishes. There is, however, a non-zero spin current, giving rise to a quantum spin Hall effect.

One way of realizing the transport properties in the situation described above is to preform a two-terminal conductance measurement. An idealized picture for this setup is illustrated in Fig. 1.7b. Two contacts are attached to the sample, and held at different chemical potentials such that $\mu_T > \mu_B$. The current injected into the sample then flows from one contact to the other via a single spin channel for each edge of the sample. That is, current moving in the direction of the net current, I, will be in the spin-down channel (blue arrow) along the right edge, and in the spin-up

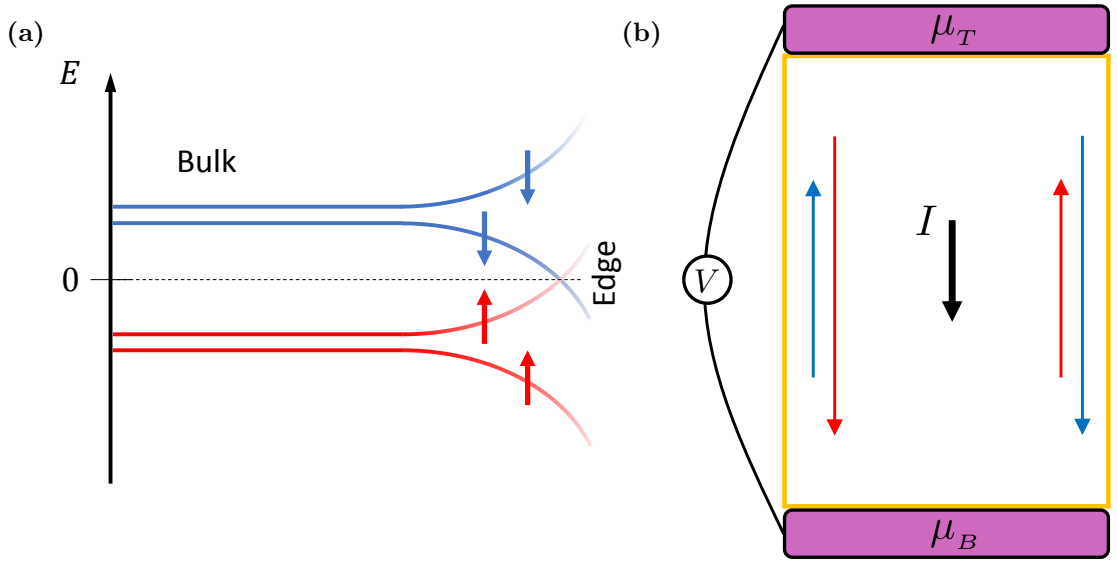

Figure 1.7: (a) Bulk-edge band structure in the presence of a Zeeman splitting. The bulk ground state is spin polarized, and, due to electron-like and hole-like dispersion towards the edge, there is a band crossing. This yields a pair of counter propagating helical edge modes, which are characterized by their spin polarization. Image adapted from Ref. [13]. (b) A simplified schematic for a two-terminal conductance setup. Current flows along the edge of the sample through spin-up (red arrow) or spin-down (blue arrow) channels. The contacts (shaded purple) are held at different chemical potentials such that $\mu_T > \mu_B$, giving rise to a net current downward.

channel (red arrow) along the left edge. In terms of this current and the voltage drop between contacts, the two-terminal conductance, G, is defined as $G = I/V = eI/(\mu_T - \mu_B)$.

Furthermore, because there are two spin channels carrying current from one contact to the other, we would expect a quantized value of $2e^2/h$ for the two-terminal conductance (one factor of e^2/h from each edge). However, the experiment in Ref. [14] has shown evidence contrary to this result. They instead find that, at low Zeeman (total) field, the system becomes insulating. In these experiments, graphene is suspended in an external magnetic field with a finite tilt angle, which is measured between the direction of the field and an axis that is normal to the graphene plane. Changing the tilt angle thus allows the field perpendicular to the sample ($B_\perp$) to be smaller than the total field (B_T). Since the orbital degrees of freedom only depend on $B_\perp$, tilted field experiments allow for a direct tuning of the Zeeman energy, which becomes greatly enhanced, while $B_\perp$ is fixed. Fig. 1.8 shows the two-terminal conductance for a wide range of B_T and fixed $B_\perp$. The system is strongly insulating at low fields, and gradually becomes more conductive as the field increases. At high enough external fields, the bulk state becomes a spin-polarized ferromagnet with a quantized conductance.

The fact that the system is insulating at low fields suggests that the picture for the band-crossing at the edge (Fig. 1.7a) is not generally correct. To be more consistent with the experiment, there would actually need to be a gap at the edge, which would only happen if the bulk ground state was spin-unpolarized. It is evident, then, that including only the Zeeman interaction is not enough to describe the $\nu = 0$ ground state.

The energy scales in graphene are primarily dominated by the cyclotron motion and the long range Coulomb interaction, both of which preserve the SU(4) symmetry formed by the spin-valley flavor. The Zeeman splitting is just one type of possible symmetry-breaking, and is the only interaction which can break the spin symmetry, owing to the fact that spin-orbit interactions are relatively weak for graphene. Lattice interactions, however, can break the symmetry in the valley

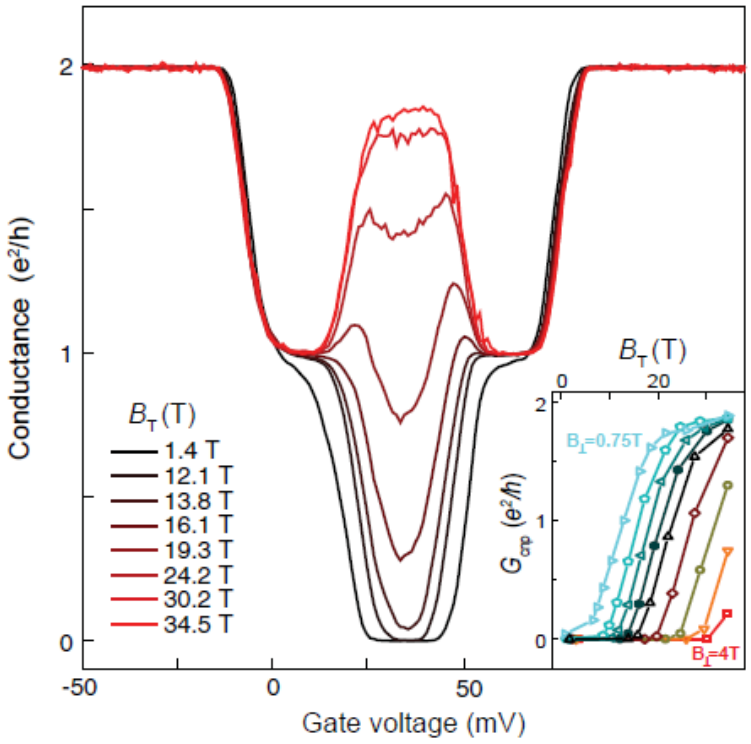

Figure 1.8: Two-terminal conductance measurement as a function of gate voltage and total field. The conductance vanishes at the charge neutral point ($\nu = 0$) at low fields, and increases continuously as the field increases. Image reproduced from Ref. [14].

degree of freedom, and allow for a wide range of possible ground states.

1.6 Kharitonov model

There have been a number of studies [6,11,15–24] over the years that treat the possible symmetry-breaking effects due to interactions in graphene. One of those studies [6] is of particular interest for the current discussion. In the Kharitonov model, short-range (SR) e-e interactions which break the valley and sublattice degrees of freedom, in addition to a spin splitting Zeeman interaction, are explicitly added to the Hamiltonian.

The short-range interactions are given by

$$\hat{H}_{e-e,SR} = \frac{1}{2}\int d^2\boldsymbol{r} \sum_{\alpha,\beta}{}' g_{\alpha\beta}\big[\hat{\psi}^\dagger(\boldsymbol{r})\mathcal{T}_{\alpha\beta}\hat{\psi}(\boldsymbol{r})\big]^2, \tag{1.43}$$

where $\hat{\psi}(\boldsymbol{r}) = [\hat{\psi}_\uparrow(\boldsymbol{r}), \hat{\psi}_\downarrow(\boldsymbol{r})]^T$ is an eight component spinor written in the spin basis, and

$$\hat{\psi}_\sigma(\boldsymbol{r}) = \begin{pmatrix} \hat{\psi}_{KA\sigma}(\boldsymbol{r}) \\ \hat{\psi}_{KB\sigma}(\boldsymbol{r}) \\ \hat{\psi}_{K'B\sigma}(\boldsymbol{r}) \\ -\hat{\psi}_{K'A\sigma}(\boldsymbol{r}) \end{pmatrix} \tag{1.44}$$

are the Dirac fields, written in terms of a direct product, $KK' \otimes AB$, for the valley and sublattice. Here, $\sigma = (\uparrow, \downarrow)$ is the spin label. The matrix elements,

$$\mathcal{T}_{\alpha\beta} = \tilde{\sigma}_\alpha^{KK'} \otimes \tilde{\sigma}_\beta^{AB} \otimes \hat{1}^\sigma, \tag{1.45}$$

are given in terms of the Pauli matrices, $\tilde{\sigma}_x, \tilde{\sigma}_y, \tilde{\sigma}_z$, and $\alpha, \beta = 0, x, y, z$.

The generality of this model comes from the fact that the sum, $\sum'_{\alpha,\beta}$, runs over all combinations of α and β, except for the special case when $\alpha = \beta = 0$, which corresponds to the symmetric long range Coulomb (C) interaction,

$$\hat{H}_{e-e,C} = \frac{1}{2}\int d^2\boldsymbol{r} d^2\boldsymbol{r}' \big[\hat{\psi}^\dagger(\boldsymbol{r})\hat{\psi}(\boldsymbol{r})\big] \frac{e^2}{|\boldsymbol{r}-\boldsymbol{r}'|} \big[\hat{\psi}^\dagger(\boldsymbol{r}')\hat{\psi}(\boldsymbol{r}')\big]. \tag{1.46}$$

It is understood that the operators in eq. (1.43) and eq. (1.46) are normal ordered. Lastly, $g_{\alpha\beta}$ are the bare coupling constants. The model is then projected into the $n = 0$ LL (zLL), which is a great simplification because the wave functions for a particular valley have weight on only one sublattice, as discussed in I.D.1. The higher order LL effects are renormalized into the bare couplings for the short range anisotropies. This generates, after symmetry considerations, two effective parameters, $u_\perp$ and u_z, which are referred to as the anisotropy energies. Using these two parameters, the short range interaction can be written in a more simplified way as

$$\hat{H}_{e-e,SR} = \frac{1}{2}\sum_s \int d^2\boldsymbol{r}\big\{u_\perp\big[M_x(\boldsymbol{r},s)M_x(\boldsymbol{r},s) + M_y(\boldsymbol{r},s)M_y(\boldsymbol{r},s)\big] + u_z M_z(\boldsymbol{r},s)M_z(\boldsymbol{r},s)\big\}, \quad (1.47)$$

where

$$M_i(\boldsymbol{r},s) = \sum_{\tau_1,\tau_2}\sum_\sigma \hat{\psi}^\dagger_{\sigma\tau_1}(\boldsymbol{r},s)(\tilde{\sigma}_i)_{\tau_1\tau_2}\hat{\psi}_{\sigma\tau_2}(\boldsymbol{r},s) \quad (1.48)$$

can be thought of as a magnetization of the valley pseudospin. In eq. (1.47), $s = A, B$ refers to the sublattice index.

The results of the study yield a phase diagram, within the space of the anisotropy energies, with four potential ground states. For the present discussion, we project the states into the $n = 0$ LL, and ignore any structure which might be present for $n \neq 0$. This allows us to associate a particular sublattice with a single valley index. For example, the K' valley would correspond to the A sublattice, and the K valley would correspond to the B sublattice. In addition, we assume the states are uniform, in real space, so that they do not admix guiding centers. The ground states are then characterized by their spin and valley structure, and can be represented by a density matrix, $\langle\hat{\psi}^\dagger_{\sigma\tau}\hat{\psi}_{\sigma'\tau'}\rangle$. At $\nu = 0$, the trace of this matrix, excluding any geometric normalizations, yields a factor of 2, because there are two electrons which occupy the half filled $n = 0$ LL. We will define the density matrix more concretely in Chapter 2. To better describe the ordering of the various phases, we will make use of the Bloch vectors for spin, $\boldsymbol{S} = (S_x, S_y, S_z)$, and pseudospin, $\boldsymbol{P} = (P_x, P_y, P_z)$.

The ground states are as follows:

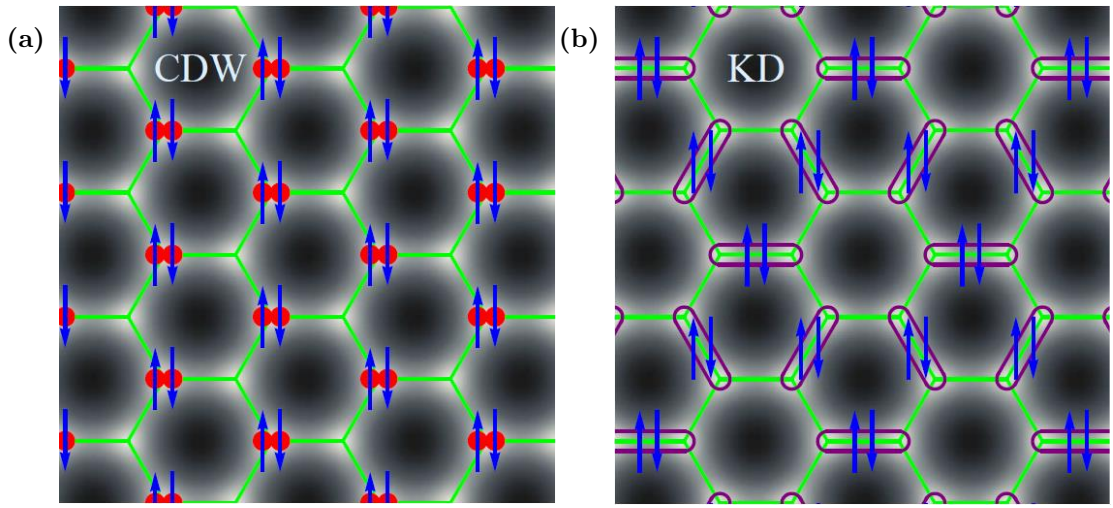

Figure 1.9: Illustrations of the possible ground states at $\nu = 0$. (a) Charge density wave (CDW) phase. (b) Kekulé-distortion (KD) phase. Both images reproduced from Ref. [6].

1) The charge density wave (CDW), characterized by a valley polarized spin singlet, in which both electrons occupy the same sublattice, but have opposite spin orientations. Occupation of the A sublattice yields the same energy as an occupation of the B sublattice. The CDW, therefore, has a Z_2 symmetry with respect to the valley space. The density matrix is

$$\langle \hat{\psi}^{\dagger}_{\sigma\tau} \hat{\psi}_{\sigma'\tau'} \rangle_{\text{CDW}} \propto \delta_{\sigma,\sigma'} \delta_{\tau,K} \delta_{\tau',K}, \tag{1.49}$$

where we have chosen a particular occupation of the K valley, so that the pseudospin orientation is $\boldsymbol{P} = (0, 0, +1)$. An illustration of this phase is shown in Fig. 1.9a.

2) The Kekulé-distortion (KD) phase, in which each electron occupies the K and K' points with equal weight, has a pseudospin orientation which resides on the equator of the Bloch sphere. Taking φ to be the in-plane azimuthal angle, the pseudospin orientation in this case is $\boldsymbol{P} = (\cos\varphi, \sin\varphi, 0)$. The KD phase has the property that in-plane rotations of the pseudospin vector leave the energy for the system unchanged, yielding a U(1) symmetry in the valley space. This is the only state that admixes the valley index, and so one may think of it as a dimerized pairing of the two electrons between valleys. It is important to note that there is no physical distortion of the actual graphene

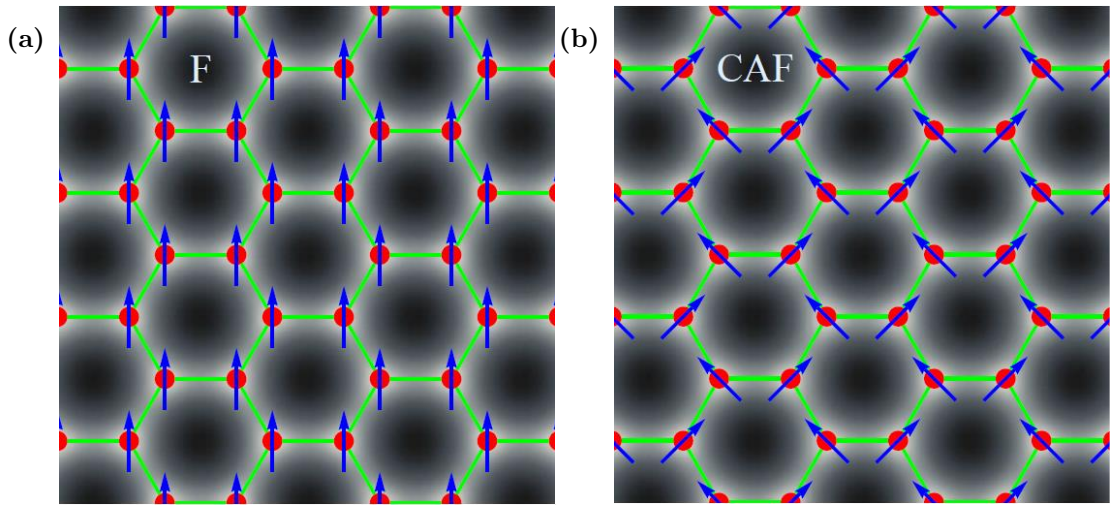

Figure 1.10: Illustrations of the possible ground states at $\nu = 0$. (a) Ferromagnet (FM) phase. (b) Canted anti-ferromagnet (CAF) phase. Both images reproduced from Ref. [6].

lattice in this phase. The KD phase, like the CDW, is spin-unpolarized, and its density matrix is given by

$$\langle \hat{\psi}^\dagger_{\sigma\tau} \hat{\psi}_{\sigma'\tau'} \rangle_{\text{KD}} \propto \frac{1}{2} \delta_{\sigma,\sigma'}, \tag{1.50}$$

where we have chosen the pseudospin orientation to be $\boldsymbol{P} = (+1, 0, 0)$. An illustration of the phase is given in Fig 1.9b.

3) The ferromagnet (FM), a spin polarized valley singlet state, has a spin orientation of $\boldsymbol{S} = (0, 0, +1)$ in the presence of a Zeeman field aligned in the positive z-direction. Because the state is spin polarized, its energy depends linearly on the Zeeman field strength. The density matrix representation is

$$\langle \hat{\psi}^\dagger_{\sigma\tau} \hat{\psi}_{\sigma'\tau'} \rangle_{\text{FM}} \propto \delta_{\sigma,\uparrow} \delta_{\sigma',\uparrow} \delta_{\tau,\tau'}. \tag{1.51}$$

Fig. 1.10a shows an illustration for the phase.

4) The last phase is the canted anti-ferromagnet (CAF), which is partially spin polarized along the direction of the Zeeman field, but with opposite in-plane spin orientations between each valley. An illustration of this phase is shown in Fig. 1.10b. The state has the property that simultaneous rotations of the in-plane spin for each valley does not change the energy, giving the state a U(1)

spin-symmetry. Taking $s_z = \cos\theta$, where θ, also referred to as the canting angle, is the polar angle measured from the positive z-axis of the Bloch sphere, the spin orientation for each sublattice (or valley) can be written as

$$\boldsymbol{S}_{\mathrm{A,B}} = \big(\pm \sqrt{1 - s_z^2} \cos\varphi, \pm \sqrt{1 - s_z^2} \sin\varphi, s_z \big). \tag{1.52}$$

The particular choice of the canting angle is chosen such that the Zeeman and anisotropy energies are minimized, which is determined by a competition between the anisotropic interactions which break the valley symmetry, and the Zeeman interaction. The former prefers anti-ferromagnetic correlations, while the latter prefers ferromagnetic ones. This results in equal spin projections along the Zeeman direction, and anti-parallel spin orientations in the (xy) plane, as shown in Fig. 1.11a. The canting angle approaches zero as the Zeeman field is increased, eventually leading to a continuous phase transition from CAF ($s_z < 1$) to FM ($s_z = 1$). All other phase transitions in this model are first order. Fig. 1.11b shows the phase diagram within the space of the anisotropy energies for a fixed Zeeman energy, ϵ_z. The point where the phases meet is a function of the Zeeman energy. Thus, as the Zeeman field is increased, the FM takes up more space in the phase diagram.

The various states realized in this model, with the exception of the FM, do not host conducting edge channels; that is, they do not have gapless charged excitations at the edge [25–30]. The FM is the only state here that supports helical edge modes, which yields a non-zero two-terminal conductance, as discussed in section 1.5.

While this model gives a rich number of interesting phases, it is based on interactions which are phenomenological. There is no clear connection between the interaction parameters, $u_\perp$ and u_z, and the microscopic interaction parameters which might be present in the physical graphene system. This will be the subject of our study in Chapter 2. Furthermore, what becomes of these states when the system is not exactly at integer filling remains an open question. We will study what happens to the system when it is doped slightly away from $\nu = 0$ in Chapters 4 and 5.

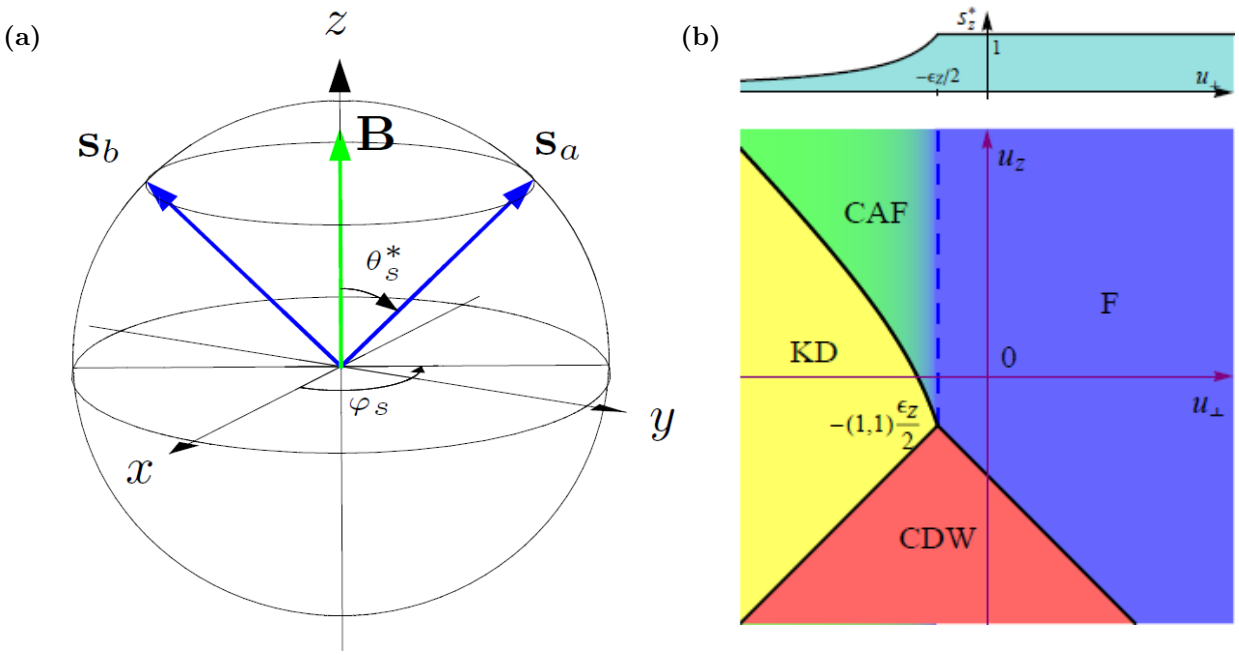

Figure 1.11: (a) Spin projections (blue arrows) on the Bloch sphere for the CAF phase. The in-plane spin between sublattices have opposite orientations, but share a common Zeeman direction (green arrow). The polar angle, θ_s^*, is chosen so that the ground state energy is minimized with respect to the anisotropy and Zeeman energies. The angle φ_s is chosen freely, due to the U(1) spin symmetry. (b) Phase diagram for the Kharitonov model. The solid black curves denote first order transitions between phases, while the dashed blue line represents a continuous transition between the CAF and FM. Both images reproduced from Ref. [6].

Chapter 2

Uniform Broken Symmetry States at $\nu = 0$

As discussed in the introduction, it is tempting to describe the $\nu = 0$ quantum Hall (QH) state of graphene as a spin polarized FM. Results from early transport experiments [10] seemed to validate this description, claiming that a spin splitting in the $n = 0$ LL would dominate the behavior of the $\nu = 0$ QH state. In that experiment, they performed measurements of the activation gap with varying Zeeman energy (tilt), but, at that time, there was less appreciation for the variety of potential ground states at $\nu = 0$. In more recent years, other experiments [14,31] on clean graphene samples concluded that the $\nu = 0$ ground state is spin unpolarized.

The assertion is supported by considering the effects of edge state transport on two-terminal conductance measurements, as discussed in section 1.5. If the system is truly a spin polarized FM in the presence of a Zeeman field of arbitrary strength and no other interactions, then one would expect such a measurement to yield a quantized value of $2e^2/h$. What they found, instead, was a vanishing conductance, at low (total) fields, which increased continuously as the field was increased, all while keeping the perpendicular field component fixed. The result indicates that interactions which break the SU(4) symmetry play a fundamental role in determining the ground state at $\nu = 0$. Since Zeeman interactions can only lift the spin degeneracy, it is left to the lattice scale interactions to break the symmetry of the sublattice/valley.

In this chapter we introduce a microscopic model [32] for the lattice scale interactions specific to monolayer graphene, as well as the symmetric long-range Coulomb interaction. Zeeman and cyclotron terms are included in the single particle Hamiltonian. The model is studied within a self-consistent, numerical, Hartree-Fock (HF) approximation, which requires the assumption that the exact ground state can be written in terms of a Slater determinant. Negative energy LL's, and LL-mixing (LLM) terms, are explicitly included in this study, and are shown to play a critical

role in determining the ground state. The calculation is largely unrestricted in the sense that we make no a priori assumption on the structure of a density matrix which represents a solution to the HF equations. There is one exception, regarding the number of LL's explicitly included in the calculation, which will be discussed in section 2.3.

Before introducing the model, it is helpful to expand the field operators around the low energy Dirac points, which coincide with the two inequivalent points

$$\boldsymbol{K} = -\boldsymbol{K'} = \frac{4\pi}{3\sqrt{3}a}\hat{\mathbf{x}} = \mathcal{K}\hat{\mathbf{x}}, \tag{2.1}$$

in the FBZ. The locations of the valley points can be written in terms of the valley pseudospin index, $\tau = (+,-)$ or, equivalently, $\tau = (K, K')$, as $\pm\boldsymbol{K} = \tau\mathcal{K}\hat{\mathbf{x}}$. The field operators are represented as

$$\Psi_\sigma(\boldsymbol{R}) \equiv \frac{1}{\sqrt{N_s}} \sum_{\boldsymbol{k}\in \mathrm{FBZ}} e^{i\boldsymbol{k}\cdot\boldsymbol{R}} c_{\boldsymbol{k}\sigma}, \tag{2.2}$$

which are separated into two equal halves in momentum space:

$$\Psi_\sigma(\boldsymbol{R}) = \frac{1}{\sqrt{N_s}}\left[{\sum_{\boldsymbol{q}}}' e^{i(\boldsymbol{q}+\boldsymbol{K})\cdot\boldsymbol{R}} c_{\boldsymbol{q}+\boldsymbol{K},\sigma} + {\sum_{\boldsymbol{q}}}'' e^{i(\boldsymbol{q}+\boldsymbol{K'})\cdot\boldsymbol{R}} c_{\boldsymbol{q}+\boldsymbol{K'},\sigma} \right], \tag{2.3}$$

where $\sigma = (\uparrow,\downarrow)$ is the spin label. The first sum is over $\boldsymbol{q}$'s closest to $\boldsymbol{K}$, and the second sum is over $\boldsymbol{q}$'s closest to $\boldsymbol{K'}$. Then, defining

$$\Psi_{\sigma,\boldsymbol{K}}(\boldsymbol{R}) \equiv \left(\frac{2}{N_s}\right)^{1/2} {\sum_{\boldsymbol{q}}}' e^{i\boldsymbol{q}\cdot\boldsymbol{R}} c_{\boldsymbol{q}+\boldsymbol{K},\sigma} \tag{2.4}$$

and

$$\Psi_{\sigma,\boldsymbol{K'}}(\boldsymbol{R}) \equiv \left(\frac{2}{N_s}\right)^{1/2} {\sum_{\boldsymbol{q}}}'' e^{i\boldsymbol{q}\cdot\boldsymbol{R}} c_{\boldsymbol{q}+\boldsymbol{K'},\sigma}, \tag{2.5}$$

the field operators are written as

$$\begin{aligned} \Psi_\sigma(\boldsymbol{R}) &= \frac{1}{\sqrt{2}}\left[e^{i\boldsymbol{K}\cdot\boldsymbol{R}}\Psi_{\sigma,\boldsymbol{K}}(\boldsymbol{R}) + e^{i\boldsymbol{K'}\cdot\boldsymbol{R}}\Psi_{\sigma,\boldsymbol{K'}}(\boldsymbol{R})\right] \\ &= \frac{1}{\sqrt{2}}\sum_\tau e^{i\tau\mathcal{K}\hat{\mathbf{x}}\cdot\boldsymbol{R}}\Psi_{\sigma,\tau}(\boldsymbol{R}). \end{aligned} \tag{2.6}$$

We take $\boldsymbol{R}$ to be on the triangular Bravais lattice, and add a sublattice index, $s = (A, B)$, so that there are two copies of the field operators for each atom in the unit cell, $\Psi_{\sigma,\tau}(\boldsymbol{R}) \to \Psi_{\sigma,\tau}(\boldsymbol{R}, s)$.

In the continuum limit, $\boldsymbol{R} \to \boldsymbol{r} = (x, y)$, and the field operators can be expanded in the basis of single particle Landau states. Following the formalism of section 1.4.1 and 1.4.2, the operators are given by

$$\begin{aligned}
\Psi_{\sigma,K}(\boldsymbol{r}, A) &= -\frac{1}{\sqrt{2}} \sum_{k,n} \mathrm{sgn}(n) h_{|n|-1,k}(\boldsymbol{r}) c_{nk\sigma K}, \\
\Psi_{\sigma,K}(\boldsymbol{r}, B) &= \frac{1}{\sqrt{2}} \sum_{k,n} \left(\sqrt{2}\right)^{\delta_{n,0}} h_{|n|,k}(\boldsymbol{r}) c_{nk\sigma K}, \\
\Psi_{\sigma,K'}(\boldsymbol{r}, A) &= \frac{1}{\sqrt{2}} \sum_{k,n} \left(\sqrt{2}\right)^{\delta_{n,0}} h_{|n|,k}(\boldsymbol{r}) c_{nk\sigma K'}, \\
\Psi_{\sigma,K'}(\boldsymbol{r}, B) &= \frac{1}{\sqrt{2}} \sum_{k,n} \mathrm{sgn}(n) h_{|n|-1,X}(\boldsymbol{r}) c_{nk\sigma K'},
\end{aligned} \tag{2.7}$$

where

$$\mathrm{sgn}(n) \equiv \begin{cases} -1 & \text{if } n < 0 \\ 0 & \text{if } n = 0 \\ 1 & \text{if } n > 0 \ , \end{cases} \tag{2.8}$$

plays the role of the band index. More specifically, we have made the replacement $\lambda \to \mathrm{sgn}(n)$, so that negative (positive) LL's are associated with the valence (conduction) band. The requirement that $\mathrm{sgn}(0) = 0$ ensures that the weights collapse onto a single sublattice when $n = 0$. In eq. (2.7), $h_{n,k}(\boldsymbol{r})$ are the Landau wave functions given in eq. (1.31). In the next section, the interactions will be introduced in terms of the discrete field operators, $\Psi(\boldsymbol{R})$. Once we have a handle on the form of the interactions, we will take the model to the continuum.

2.1 Model Hamiltonian

The Hamiltonian, $\mathcal{H} = \mathcal{H}_0 + \mathcal{H}_{\mathrm{int}}$, is separated into a single particle term, $\mathcal{H}_0$, and a two-body interaction term, $\mathcal{H}_{\mathrm{int}}$. In the basis described above, the continuum form of the single particle Hamiltonian is given in terms of the LL spectrum and Zeeman energy, and is written as

$$\mathcal{H}_0 = \sum_{n,k,\sigma,\tau} \left[\mathrm{sgn}(n) \frac{\hbar v_F}{\ell} \sqrt{2|n|} - \frac{\sigma g^* \mu_B}{2} B_T \right] c^\dagger_{\sigma\tau nk} c_{\sigma\tau nk}, \tag{2.9}$$

where $g^* = 2$ is the Landé factor, and μ_B is the Bohr magneton. The perpendicular field is related to the total field by $B_T = \epsilon_z B_\perp$, where ϵ_z is a dimensionless parameter that determines the strength of the Zeeman energy.

2.1.1 Graphene lattice interactions

The microscopic interactions consist of Hubbard-like on-site (OS) and nearest neighbor (NN) terms, which are treated as lattice scale corrections to the SU(4) symmetric Coulomb (C) interaction: $\mathcal{H}_{\rm int} = \mathcal{H}^{(\rm C)} + \mathcal{H}^{(\rm OS)} + \mathcal{H}^{(\rm NN)}$. We will first introduce the NN interaction, which can be written as

$$\begin{aligned}\mathcal{H}^{(\rm NN)} \equiv & \frac{V_1}{2} \sum_{\boldsymbol{R},\boldsymbol{R}'} \sum_{s,s'} \sum_{\sigma',\sigma} \big[1 - \delta_{s,s'}\big] \delta_{\boldsymbol{R},\boldsymbol{R}'} \\ & \times \Big[\Psi^\dagger_\sigma(\boldsymbol{R},s) \Psi^\dagger_{\sigma'}(\boldsymbol{R}',s') \Psi_{\sigma'}(\boldsymbol{R}',s') \Psi_\sigma(\boldsymbol{R},s) \\ & + \Psi^\dagger_\sigma(\boldsymbol{R},s) \Psi^\dagger_{\sigma'}(\boldsymbol{R}'+\boldsymbol{a}_1,s') \Psi_{\sigma'}(\boldsymbol{R}'+\boldsymbol{a}_1,s') \Psi_\sigma(\boldsymbol{R},s) \\ & + \Psi^\dagger_\sigma(\boldsymbol{R},s) \Psi^\dagger_{\sigma'}(\boldsymbol{R}'+\boldsymbol{a}_2,s') \Psi_{\sigma'}(\boldsymbol{R}'+\boldsymbol{a}_2,s') \Psi_\sigma(\boldsymbol{R},s) \Big],\end{aligned} \tag{2.10}$$

where $\boldsymbol{a}_1$ and $\boldsymbol{a}_2$ are primitive lattice vectors, and V_1 is the NN interaction strength. The three terms in eq. (2.10) are related by 120° lattice rotations, and, as long as the state does not break the 3-fold rotational symmetry, the expectation value for all three terms should be the same. We therefore drop the last two terms in eq. (2.10), and replace $V_1 \to 3V_1$.

Using eq. (2.6) to expand the fields in terms of the valley, the NN interaction becomes

$$\begin{aligned}\mathcal{H}^{(\rm NN)} = & \frac{3V_1}{8} \sum_{\boldsymbol{R},\boldsymbol{R}'} \sum_{s,s'} \sum_{\sigma,\sigma'} \sum_{\boldsymbol{\tau}} e^{i(\tau_4 - \tau_1 + \tau_3 - \tau_2)\mathcal{K}\hat{\mathbf{x}}\cdot\boldsymbol{R}} \big[1 - \delta_{s,s'}\big] \delta_{\boldsymbol{R},\boldsymbol{R}'} \\ & \times \Psi^\dagger_{\sigma,\tau_1}(\boldsymbol{R},s) \Psi^\dagger_{\sigma',\tau_2}(\boldsymbol{R}',s') \Psi_{\sigma',\tau_3}(\boldsymbol{R}',s') \Psi_{\sigma,\tau_4}(\boldsymbol{R},s),\end{aligned} \tag{2.11}$$

where, as a matter of notational convenience, the bold face on a discrete index will refer to the 4 component set of constituent labels (i.e., $\boldsymbol{\tau} = \{\tau_1, \tau_2, \tau_3, \tau_4\}$). Following a similar procedure, the

OS interaction takes the form

$$\begin{aligned}\mathcal{H}^{(\mathrm{OS})} \equiv \frac{V_0}{8} \sum_{\boldsymbol{R},\boldsymbol{R}'} \sum_{s,s'} \sum_{\sigma,\sigma'} \sum_{\boldsymbol{\tau}} e^{i(\tau_4-\tau_1+\tau_3-\tau_2)\mathcal{K}\hat{\mathbf{x}}\cdot\boldsymbol{R}} \delta_{s,s'}\delta_{\boldsymbol{R},\boldsymbol{R}'} \\ \times \Psi^{\dagger}_{\sigma,\tau_1}(\boldsymbol{R},s)\Psi^{\dagger}_{\sigma',\tau_2}(\boldsymbol{R}',s')\Psi_{\sigma',\tau_3}(\boldsymbol{R}',s')\Psi_{\sigma,\tau_4}(\boldsymbol{R},s),\end{aligned} \tag{2.12}$$

where V_0 is the OS interaction strength. We then assume that, for any state of interest, the expectation value of the four field operators, $\langle\Psi^{\dagger}(\boldsymbol{R})\Psi^{\dagger}(\boldsymbol{R}')\Psi(\boldsymbol{R}')\Psi(\boldsymbol{R})\rangle$, varies slowly on the lattice scale. Under this assumption, when we sum over $\boldsymbol{R}$ and $\boldsymbol{R}'$ in eq. (2.11) and eq. (2.12), only terms which do not rapidly oscillate will add a non-zero contribution to the sum.

To enforce this, the argument in the phase factor must vanish, giving following condition on the pseudospin:

$$\tau_4 - \tau_1 + \tau_3 - \tau_2 = 0. \tag{2.13}$$

This condition yields two possibilities:

$$\text{i) } \tau_1 = \tau_4, \tau_2 = \tau_3 \text{ and ii) } \tau_1 = \tau_3 \neq \tau_2 = \tau_4. \tag{2.14}$$

We can express possibility ii) in terms of Pauli matrices, τ_i, with $i = x, y, z$, in the pseudospin space as

$$\tau_1 = \tau_3 \neq \tau_2 = \tau_4 \longleftrightarrow \frac{1}{2}\Big[(\tau_x)_{\tau_1\tau_4}(\tau_x)_{\tau_2\tau_3} + (\tau_y)_{\tau_1\tau_4}(\tau_y)_{\tau_2\tau_3}\Big]. \tag{2.15}$$

When case ii) is written in this way, the microscopic interactions look very similar to the short range interactions, particularly the term accompanying the anisotropy energy, $u_{\perp}$, of Kharitonov's model in eq. (1.47). However, notice that, if the OS and NN interactions are projected into the $n = 0$ LL, both interactions vanish. This is because case ii) yields a non-zero result only if, for example, $\tau_1 \neq \tau_4$, whereas $\Psi^{\dagger}_{\sigma,\tau_1}(\boldsymbol{R},s)$ and $\Psi_{\sigma,\tau_4}(\boldsymbol{R},s)$ are evaluated on the same sublattice. In the basis of the Landau states, both of these field operators cannot be non-zero when $n = 0$. We emphasize this point as further motivation to keep non-zero LL's in the calculation.

The electron-electron (e-e) Coulomb interaction is written as

$$\mathcal{H}^{(\mathrm{C})} = \frac{1}{8}\sum_{\boldsymbol{R},\boldsymbol{R}'}\sum_{s,s'}\sum_{\sigma,\sigma'}\sum_{\boldsymbol{\tau}} e^{[i(\tau_4-\tau_1)\boldsymbol{R}+(\tau_3-\tau_2)\boldsymbol{R}']\cdot\mathcal{K}\hat{\mathbf{x}}}\frac{e^2}{|\boldsymbol{R}-\boldsymbol{R}'|} \times \Psi^{\dagger}_{\sigma,\tau_1}(\boldsymbol{R},s)\Psi^{\dagger}_{\sigma',\tau_2}(\boldsymbol{R}',s')\Psi_{\sigma',\tau_3}(\boldsymbol{R}',s')\Psi_{\sigma,\tau_4}(\boldsymbol{R},s), \tag{2.16}$$

where the same assumption is made about rapidly oscillating terms in the sum over $\boldsymbol{R}$ and $\boldsymbol{R}'$. That is, the phase factor in eq. (2.16) will oscillate rapidly unless we have the condition: $\tau_1 = \tau_4,\ \tau_2 = \tau_3$, which is the same result as case i) for the microscopic interactions. Thus, the Coulomb interaction is SU(4) symmetric in both spin and valley.

We summarize the conditions on the pseudospin index for all three interactions by making the replacement

$$e^{[i(\tau_4-\tau_1)\boldsymbol{R}+(\tau_3-\tau_2)\boldsymbol{R}']\cdot\mathcal{K}\hat{\mathbf{x}}} \to f^{(\mathrm{i})}(\boldsymbol{\tau}), \tag{2.17}$$

where the function,

$$f^{(\mathrm{i})}(\boldsymbol{\tau}) \equiv \delta_{\tau_1-\tau_4,\tau_3-\tau_2}\big[1-\delta_{\mathrm{i,C}}(1-\delta_{\delta_{\tau_1,\tau_4}})\big], \tag{2.18}$$

has the form $f^{(\mathrm{C})} = \delta_{\tau_1,\tau_4}\delta_{\tau_2,\tau_3}$, for the Coulomb interaction, and $f^{(\mathrm{OS})} = f^{(\mathrm{NN})} = \delta_{\tau_1-\tau_4,\tau_3-\tau_2}$, for the OS and NN interactions. We further note that these conditions are imposed so that any terms which oscillate rapidly are not included in the sum over $\boldsymbol{R}$ and $\boldsymbol{R}'$, for each interaction.

2.1.2 Interactions in the continuum

In the continuum limit, we make the substitution $\sum_{\boldsymbol{R}} \to \frac{1}{A_c}\int d\boldsymbol{r}$, where the normalization is given in terms of the area of the unit cell, A_c. Furthermore, the discrete field operators, $\Psi(\boldsymbol{R})$, are replaced by their continuum counterparts, $\Psi(\boldsymbol{R}) \to \sqrt{A_c}\Psi(\boldsymbol{r})$. The interactions now reads as

$$\mathcal{H}^{(\mathrm{i})} = \frac{1}{2}\sum_{s,s'}\sum_{\sigma,\sigma'}\sum_{\boldsymbol{\tau}}\int d\boldsymbol{r}d\boldsymbol{r}' f^{(\mathrm{i})}(\boldsymbol{\tau}) \times\Psi^{\dagger}_{\sigma\tau_1}(\boldsymbol{r},s)\Psi^{\dagger}_{\sigma'\tau_2}(\boldsymbol{r}',s')V^{(\mathrm{i})}(s,s';\ \boldsymbol{r}-\boldsymbol{r}')\Psi_{\sigma'\tau_3}(\boldsymbol{r}',s')\Psi_{\sigma\tau_4}(\boldsymbol{r},s), \tag{2.19}$$

where each interaction is specified by the index $\mathrm{i} = \mathrm{C}, \mathrm{OS}, \mathrm{NN}$.

Using the Fourier transform of the real space potential,

$$V^{(\mathrm{i})}(s,s';\boldsymbol{r}-\boldsymbol{r}') = \frac{1}{S}\sum_{\boldsymbol{q}} V^{(\mathrm{i})}(s,s';q)e^{i\boldsymbol{q}\cdot(\boldsymbol{r}-\boldsymbol{r}')}, \tag{2.20}$$

where $S = L_x L_y$ is the area of the sample and $\boldsymbol{q} = (q_x, q_y)$, the potentials read as:

$$\begin{aligned}
V^{(\mathrm{C})}(s,s';\boldsymbol{r}) &= \frac{1}{4}\frac{e^2}{|\boldsymbol{r}|}\ ,\ V^{(\mathrm{C})}(s,s';q) = \frac{1}{4}\frac{2\pi e^2}{q}\ ; \\
V^{(\mathrm{OS})}(s,s';\boldsymbol{r}) &= \frac{V_0 A_c}{4}\delta(\boldsymbol{r})\delta_{s,s'}\ ,\ V^{(\mathrm{OS})}(s,s';q) = \frac{V_0 A_c}{4}\delta_{s,s'}\ ; \\
V^{(\mathrm{NN})}(s,s';\boldsymbol{r}) &= \frac{3V_1 A_c}{4}\delta(\boldsymbol{r})\big[1-\delta_{s,s'}\big]\ ,\ V^{(\mathrm{NN})}(s,s';q) = \frac{3V_1 A_c}{4}\big[1-\delta_{s,s'}\big].
\end{aligned} \tag{2.21}$$

Expanding the field operators using eq. (2.7), the interactions are now given by

$$\begin{aligned}
\mathcal{H}^{(\mathrm{i})} = \frac{f^{(\mathrm{i})}(\boldsymbol{\tau})}{2S}\sum_{\boldsymbol{q}} V^{(\mathrm{i})}(s,s';q) &\int d\boldsymbol{r}\, \langle \boldsymbol{r}|\tau_1;n_1,k_1,s\rangle^* e^{i\boldsymbol{q}\cdot\boldsymbol{r}} \langle \boldsymbol{r}|\tau_4;n_4,k_4,s\rangle \\
&\times \int d\boldsymbol{r}'\, \langle \boldsymbol{r}'|\tau_2;n_2,k_2,s'\rangle^* e^{-i\boldsymbol{q}\cdot\boldsymbol{r}'} \langle \boldsymbol{r}'|\tau_3;n_3,k_3,s'\rangle \\
&\times c^\dagger_{\tau_1 n_1 k_1} c^\dagger_{\tau_2 n_2 k_2} c_{\tau_3 n_3 k_3} c_{\tau_4 n_4 k_4},
\end{aligned} \tag{2.22}$$

where a sum over repeated indices is now implied, and we have defined the functions,

$$\begin{aligned}
\langle \boldsymbol{r}|\tau=+1,n,k,s\rangle &= \frac{\sqrt{2}^{\delta_{n,0}}}{\sqrt{2}}\big[-\mathrm{sgn}(n)h_{|n|-1,k}(\boldsymbol{r})\delta_{s,A} + h_{|n|,k}(\boldsymbol{r})\delta_{s,B}\big], \\
\langle \boldsymbol{r}|\tau=-1,n,k,s\rangle &= \frac{\sqrt{2}^{\delta_{n,0}}}{\sqrt{2}}\big[h_{|n|,k}(\boldsymbol{r})\delta_{s,A} + \mathrm{sgn}(n)h_{|n|-1,k}(\boldsymbol{r})\delta_{s,B}\big].
\end{aligned} \tag{2.23}$$

We have also omitted the spin label, σ, for the present calculation. Its dependence on the interactions enters only in the c operators as a discrete label.

After a little work, it can be shown that

$$\int d\boldsymbol{r}\, \langle \boldsymbol{r}|\tau,n,k,s\rangle^* e^{i\boldsymbol{q}\cdot\boldsymbol{r}} \langle \boldsymbol{r}|\tau',n',k',s\rangle \equiv e^{iq_x(k+k')\ell^2/2} T^{\tau,\tau'}_{n,n'}(\boldsymbol{q},s)\delta_{k,k'-q_y}. \tag{2.24}$$

See Appendix A for more details regarding this integral. Notice that the sublattice dependence on the right hand side of eq. (2.24) only appears in the functions $T^{\tau,\tau'}_{n,n'}(\boldsymbol{q},s)$, which have the following

forms:

$$
\begin{aligned}
T^{1,-1}_{n,n'}(\boldsymbol{q},A) &= -\mathrm{sgn}(n)\frac{\sqrt{2}^{\delta_{n,0}+\delta_{n',0}}}{2}F_{|n|-1,\,|n'|}(\boldsymbol{q}),\\
T^{-1,1}_{n,n'}(\boldsymbol{q},A) &= -\mathrm{sgn}(n')\frac{\sqrt{2}^{\delta_{n,0}+\delta_{n',0}}}{2}F_{|n|,\,|n'|-1}(\boldsymbol{q}),\\
T^{1,-1}_{n,n'}(\boldsymbol{q},B) &= \mathrm{sgn}(n')\frac{\sqrt{2}^{\delta_{n,0}+\delta_{n',0}}}{2}F_{|n|,\,|n'|-1}(\boldsymbol{q}),\\
T^{-1,1}_{n,n'}(\boldsymbol{q},B) &= \mathrm{sgn}(n)\frac{\sqrt{2}^{\delta_{n,0}+\delta_{n',0}}}{2}F_{|n|-1,\,|n'|}(\boldsymbol{q}),\\
T^{1,1}_{n,n'}(\boldsymbol{q},A) &= \mathrm{sgn}(nn')\frac{\sqrt{2}^{\delta_{n,0}+\delta_{n',0}}}{2}F_{|n|-1,\,|n'|-1}(\boldsymbol{q}),\\
T^{-1,-1}_{n,n'}(\boldsymbol{q},A) &= \frac{\sqrt{2}^{\delta_{n,0}+\delta_{n',0}}}{2}F_{|n|,\,|n'|}(\boldsymbol{q}),\\
T^{1,1}_{n,n'}(\boldsymbol{q},B) &= T^{-1,-1}_{n,n'}(\boldsymbol{q},A),\\
T^{-1,-1}_{n,n'}(\boldsymbol{q},B) &= T^{1,1}_{n,n'}(\boldsymbol{q},A).
\end{aligned}
\tag{2.25}
$$

In eq. (2.25), we have introduced the form factors,

$$
F_{m,j}(\boldsymbol{q}) \equiv \left(\frac{j!}{m!}\right)^{1/2}\left[\frac{-q_y\ell + iq_x\ell}{\sqrt{2}}\right]^{m-j} e^{-q^2\ell^2/4}L_j^{m-j}(q^2\ell^2/2), \tag{2.26}
$$

for $m \geq j$, where $L_j^{\alpha}(x)$ is the generalized Laguerre polynomial. Note that $F_{m,j}(\boldsymbol{q}) = \left[F_{j,m}(-\boldsymbol{q})\right]^*$. The next step will be to sum the interactions over the sublattice indices. We define the interaction dependent functions,

$$
\mathcal{M}^{(\mathrm{i})}(\boldsymbol{n},\boldsymbol{\tau},\boldsymbol{q}) \equiv \sum_{s,s'} V^{(\mathrm{i})}(s,s';q)T^{\tau_1,\tau_4}_{n_1,n_4}(\boldsymbol{q},s)T^{\tau_2,\tau_3}_{n_2,n_3}(-\boldsymbol{q},s'). \tag{2.27}
$$

Noting the conditions on the pseudospin index, imposed by $f^{(\mathrm{i})}(\boldsymbol{\tau})$, the $\mathcal{M}$'s have the following forms for each interaction. For the Coulomb interaction,

$$
\begin{aligned}
\mathcal{M}^{(\mathrm{C})}(\boldsymbol{n},\tau,\tau',\tau',\tau,\boldsymbol{q}) = \frac{2\pi e^2}{4q}\big[&T^{\tau,\tau}_{n_1,n_4}(\boldsymbol{q},A)T^{\tau',\tau'}_{n_2,n_3}(-\boldsymbol{q},A) + T^{\tau,\tau}_{n_1,n_4}(\boldsymbol{q},A)T^{\tau',\tau'}_{n_2,n_3}(-\boldsymbol{q},B)\\
&+ T^{\tau,\tau}_{n_1,n_4}(\boldsymbol{q},B)T^{\tau',\tau'}_{n_2,n_3}(-\boldsymbol{q},A) + T^{\tau,\tau}_{n_1,n_4}(\boldsymbol{q},B)T^{\tau',\tau'}_{n_2,n_3}(-\boldsymbol{q},B)\big]
\end{aligned}
\tag{2.28}
$$

$$
\begin{aligned}
&= \frac{2\pi e^2}{4q} D(\boldsymbol{n}) \Big[F_{|n_1|,\,|n_4|}(\boldsymbol{q}) F_{|n_2|,\,|n_3|}(-\boldsymbol{q}) \\
&\qquad + \operatorname{sgn}(n_1 n_4) F_{|n_1|-1,\,|n_4|-1}(\boldsymbol{q}) F_{|n_2|,\,|n_3|}(-\boldsymbol{q}) \\
&\qquad + \operatorname{sgn}(n_2 n_3) F_{|n_1|,\,|n_4|}(\boldsymbol{q}) F_{|n_2|-1,\,|n_3|-1}(-\boldsymbol{q}) \\
&\qquad + \operatorname{sgn}(n_1 n_2 n_3 n_4) F_{|n_1|-1,\,|n_4|-1}(\boldsymbol{q}) F_{|n_2|-1,\,|n_3|-1}(-\boldsymbol{q}) \Big],
\end{aligned}
\tag{2.29}
$$

and is independent of whether $\tau = \tau'$ or $\tau \neq \tau'$. The term,

$$
D(\boldsymbol{n}) = \prod_{i=1}^{4} \sqrt{2}^{(\delta_{n_i,0}-1)},
\tag{2.30}
$$

ensures the correct normalization when one, or more, of the LL indices is zero.

For the OS interaction, the components of $\mathcal{M}$ with $\tau_1 = \tau_4$, $\tau_2 = \tau_3$ are

$$
\mathcal{M}^{(\mathrm{OS})}(\boldsymbol{n}, \tau, \tau', \tau', \tau, \boldsymbol{q}) = \frac{V_0 A_c}{4} \left[T^{\tau,\tau}_{n_1,n_4}(\boldsymbol{q}, A) T^{\tau',\tau'}_{n_2,n_3}(-\boldsymbol{q}, A) + T^{\tau,\tau}_{n_1,n_4}(\boldsymbol{q}, B) T^{\tau',\tau'}_{n_2,n_3}(-\boldsymbol{q}, B) \right]
$$

$$
\begin{aligned}
&= \frac{V_0 A_c}{4} D(\boldsymbol{n}) \Big[\Big(F_{|n_1|,\,|n_4|}(\boldsymbol{q}) F_{|n_2|,\,|n_3|}(-\boldsymbol{q}) \\
&\qquad + \operatorname{sgn}(n_1 n_2 n_3 n_4) F_{|n_1|-1,\,|n_4|-1}(\boldsymbol{q}) F_{|n_2|-1,\,|n_3|-1}(-\boldsymbol{q}) \Big) \delta_{\tau,\tau'} \\
&\qquad + \Big(\operatorname{sgn}(n_1 n_4) F_{|n_1|-1,\,|n_4|-1}(\boldsymbol{q}) F_{|n_2|,\,|n_3|}(-\boldsymbol{q}) \\
&\qquad + \operatorname{sgn}(n_2 n_3) F_{|n_1|,\,|n_4|}(\boldsymbol{q}) F_{|n_2|-1,\,|n_3|-1}(-\boldsymbol{q}) \Big) \delta_{\tau,-\tau'} \Big],
\end{aligned}
\tag{2.31}
$$

and the components with $\tau_1 = \tau_3 \neq \tau_2 = \tau_4$ are

$$
\mathcal{M}^{(\mathrm{OS})}(\boldsymbol{n}, \tau, \tau', \tau, \tau', \boldsymbol{q}) = \frac{V_0 A_c}{4} \left[T^{\tau,\tau'}_{n_1,n_4}(\boldsymbol{q}, A) T^{\tau',\tau}_{n_2,n_3}(-\boldsymbol{q}, A) + T^{\tau,\tau'}_{n_1,n_4}(\boldsymbol{q}, B) T^{\tau',\tau}_{n_2,n_3}(-\boldsymbol{q}, B) \right]
$$

$$
\begin{aligned}
&= \frac{V_0 A_c}{4} D(\boldsymbol{n}) \big[\operatorname{sgn}(n_2 n_4) F_{|n_1|,\,|n_4|-1}(\boldsymbol{q}) F_{|n_2|-1,\,|n_3|}(-\boldsymbol{q}) \\
&\qquad + \operatorname{sgn}(n_1 n_3) F_{|n_1|-1,\,|n_4|}(\boldsymbol{q}) F_{|n_2|,\,|n_3|-1}(-\boldsymbol{q}) \big],
\end{aligned}
\tag{2.32}
$$

with $\tau \neq \tau'$.

For the NN interaction, the components with $\tau_1 = \tau_4$, $\tau_2 = \tau_3$ are

$$\mathcal{M}^{(\mathrm{NN})}(\boldsymbol{n},\tau,\tau',\tau',\tau,\boldsymbol{q}) = \frac{3V_1A_c}{4}\left[T^{\tau,\tau}_{n_1,n_4}(\boldsymbol{q},A)T^{\tau',\tau'}_{n_2,n_3}(-\boldsymbol{q},B) + T^{\tau,\tau}_{n_1,n_4}(\boldsymbol{q},B)T^{\tau',\tau'}_{n_2,n_3}(-\boldsymbol{q},A)\right]$$

$$\begin{aligned}
&= \frac{3V_1A_c}{4}D(\boldsymbol{n})\Bigg[\Bigg(F_{|n_1|,\,|n_4|}(\boldsymbol{q})F_{|n_2|,\,|n_3|}(-\boldsymbol{q}) \\
&\qquad + \mathrm{sgn}(n_1n_2n_3n_4)F_{|n_1|-1,\,|n_4|-1}(\boldsymbol{q})F_{|n_2|-1,\,|n_3|-1}(-\boldsymbol{q})\Bigg)\delta_{\tau,-\tau'} \\
&\qquad + \Bigg(\mathrm{sgn}(n_1n_4)F_{|n_1|-1,\,|n_4|-1}(\boldsymbol{q})F_{|n_2|,\,|n_3|}(-\boldsymbol{q}) \\
&\qquad + \mathrm{sgn}(n_2n_3)F_{|n_1|,\,|n_4|}(\boldsymbol{q})F_{|n_2|-1,\,|n_3|-1}(-\boldsymbol{q})\Bigg)\delta_{\tau,\tau'}\Bigg].
\end{aligned} \tag{2.33}$$

Notice that this expression is very similar to $\mathcal{M}^{(\mathrm{OS})}(\boldsymbol{n},\tau,\tau',\tau',\tau,\boldsymbol{q})$ since

$$\mathcal{M}^{(\mathrm{OS})}(\boldsymbol{n},\tau,\tau',\tau',\tau,\boldsymbol{q}) = \frac{V_0}{3V_1}\left[\mathcal{M}^{(\mathrm{NN})}(\boldsymbol{n},\tau,-\tau,-\tau,\tau,\boldsymbol{q})\delta_{\tau,\tau'} + \mathcal{M}^{(\mathrm{NN})}(\boldsymbol{n},\tau,\tau,\tau,\tau,\boldsymbol{q})\delta_{\tau,-\tau'}\right]. \tag{2.34}$$

For the case when $\tau_1 = \tau_3 \neq \tau_2 = \tau_4$, we have

$$\mathcal{M}^{(\mathrm{NN})}(\boldsymbol{n},\tau,\tau',\tau,\tau',\boldsymbol{q}) = \frac{3V_1A_c}{4}\left[T^{\tau,\tau'}_{n_1,n_4}(\boldsymbol{q},A)T^{\tau',\tau}_{n_2,n_3}(-\boldsymbol{q},B) + T^{\tau,\tau'}_{n_1,n_4}(\boldsymbol{q},B)T^{\tau',\tau}_{n_2,n_3}(-\boldsymbol{q},A)\right]$$

$$\begin{aligned}
&= -\frac{3V_1A_c}{4}D(\boldsymbol{n})\big[\mathrm{sgn}(n_3n_4)F_{|n_1|,\,|n_4|-1}(\boldsymbol{q})F_{|n_2|,\,|n_3|-1}(-\boldsymbol{q}) \\
&\qquad + \mathrm{sgn}(n_1n_2)F_{|n_1|-1,\,|n_4|}(\boldsymbol{q})F_{|n_2|-1,\,|n_3|}(-\boldsymbol{q})\big],
\end{aligned} \tag{2.35}$$

with $\tau \neq \tau'$. In terms of the $\mathcal{M}$'s, the interactions can now be written as

$$\begin{aligned}
\mathcal{H}^{(\mathrm{i})} = \frac{f^{(\mathrm{i})}(\boldsymbol{\tau})}{2S}\sum_{\boldsymbol{q}}\mathcal{M}^{(\mathrm{i})}(\boldsymbol{n},\boldsymbol{\tau},\boldsymbol{q})\delta_{k_1,k_4-q_y}\delta_{k_2,k_3+q_y}e^{iq_x(k_1+k_4-k_2-k_3)\ell^2/2} \\
\times c^\dagger_{\tau_1n_1k_1}c^\dagger_{\tau_2n_2k_2}c_{\tau_3n_3k_3}c_{\tau_4n_4k_4}.
\end{aligned} \tag{2.36}$$

2.2 Hartree-Fock approximation

In the Hartree-Fock (HF) approximation, we assume that the ground state can be written in terms of a single Slater determinant. The two body interactions are replaced by single particle interactions, with effective potentials that are written in terms of direct (D) and exchange (X)

components. Under this mean field approximation, the interactions become

$$\begin{aligned}\mathcal{H}^{(\mathrm{i})} \to \mathcal{H}^{(\mathrm{i})}_{\mathrm{HF}} &= \frac{f^{(\mathrm{i})}(\boldsymbol{\tau})}{S}\sum_{\boldsymbol{q}} \mathcal{M}^{(\mathrm{i})}(\boldsymbol{n},\boldsymbol{\tau},\boldsymbol{q})\delta_{k_1,k_4-q_y}\delta_{k_2,k_3+q_y}e^{iq_x(k_1+k_4-k_2-k_3)\ell^2/2} \\ &\quad\times\left[\,\langle c_1^\dagger c_4\rangle\, c_2^\dagger c_3 - \langle c_1^\dagger c_3\rangle\, c_2^\dagger c_4\right] \\ &\equiv \mathcal{H}^{(\mathrm{i})}_{\mathrm{D}} - \mathcal{H}^{(\mathrm{i})}_{\mathrm{X}},\end{aligned} \tag{2.37}$$

where $\langle c^\dagger c\rangle$ is the density matrix, which is chosen as the order parameter for this analysis. The full HF Hamiltonian, $\mathcal{H}_{\mathrm{HF}}$, can then be written as $\mathcal{H}_{\mathrm{HF}} = \mathcal{H}_0 + \mathcal{H}^{(\mathrm{C})}_{\mathrm{HF}} + \mathcal{H}^{(\mathrm{OS})}_{\mathrm{HF}} + \mathcal{H}^{(\mathrm{NN})}_{\mathrm{HF}}$, where $\mathcal{H}_0$, defined in eq. (2.9), is the single particle contribution to the underlying Hamiltonian. The rest of this chapter will focus on states which exist exactly at $\nu = 0$. At integer filling, we expect the states to be spatially uniform, which forces the density matrix to have the form

$$\langle c^\dagger_{\tau n k} c_{\tau' n' k'}\rangle = \delta_{k,k'}\,\langle c^\dagger_{\tau n} c_{\tau' n'}\rangle\,. \tag{2.38}$$

Although it was not included explicitly in the Hamiltonian for this model, there is a Coulomb interaction between the electrons and the positively charged atoms in the (uniform) background. The energy associated with that interaction is divergent. However, the Hartree (direct) potential for the e-e Coulomb interaction, which is also divergent, exactly cancels the divergence of the electron-background. For uniform states, we therefore include only the exchange term for the e-e Coulomb interaction in the HF Hamiltonian, and take $\mathcal{H}^{(\mathrm{C})}_{\mathrm{D}} \to 0$.

In what follows, we first focus on the exchange terms for each interaction. Afterwards, we will deal with the direct terms. With the delta function restriction in eq. (2.38), the exchange operator for all three interactions becomes

$$\begin{aligned}\mathcal{H}^{(\mathrm{i})}_{\mathrm{X}} &= \frac{f^{(\mathrm{i})}(\boldsymbol{\tau})}{S}\sum_{\boldsymbol{q},k} \mathcal{M}^{(\mathrm{i})}(\boldsymbol{n},\boldsymbol{\tau},\boldsymbol{q})\,\langle c^\dagger_{\tau_1 n_1} c_{\tau_3 n_3}\rangle\, c^\dagger_{\tau_2 n_2 k} c_{\tau_4 n_4 k} \\ &= f^{(\mathrm{i})}(\boldsymbol{\tau})\int \frac{d\boldsymbol{q}}{(2\pi)^2}\mathcal{M}^{(\mathrm{i})}(\boldsymbol{n},\boldsymbol{\tau},\boldsymbol{q})\,\langle c^\dagger_{\tau_1 n_1} c_{\tau_3 n_3}\rangle \sum_k c^\dagger_{\tau_2 n_2 k} c_{\tau_4 n_4 k}.\end{aligned} \tag{2.39}$$

Note that now the dependence on k only appears in the c operators.

A generic term in $\mathcal{M}$ has the form of a product of two form factors, and so the integral of

interest here is

$$\begin{aligned} I_{\mathrm{X}}^{(\mathrm{C})}(\boldsymbol{n}) &\equiv \int \frac{d\boldsymbol{q}}{(2\pi)^2}\frac{2\pi e^2}{4q}F_{n_1,n_4}(\boldsymbol{q})F_{n_2,n_3}(-\boldsymbol{q}) \\ &= \frac{\sqrt{2}e^2}{4\ell}J^{|n_1-n_4|}_{\min(n_1,n_4),\min(n_2,n_3)}\delta_{n_1-n_4,n_3-n_2} \end{aligned} \tag{2.40}$$

for the Coulomb interaction, where

$$J^{\alpha}_{n,m} = \left(\frac{n!\ m!}{(\alpha+n)!\ (\alpha+m)!}\right)^{\frac{1}{2}}\int_0^\infty dx\ x^{2\alpha}e^{-x^2}L_n^\alpha(x^2)L_m^\alpha(x^2). \tag{2.41}$$

The restriction on LL's, $\delta_{n_1-n_4,n_3-n_2}$, comes from the angular integral over $\boldsymbol{q}$, and use of min() ensures that the requirement on the form factors, $F_{n,m}(\boldsymbol{q})$ with $n \geq m$, carries through the integral. The remaining integral over x is solved numerically. The OS and NN exchange integrals are

$$\begin{aligned} I_{\mathrm{X}}^{(\mathrm{OS})}(\boldsymbol{n}) &\equiv \int \frac{d\boldsymbol{q}}{(2\pi)^2}\frac{V_0A_c}{4}F_{n_1,n_4}(\boldsymbol{q})F_{n_2,n_3}(-\boldsymbol{q}) \\ &= \frac{V_0A_c}{8\pi\ell^2}\delta_{n_1,n_3}\delta_{n_2,n_4} \end{aligned} \tag{2.42}$$

and

$$\begin{aligned} I_{\mathrm{X}}^{(\mathrm{NN})}(\boldsymbol{n}) &\equiv \int \frac{d\boldsymbol{q}}{(2\pi)^2}\frac{3V_1A_c}{4}F_{n_1,n_4}(\boldsymbol{q})F_{n_2,n_3}(-\boldsymbol{q}) \\ &= \frac{3V_1A_c}{8\pi\ell^2}\delta_{n_1,n_3}\delta_{n_2,n_4}, \end{aligned} \tag{2.43}$$

which follows directly from the orthogonality of generalized Laguerre polynomials, and the requirement on the form factors mentioned above.

Using $\langle c^\dagger_{\tau_1 n_1 k_1}c_{\tau_4 n_4 k_4}\rangle = \delta_{k_1,k_4}\langle c^\dagger_{\tau_1 n_1}c_{\tau_4 n_4}\rangle$ in the direct term, which only involves the OS and NN interactions, leads to

$$\mathcal{H}_{\mathrm{D}}^{(\mathrm{i})} = \frac{f^{(\mathrm{i})}(\boldsymbol{\tau})}{2\pi\ell^2}\mathcal{M}^{(\mathrm{i})}(\boldsymbol{n},\boldsymbol{\tau},\boldsymbol{q}=0)\langle c^\dagger_{\tau_1 n_1}c_{\tau_4 n_4}\rangle\sum_k c^\dagger_{\tau_2 n_2 k}c_{\tau_3 n_3 k}, \tag{2.44}$$

where we have used the fact that $\sum_k e^{iq_xk\ell^2} = \frac{S}{2\pi\ell^2}\delta_{q_x,0}$. The product of form factors in $\mathcal{M}$ are now being evaluated at $\boldsymbol{q}=0$. In that case, the only way to yield a non-zero result is if

$$F_{n_1,n_4}(\boldsymbol{q}=0)F_{n_2,n_3}(\boldsymbol{q}=0) = \delta_{n_1,n_4}\delta_{n_2,n_3}. \tag{2.45}$$

We summarize these results by defining

$$\mathcal{T}_{\mathrm{X}}^{(\mathrm{i})}(\boldsymbol{n},\boldsymbol{\tau}) \equiv \int \frac{d\boldsymbol{q}}{(2\pi)^2}\mathcal{M}^{(\mathrm{i})}(\boldsymbol{n},\boldsymbol{\tau},\boldsymbol{q}) \tag{2.46}$$

and

$$\mathcal{T}_{\rm D}^{(\rm i)}(\boldsymbol{n},\boldsymbol{\tau}) \equiv \frac{1}{2\pi\ell^2}\mathcal{M}^{(\rm i)}(\boldsymbol{n},\boldsymbol{\tau},\boldsymbol{q}=0), \tag{2.47}$$

where direct term is only associated with the OS and NN interactions. For the Coulomb interaction, since the form of $\mathcal{M}^{(\rm C)}$ in eq. (2.29) is independent of the pseudospin indices, we will drop the $\boldsymbol{\tau}$ dependence on $\mathcal{T}_{\rm X}^{(\rm C)}$, and write

$$\begin{aligned}\mathcal{T}_{\rm X}^{(\rm C)}(\boldsymbol{n}) = D(\boldsymbol{n})\Big[& I^{(\rm C)}\big(|n_1|,|n_2|,|n_3|,|n_4|\big) \\ & +\mathrm{sgn}(n_1n_4)I^{(\rm C)}\big(|n_1|-1,|n_2|,|n_3|,|n_4|-1\big) \\ & +\mathrm{sgn}(n_2n_3)I^{(\rm C)}\big(|n_1|,|n_2|-1,|n_3|-1,|n_4|\big) \\ & +\mathrm{sgn}(n_1n_2n_3n_4)I^{(\rm C)}\big(|n_1|-1,|n_2|-1,|n_3|-1,|n_4|-1\big)\Big].\end{aligned} \tag{2.48}$$

The OS and NN terms, $\mathcal{T}_{\rm D}^{(\rm OS)}(\boldsymbol{n},\boldsymbol{\tau})$, $\mathcal{T}_{\rm X}^{(\rm OS)}(\boldsymbol{n},\boldsymbol{\tau})$, $\mathcal{T}_{\rm D}^{(\rm NN)}(\boldsymbol{n},\boldsymbol{\tau})$, and $\mathcal{T}_{\rm X}^{(\rm NN)}(\boldsymbol{n},\boldsymbol{\tau})$ are all written out explicitly in Appendix B.

Including the spin label, the full HF Hamiltonian now becomes

$$\begin{aligned}\mathcal{H}_{\rm HF} = & \sum_{n,\sigma,\tau}\left[\mathrm{sgn}(n)\frac{\hbar v_F}{\ell}\sqrt{2|n|} - \frac{\sigma g^*\mu_B}{2}B_T\right]c^\dagger_{\sigma\tau n}c_{\sigma\tau n} \\ & + \sum_{\boldsymbol{n},\boldsymbol{\tau}}\delta_{\tau_1-\tau_4,\tau_2-\tau_3}\left[\mathcal{T}_{\rm D}^{(\rm OS)}(\boldsymbol{n},\boldsymbol{\tau}) + \mathcal{T}_{\rm D}^{(\rm NN)}(\boldsymbol{n},\boldsymbol{\tau})\right]\sum_{\sigma,\sigma'}\langle c^\dagger_{\sigma'\tau_1n_1}c_{\sigma'\tau_4n_4}\rangle\, c^\dagger_{\sigma\tau_2n_2}c_{\sigma\tau_3n_3} \\ & - \sum_{\boldsymbol{n},\boldsymbol{\tau}}\delta_{\tau_1-\tau_4,\tau_2-\tau_3}\left[\mathcal{T}_{\rm X}^{(\rm OS)}(\boldsymbol{n},\boldsymbol{\tau}) + \mathcal{T}_{\rm X}^{(\rm NN)}(\boldsymbol{n},\boldsymbol{\tau})\right]\sum_{\sigma,\sigma'}\langle c^\dagger_{\sigma\tau_1n_1}c_{\sigma'\tau_3n_3}\rangle\, c^\dagger_{\sigma'\tau_2n_2}c_{\sigma\tau_4n_4} \\ & - \sum_{\boldsymbol{n},\boldsymbol{\tau}}\delta_{\tau_1,\tau_4}\delta_{\tau_2,\tau_3}\mathcal{T}_{\rm X}^{(\rm C)}(\boldsymbol{n})\sum_{\sigma,\sigma'}\langle c^\dagger_{\sigma\tau_1n_1}c_{\sigma'\tau_3n_3}\rangle\, c^\dagger_{\sigma'\tau_2n_2}c_{\sigma\tau_4n_4},\end{aligned} \tag{2.49}$$

where we have dropped the labeling of, and sum over, k since it is diagonal in all $c^\dagger c$ operators. In the next section, we will restrict, in a tunable way, the number of LL's which are kept in the sums in eq. (2.49). This is done to avoid diagonalizing very large matrices in the numerical calculation. A discussion of the numerical HF method is also given at the end of the next section.

2.3 Landau levels in the Dirac sea

In principle, an exact calculation of the ground state for this model would require including every accessible LL, n, such that $n \geq -n_c$, where n_c, given in eq. (1.35), is the lowest (most negative) accessible LL, and is determined by assuming that there is only one electron per carbon atom. Keeping this many LL's in the calculation is numerically challenging. For example, with a magnetic field of $B_\perp = 15\text{T}$, $n_c \approx 2500$. It is also possible for mixing between negative and positive energy LL's, so the full range for a LL index would be $-n_c \leq n \leq n_c$. Given the spin and pseudospin indices, this would require diagonalization of matrices that are on the order of 20,000 by 20,000 in size. Furthermore, numerical HF, as discussed at the end of this section, is an iterative method, and so we would need to diagonalize these matrices (potentially) many times.

To avoid this issue, any LL which is not actively included in the calculation is assumed to be filled. These filled LL's are associated with the Dirac sea, and are inactive in the sense that they cannot admix with active LL's. The range of active LL's is centered around $n = 0$, so that particle-hole symmetry is preserved. The range of LL's in the active "window" is $-n_w \leq n \leq n_w$, where n_w denotes the highest active LL index, while $-n_c \leq n < n_w$ is the range for LL's in the sea. Any LL with $n > n_w$ is neglected in the calculation. The total number of active LL's is then

$$N \equiv 2n_w + 1. \tag{2.50}$$

Fig. 2.1 shows a diagram summarizing the LL structure. Because the states in the sea are "frozen" out, we require the density matrix to be diagonal in all state indices, so that

$$\langle c^\dagger_{\sigma\tau n} c_{\sigma'\tau'n'} \rangle = \delta_{\sigma,\sigma'}\delta_{\tau,\tau'}\delta_{n,n'}, \tag{2.51}$$

for $-n_c \leq n < -n_w$. The sea will therefore appear as an effective potential to the remaining active LL's.

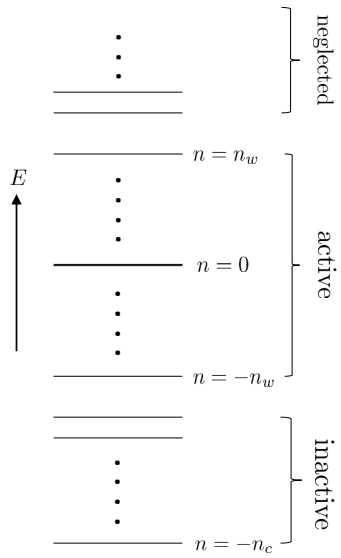

Figure 2.1: Schematic of the LL structure for this model. Inactive levels are assumed to be filled, and do not admix with levels in the active window.

For the Coulomb interaction, this generates a term in the HF Hamiltonian of the form

$$\mathcal{H}^{(\mathrm{C})}_{\mathrm{HF,sea}} = -\sum_{n_2,n_4=-n_w}^{n_w}\left[\sum_{n=-n_c}^{-n_w-1}\mathcal{T}^{(\mathrm{C})}_{\mathrm{X}}(n,n_2,n,n_4)\right]\sum_{\sigma,\tau}c^{\dagger}_{\sigma\tau n_2}c_{\sigma\tau n_4}. \tag{2.52}$$

We define

$$\begin{aligned}\mathcal{T}^{(\mathrm{C})}_{\mathrm{sea}}(n_2,n_4) &\equiv \sum_{n=-n_c}^{-n_w-1}\mathcal{T}^{(\mathrm{C})}_{\mathrm{X}}(n,n_2,n,n_4)\\ &= \frac{\sqrt{2}e^2}{4\ell}\sum_{n=-n_c}^{-n_w-1}\delta_{|n_2|,|n_4|}A(n_2,n_4,n),\end{aligned} \tag{2.53}$$

with

$$A(n_2,n_4,n) \equiv \begin{cases} \frac{1}{4}\left[J^{|n|-|n'|}_{|n'|,|n'|} - J^{|n|-|n'|}_{|n'|-1,|n'|-1}\right] & \text{if } n_2n_4<0 \quad (|n'| = |n_2| = |n_4|)\\ \frac{1}{2}J^{|n|}_{0,0} & \text{if } n_2=n_4=0\\ \frac{1}{4}\left[J^{|n|-|n'|}_{|n'|,|n'|} - sgn(n')\ 2J^{|n|-|n'|}_{|n'|-1,|n'|} - J^{|n|-|n'|}_{|n'|-1,|n'|-1}\right] & \text{if } n_2n_4>0 \quad (n'=n_2=n_4).\end{cases} \tag{2.54}$$

The details in going from eq. (2.53) to eq. (2.54) are given in Appendix B. Dirac sea contributions from the OS and NN interactions are actually diagonal in all state indices; thus, aside from a constant shift in the energy, which we will drop, they have no effect on the active window. This is

also shown in Appendix B. The only non-trivial contribution from electrons in the filled sea comes from the Coulomb interaction.

We now arrive at the final form of the HF Hamiltonian for our model of uniform states. It is written as

$$
\begin{aligned}
\mathcal{H}_{\mathrm{HF}} = & \\
& \sum_{n,n'=-n_w}^{n_w} \sum_{\sigma} \left[\mathrm{sgn}(n) \frac{\hbar v_F}{\ell} \sqrt{2|n|} \delta_{n,n'} - \frac{\sigma g^* \mu_B}{2} B_T \delta_{n,n'} - \mathcal{T}^{(\mathrm{C})}_{\mathrm{sea}}(n,n') \right] \sum_{\tau} c^\dagger_{\sigma\tau n} c_{\sigma\tau n'} \\
& + \sum_{\boldsymbol{n},\boldsymbol{\tau}} \delta_{\tau_1-\tau_4,\tau_2-\tau_3} \left[\mathcal{T}^{(\mathrm{OS})}_{\mathrm{D}}(\boldsymbol{n},\boldsymbol{\tau}) + \mathcal{T}^{(\mathrm{NN})}_{\mathrm{D}}(\boldsymbol{n},\boldsymbol{\tau}) \right] \sum_{\sigma,\sigma'} \langle c^\dagger_{\sigma'\tau_1 n_1} c_{\sigma'\tau_4 n_4} \rangle \, c^\dagger_{\sigma\tau_2 n_2} c_{\sigma\tau_3 n_3} \\
& - \sum_{\boldsymbol{n},\boldsymbol{\tau}} \delta_{\tau_1-\tau_4,\tau_2-\tau_3} \left[\mathcal{T}^{(\mathrm{OS})}_{\mathrm{X}}(\boldsymbol{n},\boldsymbol{\tau}) + \mathcal{T}^{(\mathrm{NN})}_{\mathrm{X}}(\boldsymbol{n},\boldsymbol{\tau}) \right] \sum_{\sigma,\sigma'} \langle c^\dagger_{\sigma\tau_1 n_1} c_{\sigma'\tau_3 n_3} \rangle \, c^\dagger_{\sigma'\tau_2 n_2} c_{\sigma\tau_4 n_4} \\
& - \sum_{\boldsymbol{n},\boldsymbol{\tau}} \delta_{\tau_1,\tau_4} \delta_{\tau_2,\tau_3} \mathcal{T}^{(\mathrm{C})}_{\mathrm{X}}(\boldsymbol{n}) \sum_{\sigma,\sigma'} \langle c^\dagger_{\sigma\tau_1 n_1} c_{\sigma'\tau_3 n_3} \rangle \, c^\dagger_{\sigma'\tau_2 n_2} c_{\sigma\tau_4 n_4},
\end{aligned}
\tag{2.55}
$$

where each LL index, n_i, with $-n_w \leq n_i \leq n_w$, only includes LL's belonging to the active window. From here, we construct the HF matrix by first choosing an initial density matrix. The HF matrix is then diagonalized, and its eigenvectors are used to construct a new density matrix, which is then iteratively fed back into the HF matrix.

The iterative process is repeated until the difference between two consecutive density matrices reaches a small tolerance value, χ. The difference, or error, for the i^{th} iteration is defined as

$$
\mathrm{err}(i) \equiv \frac{\sum_{n,n'} \sum_{\sigma,\sigma'} \sum_{\tau,\tau'} \left| \rho^{i}_{nn'\sigma\sigma'\tau\tau'} - \rho^{i-1}_{\sigma\sigma'\tau\tau' nn'} \right|}{\sum_{n,n'} \sum_{\sigma,\sigma'} \sum_{\tau,\tau'} \left[\left(\rho^{i}_{nn'\sigma\sigma'\tau\tau'} \right)^* \rho^{i}_{\sigma\sigma'\tau\tau' nn'} \right]^{1/2}},
\tag{2.56}
$$

with $\rho_{\sigma\sigma'\tau\tau' nn'} \equiv \langle c^\dagger_{\sigma\tau n} c_{\sigma'\tau' n'} \rangle$. The range for the tolerance value for a typical trial run is $10^{-10} \leq \chi \leq 10^{-8}$, and the density matrix is said to be converged when err $\leq \chi$. A converged density matrix represents a possible ground state solution to the HF Hamiltonian, and has energy that is (locally) minimized.

The number of iterations needed to reach convergence can vary. For example, when the energy landscape flattens out with respect to the parameters in the system, there is very little guidance as to what direction the HF algorithm should step towards in the parameter space in order to

minimize the energy. Such a situation can be realized near a continuous phase transition. Trial runs near those transitions can cycle through thousands of iterations (1,000 - 20,000) before reaching convergence. This phenomenon is called critical slowing down. In other regions of the parameter space, where the energy surface more steeply approaches a minimum, the number of iterations needed to reach convergence can be on the order of a few hundred. A solution may also reside on a saddle point in the parameter space. Such a solution is called unstable, and may appear to be converged; however, small deviations, added in either by hand or from numerical sensitivities, can cause the solution to drift away from convergence. Several challenges can arise in numerical HF, especially when the number of degrees of freedom in the system are large. Overcoming those challenges can be quite tedious. There are many techniques and methods for coaxing out converged solutions, which we do not discuss here.

2.4 Results

In this section, we discuss the results of numerical HF for our model of uniform states at filling factor $\nu = 0$. The initial guess for the density matrix is taken to be diagonal in LL index for all trial runs, and states with $-n_w \leq n < 0$ are taken to be completely filled. At $\nu = 0$, the $n = 0$ LL is occupied by two electrons. Their spin and pseudospin structure are built into the $n = 0$ component of the density matrix. The $(\uparrow\downarrow \otimes KK')$ structure for the zeroth LL (zLL) is chosen to resemble the states described in section 1.6, following Ref. [6]. In addition to the FM, CAF, CDW, and KD states, we also consider the anti-ferromagnet (AF), which is only stable when the Zeeman field is neglected. Once a density matrix is converged, the state is determined by its structure in the $n = 0$ LL.

The number of LL's in the active window, N, is treated as a tunable parameter in this analysis. For $N > 1$, in all converged ground states, we find that the program self-consistently generates LL mixing (LLM) terms only between particle-hole pairs, despite having started with a density matrix

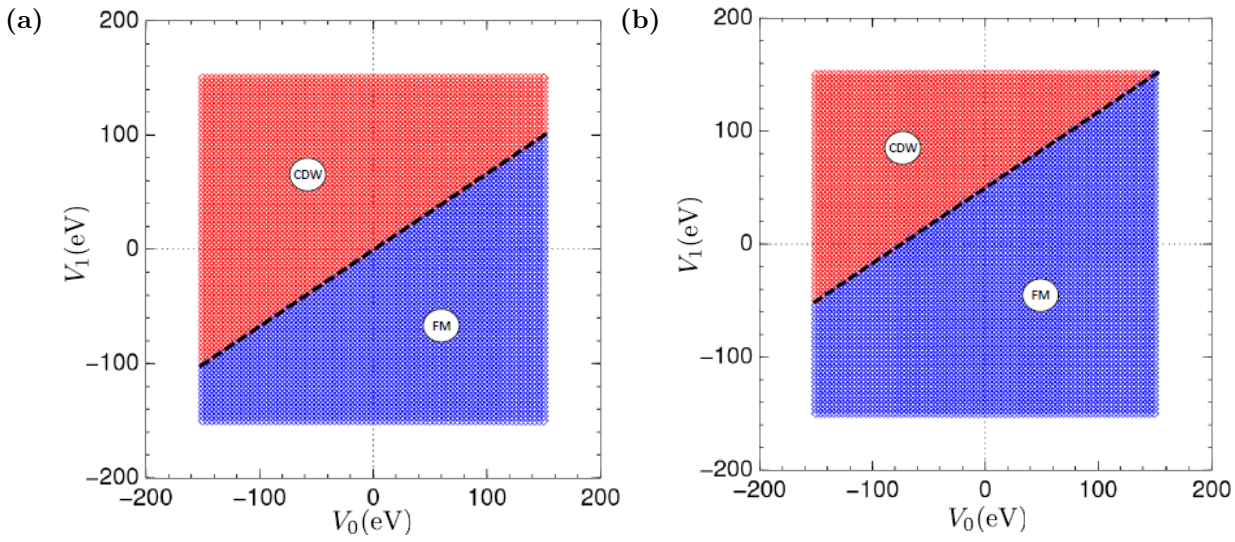

Figure 2.2: Phase diagrams for $N = 1$. (a) Diagram for $\epsilon_z \approx 0$. The FM (blue) and CDW (red) are degenerate at $V_0 = V_1 = 0$. (b) Diagram for $\epsilon_z = 2$.

that is diagonal in LL index. In what follows, we will present phase diagrams in the N-V_0-V_1-ϵ_z parameter space. Recall that ϵ_z is a measure of the Zeeman field strength, and is defined in terms of the total field, $B_T = \epsilon_z B_\perp$. The perpendicular field is fixed with magnitude $B_\perp = 15$T throughout the calculation.

2.4.1 V_0-V_1 phase diagrams

We first present results of the phase diagrams within the 2D space of the OS and NN interaction parameters, for fixed ϵ_z. For each value of V_0 and V_1, we input, as an initial guess for the density matrix, states representing the CDW, FM, KD, AF, and CAF phases. The ground state energy was compared for all converged solutions, and the HF ground state was determined by whichever state had the lowest energy.

Fig. 2.2a shows the phase diagram for $N = 1$ and $\epsilon_z \approx 0$. Notice that only the CDW and FM phases appear in this diagram. The boundary shared between the two phases is first order. When the OS interaction is attractive, electrons tend to occupy the same sublattice. In the $n = 0$

LL, each sublattice exactly coincides with a single valley; hence, the valley polarized CDW appears primarily for $V_0 < 0$. For a repulsive OS interaction, the two electrons occupy different valleys, and, in the presence of an infinitesimal Zeeman field, it is favorable for the electrons to be spin polarized. We note that in the complete absence of a Zeeman field, the AF and FM states become exactly degenerate, for $N = 1$. Fig. 2.2b shows the phase diagram for a larger value of the Zeeman field ($\epsilon_z = 2$). On a more general note, we also find that the KD phase is never the lowest energy solution for any set of parameters that we consider, despite being a stable solution for some parameter range.

When we allow for the possibility of LLM ($N > 1$), the situation becomes more interesting. Fig. 2.3a shows the phase diagram for $N = 3$ and $\epsilon_z = 0$. The AF phase now appears in a portion of the diagram, and the phase boundaries between all three phases are first order. In Fig. 2.3b, we show the phase diagram for $N = 3$ and $\epsilon_z = 2$. Similar to the case for a single LL ($N = 1$), the FM now takes up more space in the diagram, however, now, the AF is replaced by the CAF.

The boundary between the CAF and FM is second order, and the transition from CAF to FM is described by a continuous evolution of the canting angle. When the angle goes to zero, the electrons become fully spin polarized along the direction of the Zeeman field. Transitions between FM-CDW and CAF-CDW remain first order. The observation that the FM state fills a larger region of the parameter space, as the Zeeman field is increased, is consistent with the transport experiment in Ref. [14]. Note that $N = 3$ is the smallest window size in which the CAF phase can be realized. This result was also observed in Ref. [20]. We will return to this point in Chapters 4 and 5.

The OS and NN coupling strengths for a real sample of graphene are likely to both be positive. We therefore expect a real experiment to occur somewhere in the first quadrant of the phase diagrams above. Notice that the CAF-FM transition for $N = 3$ (Fig. 2.3b) occurs at a very large value (~ 300 eV) of the OS Hubbard parameter. This value is nonphysical; the estimates for the Hubbard parameters specific to graphene are on the order of a few eVs[33]. This is resolved by including more active LL's in the calculation. Fig. 2.4 shows the phase diagram for $N = 5$ and

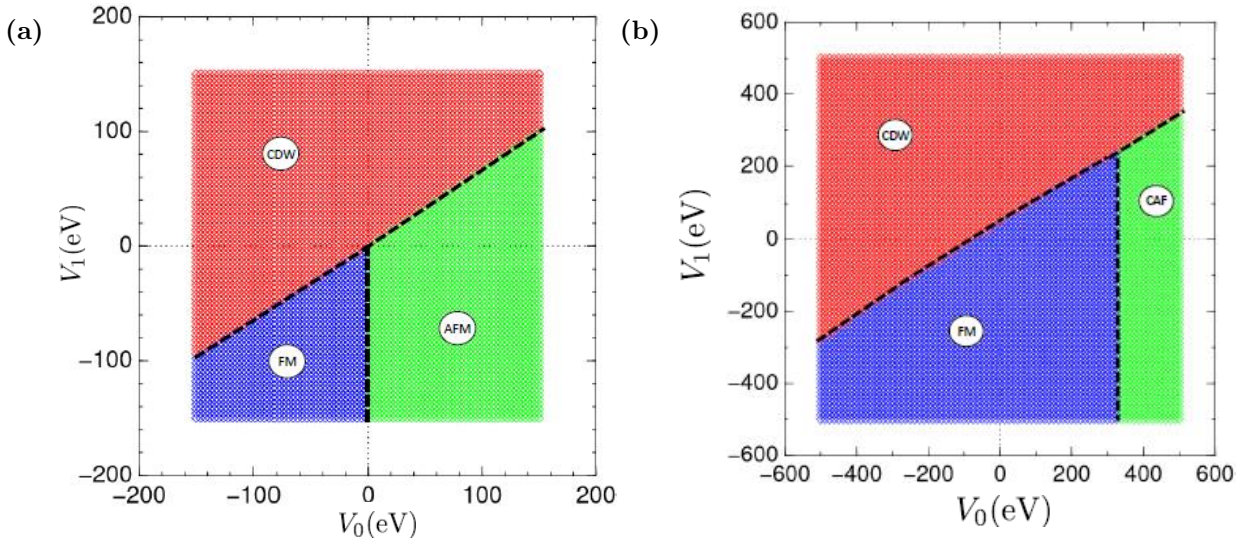

Figure 2.3: (a) Phase diagram for $N = 3$ and $\epsilon_z = 0$. The FM is still a stable solution in the region where the AF (green) now appears, but is higher in energy. (b) Phase diagram for $N = 3$ and $\epsilon_z = 2$.

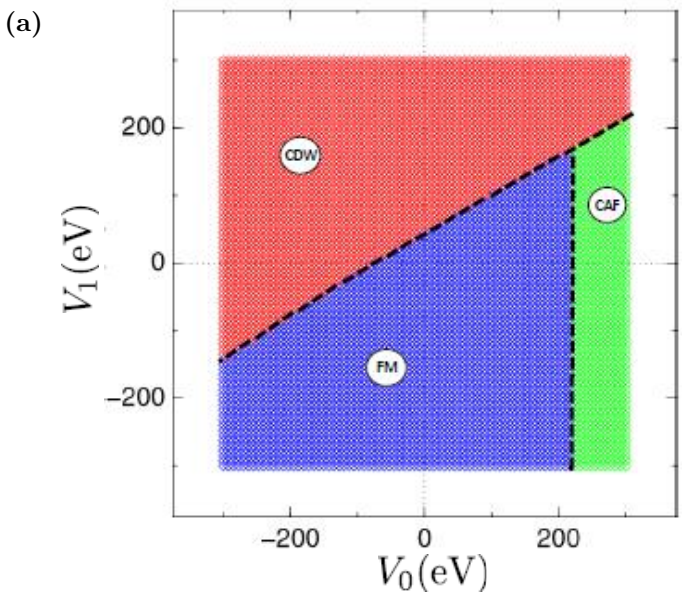

Figure 2.4: Phase diagram for $N = 5$ and $\epsilon_z = 2$.

$\epsilon_z = 2$. Notice the dramatic shift in the location of the CAF-FM boundary, compared to the $N = 3$ diagram (Fig. 2.3b). Other than this shift, the qualitative structure for the two phase diagrams remains roughly the same. In each phase diagram for $N = 7, 9,$ and 11, we found the same qualitative structure. The only quantitative difference is an overall shift in the location of the CAF-FM phase boundary, which occurs at decreasing values of V_0 with increasing N.

To obtain the most accurate picture for this model, the calculation should, ideally, include all accessible LL's in the active window. However, for $B_\perp = 15$T, this would require keeping $N = 5261$ active levels in the diagonalization. We therefore use an extrapolation method to obtain our final result, which we will discuss below.

2.4.2 Stability of the AF/CAF state

The results above suggest that LLM plays an essential role in the appearance of the CAF phase for $N \geq 3$. In what follows, we wish to see in more detail why this happens. For simplicity, we will drop the Zeeman and NN couplings ($\epsilon_z = V_1 = 0$), and focus on the case for $N = 3$. From Fig. 2.3a, we can see that the FM and AF states share the same energy at $V_0 = 0$. In the absence of Zeeman, the AF and FM phases are SU(2) symmetric in the spin space. We therefore choose their density matrix elements to be diagonal in spin and valley indices.

Given a HF state for each of these phases, we can then write the OS energy as

$$\langle \mathcal{H}^{(\mathrm{OS})} \rangle = \frac{V_0 A_c}{4} \int d\boldsymbol{r} \sum_s n_\uparrow(\boldsymbol{r}, s) n_\downarrow(\boldsymbol{r}, s), \tag{2.57}$$

where

$$n_\sigma(\boldsymbol{r}, s) \equiv \sum_\tau \langle \Psi^\dagger_{\sigma,\tau}(\boldsymbol{r}, s) \Psi_{\sigma,\tau}(\boldsymbol{r}, s) \rangle \tag{2.58}$$

is the spin resolved density. We then use eq. (2.7) to expand the continuous field operators in terms of Landau states. Integrating out the spatial dependence so that $n_\sigma(\boldsymbol{r}, s) \to n_\sigma(s)$, the density for

the A sublattice becomes

$$n_\sigma(s=A)=\frac{1}{2(2\pi\ell^2)}\Big[\sum_{n=-1}^{1}\big(2^{\delta_{n,0}}\rho(\sigma,K,n;\sigma,K,n)+(1-\delta_{n,0})\ \rho(\sigma,K',n;\sigma,K',n)\big) \\ +\frac{1}{2}\big(\rho(\sigma,K,-1;\sigma,K,1)-\rho(\sigma,K',-1;\sigma,K',1) \\ +\rho(\sigma,K,1;\sigma,K,-1)-\rho(\sigma,K',1;\sigma,K',-1)\big)\Big], \tag{2.59}$$

where $\rho(\sigma,\tau,n;\sigma',\tau',n')=\langle c^\dagger_{\sigma\tau n}c_{\sigma'\tau'n'}\rangle$ is the density matrix. To obtain $n_\sigma(s=B)$, we interchange $K'\leftrightarrow K$ in $n_\sigma(s=A)$. Note that $\rho(\sigma,\tau,-1;\sigma,\tau,-1)+\rho(\sigma,\tau,1;\sigma,\tau,1)=1$ for both the AF and FM states.

The small, but non-zero, LLM that the program self consistently generates in the density matrix for each of these states yields parameters that appear with a particular sign signature. For matrix elements which are off-diagonal in LL index, these parameters have the form

$$\begin{aligned}
&\rho^{\rm FM}(\uparrow,K,1;\uparrow,K,-1)=a_1 \quad , \quad \rho^{\rm AF}(\uparrow,K,1;\uparrow,K,-1)=a_2;\\
&\rho^{\rm FM}(\downarrow,K,1;\downarrow,K,-1)=-b_1 \quad , \quad \rho^{\rm AF}(\downarrow,K,1;\downarrow,K,-1)=-b_2;\\
&\rho^{\rm FM}(\uparrow,K',1;\uparrow,K',-1)=a_1 \quad , \quad \rho^{\rm AF}(\uparrow,K',1;\uparrow,K',-1)=-b_2;\\
&\rho^{\rm FM}(\downarrow,K',1;\downarrow,K',-1)=-b_1 \ , \quad \rho^{\rm AF}(\downarrow,K',1;\downarrow,K',-1)=a_2,
\end{aligned} \tag{2.60}$$

where $a_1, a_2, b_1,$ and b_2 are positive constants. The magnitudes of these constants are the result of minimizing the energy for each HF state. Given these parameters, the spin resolved densities for the FM state become

$$\begin{aligned}
n^{\rm FM}_\sigma(A)&=\frac{1}{2\pi\ell^2}\Big\{\rho^{\rm FM}(\sigma,K,0;\sigma,K,0)+1\Big\},\\
n^{\rm FM}_\sigma(B)&=\frac{1}{2\pi\ell^2}\Big\{\rho^{\rm FM}(\sigma,K',0;\sigma,K',0)+1\Big\}.
\end{aligned} \tag{2.61}$$

The OS energy is then

$$\langle H^{(\rm OS)}\rangle^{\rm FM}=g\frac{V_0A_c}{2\pi\ell^2}, \tag{2.62}$$

where $g=\frac{L_xL_y}{2\pi\ell^2}$ is the LL degeneracy. For the AF state, the spin resolved densities become

$$\begin{aligned}
n^{\rm AF}_\uparrow(A)&=\frac{1}{2\pi\ell^2}\big[2+(a_2+b_2)\big]\ ,\ n^{\rm AF}_\downarrow(A)=\frac{1}{2\pi\ell^2}\big[1-(a_2+b_2)\big];\\
n^{\rm AF}_\uparrow(B)&=\frac{1}{2\pi\ell^2}\big[1-(a_2+b_2)\big]\ ,\ n^{\rm AF}_\downarrow(B)=\frac{1}{2\pi\ell^2}\big[2+(a_2+b_2)\big],
\end{aligned} \tag{2.63}$$

yielding an OS energy that is then given by

$$\langle \mathcal{H}^{(\mathrm{OS})} \rangle^{\mathrm{AF}} = g\frac{V_0 a_c}{2\pi\ell^2}\left[1 - \frac{a_2 + b_2}{2} - \frac{(a_2 + b_2)^2}{2}\right]. \tag{2.64}$$

In summary of the calculation above, we find that the LLM terms which contribute to the OS energy for the FM state vanish completely. The AF state, however, can take advantage of these contributions in a way that lowers its energy. For this reason, $\langle \mathcal{H}^{(\mathrm{OS})} \rangle^{\mathrm{AF}} < \langle \mathcal{H}^{(\mathrm{OS})} \rangle^{FM}$, when $V_0 > 0$. We note that analogous sign signatures to those in eq. (2.60) persist for larger values of N. The CAF state, like the AF state, can also take advantage of the LLM. However, now, the effects of the Zeeman energy are in direct competition with the gain in energy from the LLM; therefore, if the Zeeman field is big enough, it will overcome the LLM contributions which stabilize the AF state, yielding a spin polarized FM ground state. Hence, OS interactions tend to favor anti-ferromagnetic correlations, which are made possible by LLM.

2.4.3 ϵ_z-V_0 phase diagrams

Since all the phases can be realized by retaining only the OS interaction, phase diagrams were constructed within the ϵ_z-V_0 parameter space, for $V_1 = 0$. Fig. 2.5a shows the phase diagram for $N = 7$. Again, the CAF-FM boundary occurs around nonphysically large values of V_0. Fig. 2.5b shows an evolution of the phase boundaries for various values of the window size. Notice that the boundaries move significantly as N is increased. Due to computational constraints, we were not able to exceed a window size of $N = 301$, which is quite far from the required value of $N = 5261$ at $B_\perp = 15$T. We extrapolated the results for $N \leq 301$, in order to estimate the positions of the physical phase boundaries at $N = 5261$.

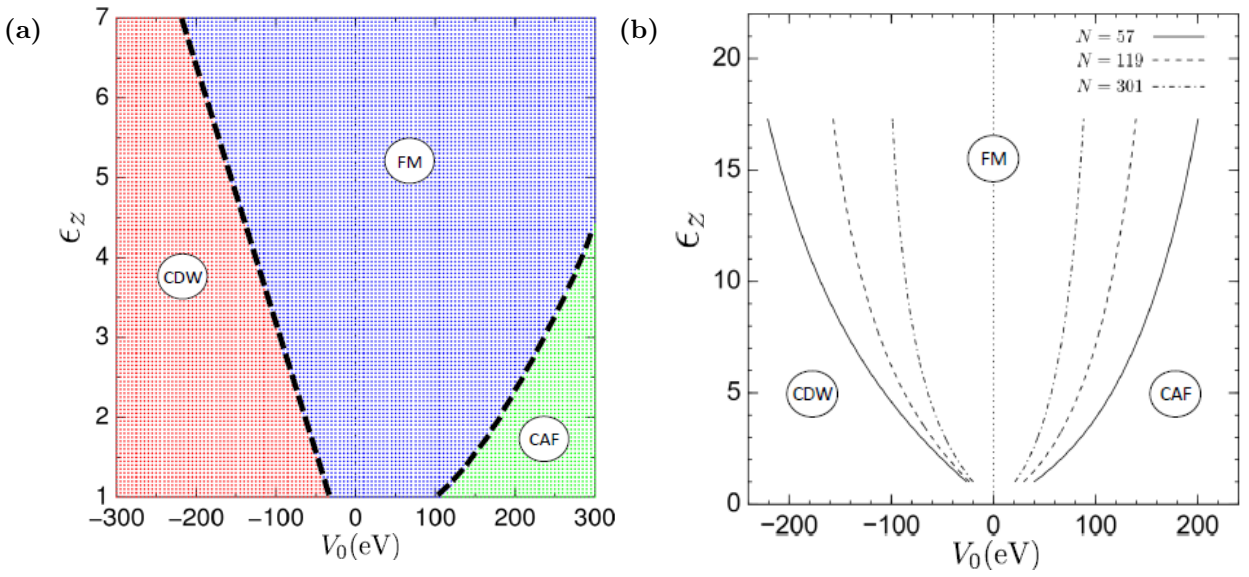

Figure 2.5: (a) Phase diagram for $N = 7$, with $V_1 = 0$. (b) Phase boundaries for $N = 57, 119,$ and 301.

2.4.4 Extrapolation and conclusions

Critical values for V_0 were obtained along the CAF-FM and CDW-FM phase boundaries for a variety of window sizes ($57 \leq N \leq 301$) and Zeeman parameters ($1.0 \leq \epsilon_z \leq 17.3$). The data was fit to a power law, $V_0(N) = aN^{-b}$, for fixed ϵ_z, where a and b are fitting parameters. Fig. 2.6a shows the result of the extrapolation on the phase boundaries. We obtained the error bars by using different sample sizes of data points in the extrapolation.

The range of physical Zeeman fields for this model has a minimum value of $B_T = 15$T, since $\epsilon_z \geq 1$ in a real experiment. Furthermore, Ref. [33] gives an estimate for the OS Hubbard interaction energy of $V_0 \approx 9.3$eV. In the extrapolated phase diagram, the CAF-FM transition, at $V_0 = 9.3$eV, passes right through a physical range of accessible Zeeman fields (Fig. 2.6b). We therefore conclude that the conductance transition as a function of Zeeman field (Fig. 1.8), observed in Ref. [14], is most naturally understood in terms of a CAF-FM transition.

We summarize this section by commenting on the physical insights gained from this window size study. For small window sizes, with the exception of $N = 1$, the correct qualitative behavior of

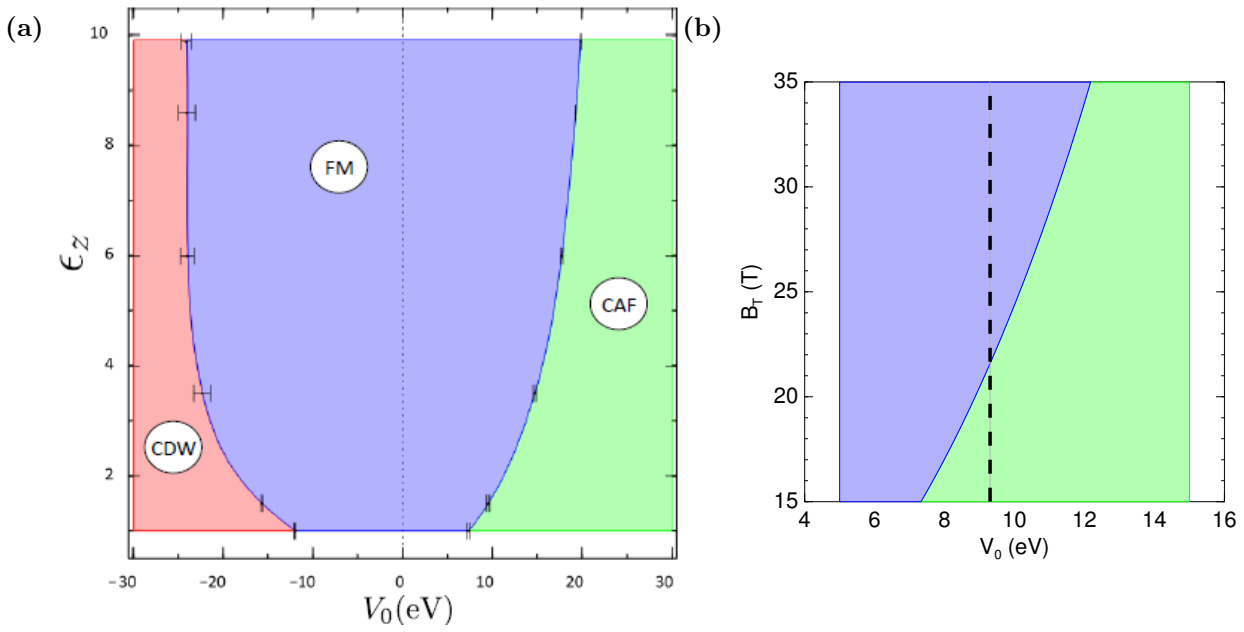

Figure 2.6: (a) Phase diagram after extrapolating the phase boundaries to $N = 5261$. (b) Close up of the CAF-FM phase boundary. The dashed line represents the estimate for the OS Hubbard parameter, $V_0 = 9.3$eV.

the phase boundaries is captured; however, the energy scales at which those phase boundaries occur are greatly overestimated. This point is illustrated by comparing the results for $N = 7$ (Fig. 2.5a) with the results of the extrapolation (Fig. 2.6a). In that comparison, the critical value of V_0 for the CAF-FM transition, at $\epsilon_z = 1$, differs by an order of magnitude. In our study of non-uniform states in Chapters 4 and 5, we will exploit this insight by keeping only three LL's in the calculation.

Chapter 3

Charged Excitations and Lattice Formations

We now discuss the structure of various ground state excitations that one might expect to find near integer filling. In this chapter, to more simply introduce the concepts of these excitations, we will focus mainly on two-level systems where spin is the only discrete degree of freedom. We study the form of single particle excitations in the first part of this chapter. We will then consider lattice formations of these excitations, and briefly outline how information about those lattices is encoded into a density matrix. A Hartree-Fock study of the crystal states will be the focus of Chapters 4 and 5.

3.1 Single particle excitations

The ground state for a conventional 2DEG at $\nu = 1$ is a ferromagnet, which is stabilized through Coulomb exchange interactions and the Pauli principle. In fact, the system will still be spontaneously ferromagnetic even without a Zeeman field present. This is mainly because the scale of the Coulomb interaction is so much larger than the Zeeman interaction. The spin component of the many-body, fermionic wave function is symmetric, when all of the spins are aligned. This forces the spatial component of the wave function to be anti-symmetric, which ultimately lowers the Coulomb energy per particle. Hence, the Coulomb interaction favors configurations that keep the spin locally parallel.

For 2DEGs in a realistic material, the Zeeman energy is typically much smaller than the cyclotron and Coulomb energy scales. For example, in graphene, the gap due to the cyclotron energy between $n = 0$ and $n = 1$ is $\sqrt{2}\hbar v_F/\ell \approx 424\sqrt{B[\mathrm{T}]}$ K, while the Coulomb interaction energy is on the order of $e^2/(4\pi\epsilon_0\epsilon\ell) \approx 218\sqrt{B[\mathrm{T}]}$ K, with $\epsilon = 3$. (For a typical substrate, or even suspended graphene, the dielectric constant ranges roughly from $2 < \epsilon < 5$[33,34].) Both of these energy scales

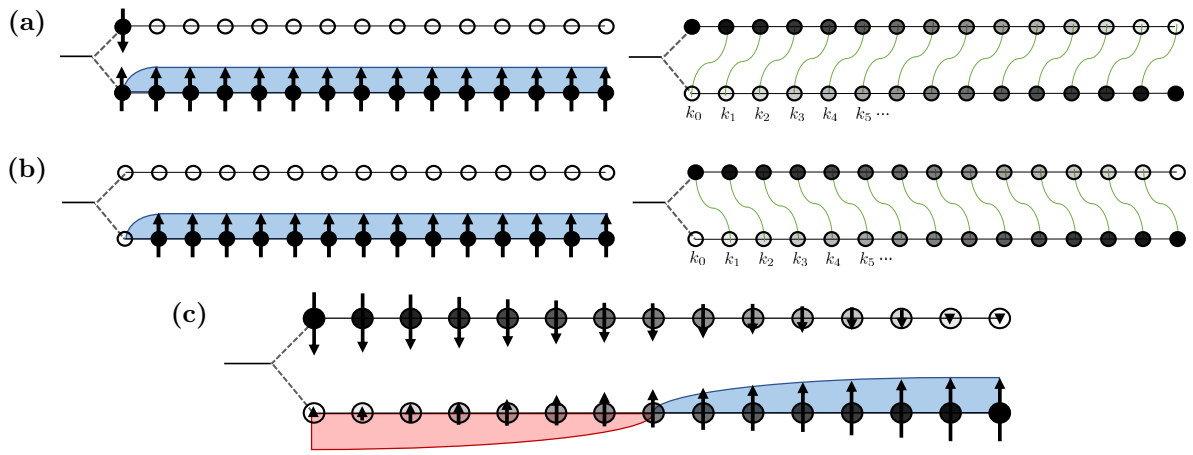

Figure 3.1: Low energy excitations for a two-level spin system in a single LL. (a-left) Qausi-electron. (b-left) Qausi-hole. (c) A spin skyrmion formed by admixing consecutive angular momentum states between spin branches, as shown in (a-right) and (b-right). The blue regions indicate a net spin-up polarization, while the red regions indicate net spin-down. By smearing the charge over many angular momentum states, or equivalently over long distances, the spin gradient is able to vary more smoothly in space.

are much bigger than the gap in Zeeman energy, $2\mu_B B_T \approx 1.34B$[T] K. Near integer filling of a subbranch, we therefore expect low-lying excitations to occur between subbranches belonging to the same LL.

One type of excitation involves adding (Fig. 3.1a-left) an electron to, or removing (Fig. 3.1b-left) an electron from, a filled subbranch, leaving behind a qausi-electron (q-e) or quasi-hole (q-h), respectively. In either case, there is a large energy cost due to exchange interactions. It turns out, that energy cost can be reduced by forming linear combinations of consecutive angular momentum states, k_i, between the lower and upper branch. For example, in the q-e configuration, we form a linear combination between the state at k_0 in the spin up (lower) branch, and the state at k_1 in the spin down (upper) branch, as shown in Fig. 3.1a-right. By choosing the appropriate weights, the majority of the occupation (darker circles) at small angular momentum is in the spin down branch. Gradually, the occupation shifts to the spin up branch at higher angular momentum. The

result for the q-e (q-h) configuration is Fig. 3.1c, which represents a skyrmion (anti-skyrmion). In this case, the charge has been smeared out in such a way that the spin is changing more smoothly as a function of angular momentum, which lessens the cost in exchange energy. There is an added cost, however, in Zeeman energy, due to the additional spins that are now pointing in the opposite direction to the ground state. The discussion above can be extended to real space, since angular momentum and physical position are tied together within a given LL.

When the Zeeman energy is not too large, it has been shown[35], for conventional 2DEGs, that the lowest energy single particle excitations are skyrmions. Skyrmions are a type of topological soliton that host "spin textures", and have smoothly varying spin gradients around their cores. Remarkably, skyrmions carry physical charge, which we will discuss in more detail below.

3.1.1 Skyrmions

Skyrmions can be realized within the O(3) nonlinear sigma model, which is commonly used to study QH systems such as chiral magnets and magnetic thin films. The Lagrangian for this model has the form

$$\mathcal{L} = -\frac{J_s}{2}\big(\partial^\mu \phi\big)\big(\partial_\mu \phi\big), \tag{3.1}$$

where J_s is the spin stiffness, $\phi = (\phi_1, \phi_2, \phi_3)$ is a 3-component vector field, and repeated indices are summed over. The fields are written in 2D so that $\phi_i = \phi_i(x, y)$. To ensure that the energy in this model remains finite, we require

$$\lim_{r\to\infty} \phi(\boldsymbol{r}) = \phi^\infty, \tag{3.2}$$

a constant. Furthermore, the fields are subject to the normalization condition $\phi^2 = \phi_i\phi_i = 1$. Given these constraints, we may choose the boundary conditions on the individual field components so that

$$\lim_{r\to\infty} \phi_1(\boldsymbol{r}) = 0, \ \lim_{r\to\infty} \phi_2(\boldsymbol{r}) = 0, \ \lim_{r\to\infty} \phi_3(\boldsymbol{r}) = 1. \tag{3.3}$$

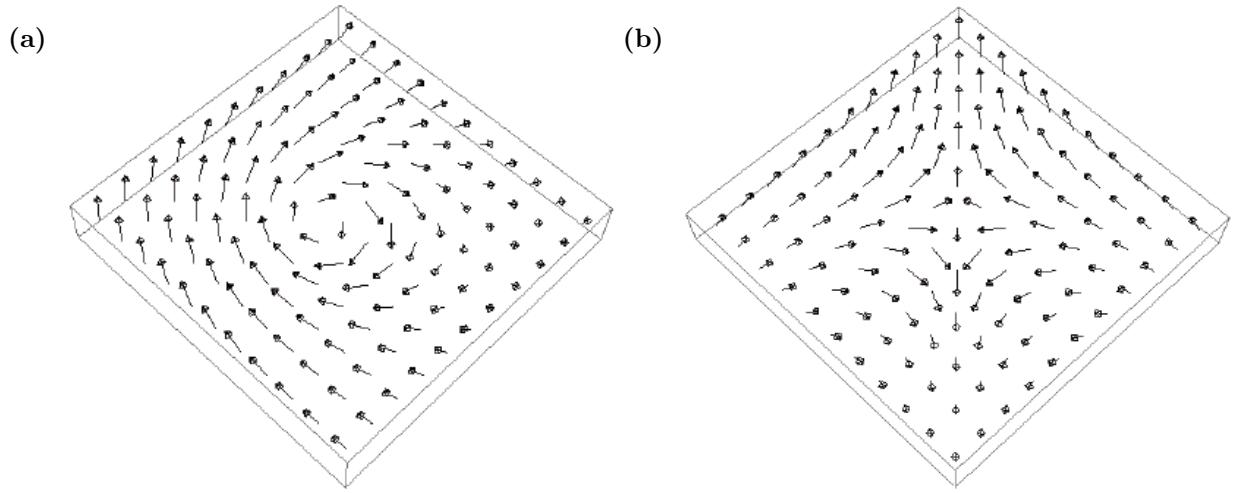

Figure 3.2: Textures for the (a) skyrmion and (b) anti-skyrmion. Both images reproduced from Ref. [37].

By minimizing the gradient energy,

$$E = \frac{J_s}{2} \int d^2r \, \left(\nabla\phi\right)^2, \tag{3.4}$$

the vector fields which describe a skyrmion may be expressed [36], in polar coordinates, as

$$\begin{aligned} \phi_1(\boldsymbol{r}) &= \frac{2\lambda r}{\lambda^2 + r^2} \cos(\theta - \varphi), \\ \phi_2(\boldsymbol{r}) &= \pm \frac{2\lambda r}{\lambda^2 + r^2} \sin(\theta - \varphi), \\ \phi_3(\boldsymbol{r}) &= \frac{r^2 - \lambda^2}{\lambda^2 + r^2}. \end{aligned} \tag{3.5}$$

In eq. (3.5), λ is a constant that determines the size scale of the skyrmion, and φ is a constant that controls the (in-plane) orientation of ϕ_1 and ϕ_2. The '+' on the right hand side of ϕ_2 corresponds to a skyrmion (Fig. 3.2a), while the '$-$' corresponds to an anti-skyrmion (Fig. 3.2b). The arrows point straight down at the center in each figure, and gradually rotate, pointing up at infinite radius. At intermediate distances, the in-plane components of the skyrmion have a vortex-like winding; that is, if we move in a circle, say clockwise from above, around the core, then the in-plane components of the arrows also rotate clockwise. If we move around the core in the same sense, and the in-plane components rotate counter-clockwise, then we have an anti-skyrmion with an anti-vortex structure.

For either case, the in-plane components rotate by a full 2π around any closed path circling the origin. The energy for each of these objects is independent of φ, yielding a U(1) symmetry with respect to global in-plane rotations.

For the case of magnetic skyrmions in 2DEGs, the field, ϕ, is replaced by an order parameter that describes the local magnetization, $\boldsymbol{m}(r,\theta)$, with $\phi_1 \to m_x$, $\phi_2 \to m_y$, and $\phi_3 \to m_z$. We can now describe the boundary conditions in eq. (3.3) as a requirement on the magnetization, far from the core of the skyrmion ($r >> \lambda$), to point in the direction of the ground state. In the core, when $r \to 0$, we have $\boldsymbol{m} = (0, 0, -1)$. Furthermore, skyrmions covers all directions of magnetization on the Bloch sphere exactly once. This property is independent of the direction of the ground state.

Another interesting feature of the QH skyrmion is that it carries electric charge, which is induced by the addition of an electron, or hole, on top of the filled, spin-polarized subbranch. As charge moves through the magnetization field, it acquires an additional Berry phase (in addition to the one induced by the Zeeman coupling). The curl of the corresponding Berry connection yields a flux that is proportional to the topological density, or Pontryagin density, which is written as

$$\rho_{\text{top}}(\boldsymbol{r}) \equiv \frac{1}{8\pi}\epsilon^{\alpha\beta}\boldsymbol{m}\cdot\big(\partial_\alpha\boldsymbol{m}\times\partial_\beta\boldsymbol{m}\big). \tag{3.6}$$

Following Ref. [38], this flux is also proportional to local changes in the charge density, $\delta\rho(\boldsymbol{r})$, due to the rotation of the spin within a filled subbranch of a single LL. This leads to the identity,

$$\delta\rho(\boldsymbol{r}) = \nu e\rho_{\text{top}}(\boldsymbol{r}). \tag{3.7}$$

This remarkable result implies that the charge density couples directly to the local spin orientation. Furthermore, the topological charge,

$$Q_{\text{top}} = \frac{1}{8\pi}\int d^2r\ \epsilon^{\alpha\beta}\boldsymbol{m}\cdot\big(\partial_\alpha\boldsymbol{m}\times\partial_\beta\boldsymbol{m}\big) = \pm 1, \tag{3.8}$$

for the fields given in eq. (3.5), where $Q_{\text{top}} = -1$ $(+1)$ corresponds to the skyrmion (anti-skrymion). Thus, at $\nu = 1$, we conclude that the skyrmion (anti-skyrmion) carries the same charge as the electron (positron).

In a physical system, the reason why skyrmions are stable is related to the energy cost for spin gradients. The spin texture makes those gradients as small as possible, so that the spin is changing slowly in space. In an adiabatic way, this allows local spins to remain, approximately, parallel. Within the core, there are many spins that point in the minority direction relative to the Zeeman field. A balance is then struck between the cost in Zeeman energy for flipping spins in the "wrong" direction, and the amount of Coulomb energy saved by having a slow rotation of the spin. That balance determines the size of the skyrmion. Thus, when the Zeeman is small, it pays to form a spin texture. If the Zeeman is big enough, the texture will collapse, and the system will become a q-e or q-h type excitation.

3.1.2 Merons

Another type of topological object which is relevant to our study is the meron. The distinguishing feature for a meron is that its magnetization only covers half of the Bloch sphere. One way to capture this feature is to let

$$\lim_{r\to\infty} m_z(\boldsymbol{r}) = 0, \ \lim_{r\to\infty} \left[m_x(\boldsymbol{r}) + i m_y(\boldsymbol{r})\right] = e^{\pm i\varphi}, \tag{3.9}$$

where φ represents the azimuthal angle of the position vector, $\boldsymbol{r}$. In this representation, the magnetization is confined to the x-y plane at large radial distances, forming a vortex ($e^{i\varphi}$) or anti-vortex ($e^{-i\varphi}$) that persists arbitrarily far from the core of the meron. To avoid a singularity in the gradient energy, the magnetization at the center of the core ($r \to 0$) must be $\boldsymbol{m} = (0, 0, \pm 1)$; approaching the core center, the magnetization rotates smoothly, up or down, out of the x-y plane. This requirement, together with the two types of vorticities, yield four flavors of merons, shown in Fig. 3.3a.

The full magnetization field can be modeled as

$$\boldsymbol{m}(\boldsymbol{r}) = \left\{\sqrt{1-(m_z(r))^2}\cos\varphi, \pm\sqrt{1-(m_z(r))^2}\sin\varphi, m_z(r)\right\}, \tag{3.10}$$

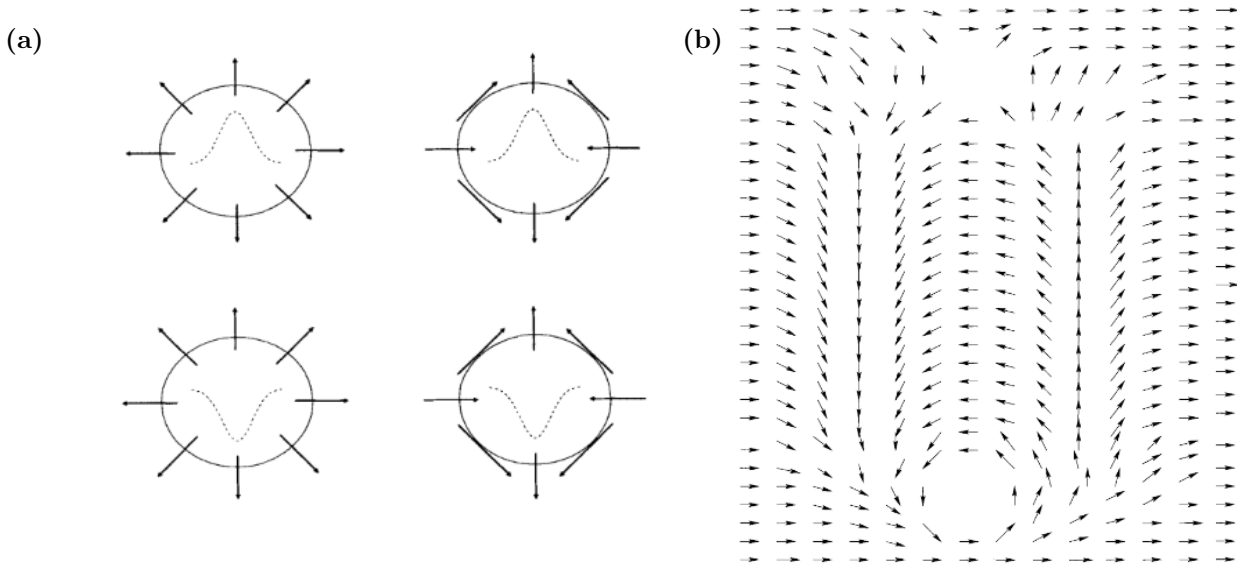

Figure 3.3: (a) Four flavors of merons. They are distinguished by their vorticity and polarity at the core center. The topological charge is the same for the merons shown in the top left and bottom right, and for the merons shown in top right and bottom left. (b) Bound meron pair with opposite vorticities, topologically equivalent to a skyrmion/anti-skyrmion. In this representation, the natural direction for the ground state would point to the right. Both images reproduced from Ref. [39].

which yields a topological charge of

$$Q_{\text{top}} = \frac{1}{2}\big[m_z(\infty) - m_z(0)\big]n_v, \tag{3.11}$$

where the winding number, n_v, is +1 (-1) for a vortex (anti-vortex). With four types of merons, the only two unique outcomes for the topological charge are such that $Q_{\text{top}} = \pm 1/2$. Hence, merons carry a physical charge of $\pm\nu e/2$, and the sign is determined by the vorticity and the polarity in the core, $m_z(0)$, of the meron.

The energy of a meron, by itself, diverges logarithmically with the area of the system, because the winding persists arbitrarily far from the core. However, a bound pair of merons with opposite vorticities can combine to yield a net magnetization that is uniform at large radial distances. Moreover, if each of these bound merons carry the same charge, so that one of them covers the south pole while the other covers the north pole of the Bloch sphere, then the meron pair is topologically equivalent to a skyrmion; the magnetization covers the entire Bloch sphere exactly once (Fig. 3.3b). We conclude by noting that, as long as the Zeeman energy is not too big, vortex/anti-vortex pairs of merons can crystallize to form a lattice, when the vortices are dense enough. These lattices will be discussed in more detail in the next section.

3.2 Lattice structures

3.2.1 The Skyrme lattice

Near odd integer filling in a two-level system, a finite density of quasiparticles can crystallize into a lattice. For the conventional 2DEG near $\nu = 1$, the ground state is a lattice of spin textured skyrmions[40], based on Hartree-Fock (HF) calculations. When the skyrmions are very dilute, the ground state is a triangular Skyrme lattice, consistent with the Madelung energy for point particles on a 2D lattice. In fact, for charged particles in a classical 2D lattice with a $1/r$ Coulomb interaction, a triangular configuration yields the lowest electrostatic energy[41]. When the textures

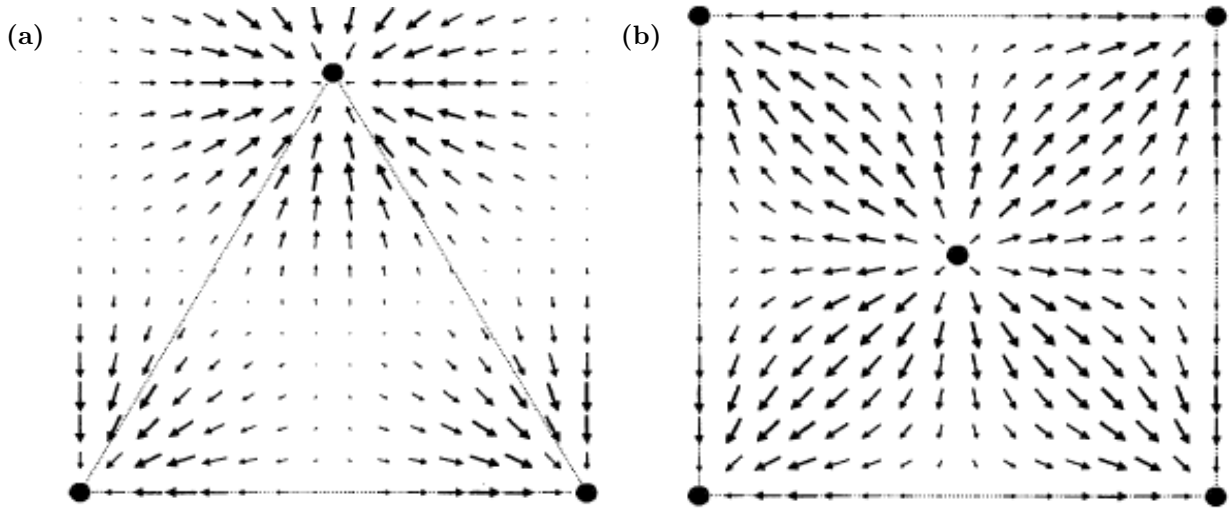

Figure 3.4: Unit cell structures for the (a) triangular and (b) square lattice of skyrmions obtained from HF calculations of conventional 2DEG materials. The arrows represent the x-y components of the spin density, and their lengths are proportional to the local magnitude of the in-plane spin. Both crystal states were obtained using the same Zeeman coupling and filling factor ($\nu = 1.1$). Both images reproduced from Ref. [40].

begin to overlap, which can occur for a relatively dilute density of skyrmions, the ground state may choose a square lattice.

The in-plane (x-y) components of the spin density in the unit cell of the HF state, corresponding to a triangular and square lattice of skyrmions, are shown in Figs. 3.4a and 3.4b. In these pictures, the Zeeman field is taken to point along an axis with $m_z = 1$. The center of the cores are marked by filled circles. Notice that the triangular lattice has the same azimuthal orientation, $m_\perp$, between cores of neighboring skyrmions; they all have orientations pointing inward. The magnitude of $m_\perp$ is small for regions of m_z near +1 (outside of the cores) and for regions of m_z near -1 (close to the core center).

For the square lattice, there are two skyrmions. One is located at the center, and the other is represented on the corners of the unit cell. Moreover, the azimuthal orientation is reversed between neighboring skyrmions. In either lattice, the textures between neighbors begin to overlap

as the density of skyrmions increases. This forces the spin, along a line between two neighboring skyrmions in the triangular lattice, to rotate by π over increasingly smaller distances, which leads to a high cost in exchange energy. The square lattice does not have this limitation. Hence, the square lattice is the preferred ground state for sufficient deviations away from $\nu = 1$. The instability of the triangular lattice is an example of geometric frustration. The square lattice avoids this frustration by arranging nearest neighbors in a bipartite lattice with a two point basis. In this way, there is almost no rotation of in-plane spin components in regions between nearest neighbors.

The global U(1) rotational symmetry here is broken, however local U(1) rotations about the Zeeman axis do not change the energy. Therefore, this representation is just one of many degenerate HF states. Notice, for the square lattice, that the in-plane spin components respect the symmetry of the lattice; as we rotate in space, at fixed radius, around the origin by some angle, the in-plane spin also rotates by the same magnitude of that angle. We will use this crucial observation in our HF study of textured states in graphene in the following chapters. We conclude this section by noting that, at sufficiently large densities, the spin textures will collapse, forming a Wigner crystal of q-e's or q-h's.

3.2.2 The meron lattice

So far, this chapter has focused on two-level spin systems for conventional 2DEGs. In the context of graphene, the valleys also play the role of a two-level, pseudospin index. Thus, if we assume the real spin is fully polarized, it is possible to form pseudospin textures by taking linear combinations of angular momentum states between pseudospin branches. This has been shown in Ref. [42]. In that study, the model Hamiltonian included an SU(4) symmetric Coulomb interaction and a Zeeman coupling. Since only the spin degree of freedom is sensitive to the latter, it is possible to realize a meron crystal, hosting a pseudospin texture, in such a system; the pseudospin textured skyrmions become very large, since they are unaffected by the Zeeman energy, and they

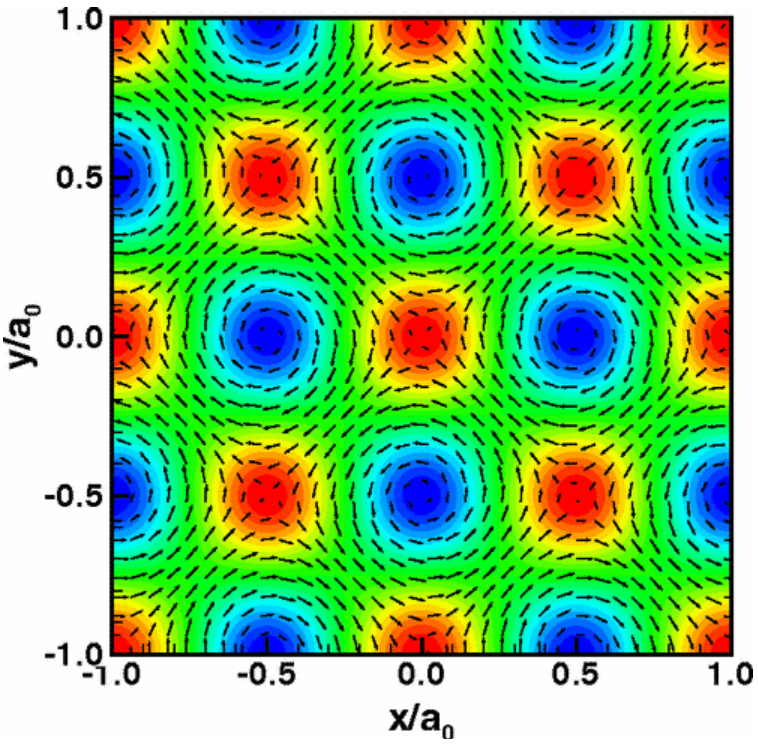

Figure 3.5: Unit cell for a square lattice of pseudospin textured merons at filling factor $\nu = -1.2$ in graphene. This configuration is continuously deformable to a unit cell containing two (pseudospin textured) skyrmions. Since the Zeeman coupling does not affect these textures, the cores of the skyrmions become very large, and they overlap. It is energetically favorable for the skyrmions to then crystallize into their constituent merons. by Image reproduced from Ref. [42].

strongly overlap with one another. The energy is then minimized by crystallizing the skyrmions into their constituent merons. The result is a square formation of meron pairs with vortex/anti-vortex structures, and opposite pseudospin polarities at their core centers. The resulting merons all have the same physical charge.

Indeed, a HF ground state resembling a square lattice of merons was found for a range of filling factors near odd integer filling of the $n = 0$ LL. The lattice is shown in Fig. 3.5, where the pseudospin components are plotted for the unit cell, with lattice spacing a_0. The arrows represent the in-plane components of the pseudospin, (P_x, P_y), while the contours represent P_z. Green regions represent areas where $P_z = 0$. There are four merons (all with charge $-e/2$) per unit cell, two of

which have $P_z = -0.5$ (red) at the core centers, while the other two have $P_z = 0.5$ (blue). This type of lattice is continuously deformable to a lattice of skyrmions

3.3 Lattice representations in a HF state

In this section, we will outline how the lattices, described above, are represented in a HF state. For states hosting a texture, these representations hinge on the fact that the in-plane spins respect the symmetry of the 2D lattice. The section is concluded with a discussion about the particular problem we wish to solve in the remaining chapters of this thesis.

The model Hamiltonian, eq. (2.9) and eq. (2.36), presented in Chapter 2, is written in terms of a momentum basis in k. The connection between that basis and the lattice representation is given by the operator,

$$\rho_{\alpha\alpha'}(\boldsymbol{q}) = \frac{1}{g}\sum_{k,k'} e^{-iq_x(k+k')\ell^2/2}\delta_{k,k'+q_y}c^\dagger_{\alpha k}c_{\alpha' k'}, \tag{3.12}$$

where $\alpha \to \{\sigma, \tau, n\}$ represents a set of labels corresponding to the spin, valley, and LL indices, respectively. The inverse of this operator is easily shown to be

$$c^\dagger_{\alpha k}c_{\alpha' k'} = \sum_{\boldsymbol{q}} e^{iq_x(k+k')\ell^2/2}\delta_{k',k-q_y}\rho_{\alpha\alpha'}(\boldsymbol{q}). \tag{3.13}$$

Note that, for $k = k'$,

$$\sum_k c^\dagger_{\alpha k}c_{\alpha' k} = g\rho_{\alpha\alpha'}(\boldsymbol{q} = 0), \tag{3.14}$$

so that the expectation value,

$$\big\langle \rho_{\alpha\alpha}(\boldsymbol{q} = 0)\big\rangle = \nu_\alpha, \tag{3.15}$$

gives the filling factor, $\nu_{\sigma\tau n}$, in the n$^{\text{th}}$ LL for a given spin and valley index.

Furthermore, the expectation value, $\langle\rho(\boldsymbol{q})\rangle$, for a crystal HF state is non-zero only when $\boldsymbol{q} = \boldsymbol{G}$, where $\boldsymbol{G} = (G_x, G_y)$ is a reciprocal lattice vector (RLV). RLV's are specified in terms of the lattice spacing, a_0, with $G \propto 2\pi/a_0$, which further depends on the filling factor. Hence, the lattice spacing

depends on the density of quasiparticles,

$$n_{\rm qp} = \frac{N_{\rm uc}}{A_{\rm uc}}, \tag{3.16}$$

where $N_{\rm uc}$ is the number of quasiparticles per unit cell, and $A_{\rm uc}$ is the area of the unit cell. For crystal states with a texture (i.e., a lattice of skyrmions), $N_{\rm uc} = 2$. We can write the filling of quasiparticles as

$$\nu_{\rm qp} = 2\pi n_{\rm qp} \ell^2. \tag{3.17}$$

Note that, depending on the filling factor, we can also have a hole lattice of quasiparticles. The particular form of eq. (3.17) will be specified in the next chapter.

The rest of this thesis will focus on a study of HF states in graphene near $\nu = 0$. In what follows, each LL will have four components ($\uparrow\downarrow \otimes KK'$). We will choose $\left\langle \rho_{\alpha\alpha'}(\boldsymbol{G}) \right\rangle$ as the order parameter for the study. It is reasonable to believe that ground states supporting textures will be present, but the way in which textures manifest themselves in the discrete degrees of freedom is unclear.

Chapter 4

Non-uniform States Near $\nu = 0$

In this chapter, we further develop the model, presented in Chapter II, to accommodate the types states we expect to find at noninteger filling factors. We provide an overview with some simplifications to the model, and outline the assumptions we use in the calculation. Following that, the non-interacting Hamiltonian and HF interactions, eq. (2.9) and eq. (2.37), are expanded in the RLV basis using the operators, eq. (3.13), introduced in the last chapter. We then use an equation of motion approach, with single particle Matsubara Green's functions. In this way, the order parameter, $\langle \rho(\boldsymbol{G}) \rangle$, is calculated through an iterative diagonalization scheme, similar to the one used in Chapter 2. We conclude the chapter with a discussion on how the numerical HF calculation is carried out.

4.1 Overview

In this study, we are looking for classes of crystal states that fall into two categories: 1) states with textures and 2) states without textures. Our goal will be to construct a phase diagram within the space of the Zeeman parameter and the filling factor. Filling factors near $\nu = 0$ are considered, and we expect hole crystals ($\nu < 0$) to be particle-hole conjugates of electron crystals ($\nu > 0$). We choose to focus on filling factors with $\nu < 0$. It is important to add that we only consider square lattices of hole crystals in this thesis. The square lattice qualitatively captures the kinds of states we expect to find near $\nu = 0$, based on our results at $\nu = 0$, and they allow the crystal to host spin textures as described above. The other reason why we only consider these types of lattices is due to the already large parameter space inherent to the problem; it would be very difficult to explore an exhaustive study involving several types of lattices (e.g., rectangular and triangular). The implications of this restriction will be described in the results of our study (Chapter 5).

For a square lattice, RLV's have the form

$$\boldsymbol{G} = \frac{2\pi}{a_0}\big(m_x\hat{\mathbf{x}} + m_y\hat{\mathbf{y}}\big), \tag{4.1}$$

where m_x and m_y are integers. From eq. (3.17), the lattice spacing between hole-like quasiparticles is determined by

$$a_0 = \sqrt{\frac{2\pi N_{\rm uc}}{|\nu|}}\ \ell \propto \frac{1}{\sqrt{B}}, \tag{4.2}$$

where $|\nu|$ is the same as the quasiparticle filling, $\nu_{\rm qp}$, near $\nu = 0$. Notice that the lattice spacing for the quasiparticle crystal depends on the magnetic length, $\ell = 25.6\text{nm}/\sqrt{B[\text{T}]}$. For typical parameters in this model, we are always in the regime $a_0 >> \tilde{a} = 0.24$ nm, the lattice spacing of graphene.

To initialize a HF state with a texture, we need to build the symmetry of the (real-space) lattice into the off-diagonal components of the discrete indices in the order parameter. For example, to initialize a spin texture on the square lattice, we assume the order parameter has the form

$$\big\langle \rho_{\uparrow\downarrow}(\boldsymbol{G})\big\rangle = e^{i\theta_{\boldsymbol{G}}}, \tag{4.3}$$

where $\theta_{\boldsymbol{G}}$ is the angle between $\boldsymbol{G}$ and the x-axis. Notice that $\pi/2$ rotations of $\theta_{\boldsymbol{G}}$ also rotate the in-plane spin by $\pi/2$. Furthermore, we only need to initialize the first shell of RLV's, which belong to the set of RLV's with the smallest non-zero magnitude. In this way, the spin texture is initially built into the components of $\boldsymbol{G}$ with $(m_x, m_y) = (1,0),\ (0,1),\ (-1,0),$ and $(0,-1)$. Specifying this symmetry condition, in addition to the filling factor, is enough for the HF algorithm to self consistently generate a HF state with a spin texture.

Another type of state that we expect to find in this analysis are Wigner crystals, which are essentially a lattice of quasi-electrons or quasi-holes. Such a state is approximately modeled by a Gaussian in $|\boldsymbol{G}| = G$. For example, to initialize a Wigner crystal of spin polarized quasiparticles, we take

$$\big\langle \rho_{\uparrow\uparrow}(\boldsymbol{G})\big\rangle \propto e^{-G^2\ell^2/4} \text{ and } \big\langle \rho_{\downarrow\downarrow}(\boldsymbol{G})\big\rangle = 0. \tag{4.4}$$

These types of lattices do not host spin textures, so there is only one quasiparticle per unit cell ($N_{\rm uc} = 1$). However, we want to allow for the possibility of textured HF states, whenever they are energetically favorable. Therefore, in the program, we always take $N_{\rm uc} = 2$, so that there are more RLV's than are needed to describe a Wigner crystal. An order parameter that represents a Wigner crystal thus has the form, $\langle \rho(\boldsymbol{G}) \rangle \propto \left[1 \pm e^{i\pi(m_x+m_y)}\right]$.

In Chapter 2, we saw that all of the phases (CDW, CAF, and FM) appearing in the phase diagram could be obtained by just keeping the OS interaction. Therefore, we do not include NN interactions in our model of crystal states; there's no reason to believe that, by including NN interactions, we will obtain states, with or without texture, that we would not obtain with only the OS interaction. Another result from Chapter 2 is that all of the phases at $\nu = 0$ are qualitatively captured by keeping only three LL's ($n = -1,\ 0,$ and 1) in the calculation. To keep the parameter space as small as possible, we will only keep three LL's in our study of crystal states. This simplification will qualitatively capture the nature of the phase diagram, at the cost of having to use an unphysically large OS interaction parameter (V_0). Another observation from Chapter 2 was that the Kekulé (KD) phase never appeared in the phase diagram. This is the only state, of the four possible ground states at $\nu = 0$, that admix different pseudospin indices in the density matrix; that is $\langle c^\dagger_\tau c_{\tau'} \rangle_{\rm KD} \neq 0$ for $\tau \neq \tau'$. Therefore, in the numerical calculation, we take the order parameter to be diagonal in pseudospin.

4.2 Model Hamiltonian

We begin with the non-interacting Hamiltonian in eq. (2.9), which can now be written as

$$\mathcal{H}_0 = g \sum_{n,\sigma,\tau} \left[\mathrm{sgn}(n) \frac{\hbar v_F}{\ell} \sqrt{2\,|n|} - \frac{\sigma g^* \mu_B}{2} B_T \right] \rho_{\sigma\tau n, \sigma\tau n}(\boldsymbol{q} = 0), \tag{4.5}$$

where we have used eq. (3.13) to rewrite the $c^\dagger c$ operator in terms of the ρ operator. The contribution from the Dirac sea will be added later. For now, all summations over LL indices will include all accessible LL's. Recall that states in the filled sea are inert and uniform, so their contribution

will appear with the factor $\rho(\boldsymbol{q}=0)$ in the non-interacting Hamiltonian.

Recall the HF interactions, given by eq. (2.37),

$$\begin{aligned}\mathcal{H}^{(\mathrm{i})}_{\mathrm{HF}} &= \frac{1}{S}\sum_{\boldsymbol{\xi},\boldsymbol{k}} f^{(\mathrm{i})}(\boldsymbol{\tau})\delta_{\sigma_1,\sigma_4}\delta_{\sigma_2,\sigma_3}\sum_{\boldsymbol{p}}\mathcal{M}^{(\mathrm{i})}(\boldsymbol{n},\boldsymbol{\tau},\boldsymbol{p})\delta_{k_1,k_4-p_y}\delta_{k_2,k_3+p_y}e^{ip_x(k_1+k_4-k_2-k_3)\ell^2/2} \\ &\quad\times\left[\,\langle c^\dagger_{\xi_1k_1}c_{\xi_4k_4}\rangle\, c^\dagger_{\xi_2k_2}c_{\xi_3k_3} - \langle c^\dagger_{\xi_1k_1}c_{\xi_3k_3}\rangle\, c^\dagger_{\xi_2k_2}c_{\xi_4k_4}\right] \\ &\equiv \mathcal{H}^{(\mathrm{i})}_{\mathrm{D}} - \mathcal{H}^{(\mathrm{i})}_{\mathrm{X}},\end{aligned} \tag{4.6}$$

where $\xi_j \to (\sigma_j,\tau_j,n_j)$ is a composite index, and $\mathrm{i} = \mathrm{C},\mathrm{OS}$, for each interaction. We will write the elements of the interactions explicitly in terms of the state indices, so there is no confusion. Inserting eq. (3.13) into eq. (4.6), the exchange component, after summing out the $\boldsymbol{k}$ indices, becomes

$$\mathcal{H}^{(\mathrm{i})}_{\mathrm{X}} = \frac{g}{S}\sum_{\boldsymbol{\xi}} f^{(\mathrm{i})}(\boldsymbol{\tau})\delta_{\sigma_1,\sigma_4}\delta_{\sigma_2,\sigma_3}\sum_{\boldsymbol{q},\boldsymbol{p}} e^{i\boldsymbol{p}\times\boldsymbol{q}\ell^2}\mathcal{M}^{(\mathrm{i})}(\boldsymbol{n},\boldsymbol{\tau},\boldsymbol{p})\left\langle\rho_{\xi_1\xi_3}(\boldsymbol{q})\right\rangle\rho_{\xi_2\xi_4}(-\boldsymbol{q}), \tag{4.7}$$

where $\boldsymbol{p}\times\boldsymbol{q} \equiv p_xq_y - p_yq_x$, and $g = S/2\pi\ell^2$ is the LL degeneracy. Similarly, the direct component becomes

$$\mathcal{H}^{(\mathrm{i})}_{\mathrm{D}} = \frac{g^2}{S}\sum_{\boldsymbol{\xi}} f^{(\mathrm{i})}(\boldsymbol{\tau})\delta_{\sigma_1,\sigma_4}\delta_{\sigma_2,\sigma_3}\sum_{\boldsymbol{q}} \mathcal{M}^{(\mathrm{i})}(\boldsymbol{n},\boldsymbol{\tau},\boldsymbol{q})\left\langle\rho_{\xi_1\xi_4}(-\boldsymbol{q})\right\rangle\rho_{\xi_2\xi_3}(\boldsymbol{q}). \tag{4.8}$$

The $\boldsymbol{q}=0$ (uniform), divergent term for the Hartree Coulomb interaction is again cancelled by the positive background; it is implied that the sum in $\mathcal{H}^{(\mathrm{C})}_{\mathrm{D}}$ only includes terms with $\boldsymbol{q}\neq 0$.

Similar to the functions given in eq. (2.46) and eq. (2.47), we define

$$\mathcal{T}^{(\mathrm{i})}_{\mathrm{X}}(\boldsymbol{n},\boldsymbol{\tau},\boldsymbol{q}) \equiv \int \frac{d\boldsymbol{p}}{(2\pi)^2} e^{i\boldsymbol{p}\times\boldsymbol{q}\ell^2}\mathcal{M}^{(\mathrm{i})}(\boldsymbol{n},\boldsymbol{\tau},\boldsymbol{p}) \tag{4.9}$$

and

$$\mathcal{T}^{(\mathrm{i})}_{\mathrm{D}}(\boldsymbol{n},\boldsymbol{\tau},\boldsymbol{q}) \equiv \frac{1}{2\pi\ell^2}\mathcal{M}^{(\mathrm{i})}(\boldsymbol{n},\boldsymbol{\tau},\boldsymbol{q}), \tag{4.10}$$

where the sum over $\boldsymbol{p}$ has been converted to an integral ($\frac{1}{S}\sum_{\boldsymbol{p}} \to \int \frac{d\boldsymbol{p}}{(2\pi)^2}$). The form of the integral in eq. (4.9) is worked out in Appendix C. Interchanging indices ($3 \leftrightarrow 4$), and shifting the sum over

$\boldsymbol{q} \to -\boldsymbol{q}$, in the direct component, the HF interactions can now be written as

$$\begin{aligned}
\mathcal{H}^{(\mathrm{i})}_{\mathrm{HF}} &= \mathcal{H}^{(\mathrm{i})}_{\mathrm{D}} - \mathcal{H}^{(\mathrm{i})}_{\mathrm{X}} \\
&= g \sum_{\boldsymbol{q},\boldsymbol{\xi}} \Big\{ f^{(\mathrm{i})}(\boldsymbol{\tau}_{34}) \delta_{\sigma_1,\sigma_3} \delta_{\sigma_2,\sigma_4} \mathcal{T}^{(\mathrm{i})}_{\mathrm{D}}(\boldsymbol{n}_{34}, \boldsymbol{\tau}_{34}, -\boldsymbol{q}) \\
&\qquad\qquad - f^{(\mathrm{i})}(\boldsymbol{\tau}) \delta_{\sigma_1,\sigma_4} \delta_{\sigma_2,\sigma_3} \mathcal{T}^{(\mathrm{i})}_{\mathrm{X}}(\boldsymbol{n}, \boldsymbol{\tau}, \boldsymbol{q}) \Big\} \left\langle \rho_{\xi_1\xi_3}(\boldsymbol{q}) \right\rangle \rho_{\xi_2\xi_4}(-\boldsymbol{q}) \\
&\equiv g \sum_{\boldsymbol{q}} \sum_{\xi_2,\xi_4} H^{(\mathrm{i})}_{\xi_2,\xi_4}(\boldsymbol{q}) \rho_{\xi_2\xi_4}(-\boldsymbol{q}),
\end{aligned} \tag{4.11}$$

which defines the interacting HF matrix (IHFM), $H^{(\mathrm{i})}_{\sigma_2\tau_2 n_2,\sigma_4\tau_4 n_4}(\boldsymbol{q})$, expressed as a function of $\boldsymbol{q}$ for the OS and C interactions. In eq. (4.11), the label, $\boldsymbol{\tau}_{34}$ and $\boldsymbol{n}_{34}$, stands for a reordering of the constituent labels. For example, $\boldsymbol{\tau}_{34} = (\tau_1, \tau_2, \tau_4, \tau_3)$.

It is helpful to find a relation between $H^{(\mathrm{i})}_{\xi,\xi'}(\boldsymbol{q})$ and $H^{(\mathrm{i})}_{\xi k,\xi' k'}$, the IHFM written in terms of k, k'. Using eq. (3.12) to expand the $\rho(-\boldsymbol{q})$ operator in the last line of eq. (4.11), we obtain

$$\mathcal{H}^{(\mathrm{i})}_{\mathrm{HF}} = \sum_{\xi_2,\xi_4} \sum_{k_2,k_4} \Big[\sum_{\boldsymbol{q}} H^{(\mathrm{i})}_{\xi_2,\xi_4}(\boldsymbol{q}) e^{iq_x(k_2+k_4)\ell^2/2} \delta_{k_2,k_4-q_y} \Big] c^\dagger_{\xi_2 k_2} c_{\xi_4 k_4}. \tag{4.12}$$

The form of the equation above is very similar to that of eq. (4.6). To see this, we interchange indices ($3 \leftrightarrow 4$) in the direct term of eq. (4.6), and define a new IHFM, $H^{(\mathrm{i})}_{\xi_2 k_2,\xi_4 k_4}$, so that

$$\mathcal{H}^{(\mathrm{i})}_{\mathrm{HF}} \equiv \sum_{\xi_2,\xi_4} \sum_{k_2,k_4} H^{(\mathrm{i})}_{\xi_2 k_2,\xi_4 k_4} c^\dagger_{\xi_2 k_2} c_{\xi_4 k_4}. \tag{4.13}$$

Comparing the expression above to the one in eq. (4.12), we see that

$$H^{(\mathrm{i})}_{\xi_2 k_2,\xi_4 k_4} = \sum_{\boldsymbol{q}} H^{(\mathrm{i})}_{\xi_2,\xi_4}(\boldsymbol{q}) e^{iq_x(k_2+k_4)\ell^2/2} \delta_{k_2,k_4-q_y}. \tag{4.14}$$

We now include the contribution to the Dirac sea of LL's, following exactly the same procedure presented in Chapter 2; a LL index with $n < -n_w$ belongs to the Dirac sea, and is prevented from admixing between LL's with $-n_w \le n \le n_w$. The contribution is added to the non-interacting Hamiltonian, which now reads as

$$\mathcal{H}_0 = g \sum_{\sigma,\tau} \sum_{n,n'=-n_w}^{n_w} h^0_{\sigma\tau n,\sigma\tau n'} \rho_{\sigma\tau n,\sigma\tau n'}(\boldsymbol{q}=0), \tag{4.15}$$

where

$$h^0_{\sigma\tau n,\sigma\tau,n'} \equiv \mathrm{sgn}(n)\frac{\hbar v_F}{\ell}\sqrt{2|n|}\delta_{n,n'} - \frac{\sigma g^* \mu_B}{2} B_T \delta_{n,n'} - \mathcal{T}^{(\mathrm{C})}_{\mathrm{sea}}(n,n'), \tag{4.16}$$

and $\mathcal{T}^{(\mathrm{C})}_{\mathrm{sea}}(n,n')$ is given by eq. (2.53). All LL summations in eq. (4.11) now include indices for which $-n_w \leq n_j \leq n_w$.

As described at the end of Chapter 3, $\langle \rho(\boldsymbol{q}) \rangle$ is non-zero only when $\boldsymbol{q} = \boldsymbol{G}$, a reciprocal lattice vector. Therefore, we will replace $\boldsymbol{q}$ with $\boldsymbol{G}$ in what follows. In Chapter 2, the numerical method that we used to find a HF state involved diagonalizing the full HF matrix, which included contributions from non-interacting and interacting terms. The IHFM is now written as a function of $\boldsymbol{G}$, and it is not obvious how one would carry out a similar diagonalization scheme. In the next section, we will introduce a new matrix that can be iteratively diagonalized. The eigenvectors of this matrix are shown to be directly connected to the order parameter, $\langle \rho(\boldsymbol{G}) \rangle$.

4.3 Matsubara Green's functions

In this section, we introduce the Matsubara (single particle) Green's functions,

$$\mathcal{G}(\alpha,\beta;\bar{\tau}) \equiv -\left\langle T_{\bar{\tau}} c_\alpha(\bar{\tau}) c^\dagger_\beta(0) \right\rangle, \tag{4.17}$$

where α, β are an arbitrary set of state labels that we will specify shortly, $\bar{\tau}$ has units of time, and $T_{\bar{\tau}}$ is the time ordering operator. Notice that

$$\mathcal{G}(\alpha,\beta;\bar{\tau}=0^-) = \langle c^\dagger_\beta c_\alpha \rangle \tag{4.18}$$

gives the density matrix, with a reordering of the state labels. Furthermore, the Fourier transform of the Green's functions, between time and frequency domains, is given by

$$\mathcal{G}(\alpha,\beta;\bar{\tau}) \equiv \frac{1}{\beta_T}\sum_m e^{-i\omega_m \bar{\tau}} \mathcal{G}(\alpha,\beta;i\omega_m), \tag{4.19}$$

where ω_m is a fermionic Matsubara frequency, and $\beta_T = \frac{1}{k_B T}$, with temperature, T, and Boltzmann constant, k_B.

To apply the Green's functions to our model, we use a Heisenberg equation of motion,

$$\frac{\partial}{\partial\bar{\tau}}(...) = \big[\mathcal{H} - \mu N, (...)\big], \tag{4.20}$$

where μ is the chemical potential, $N = c^\dagger c$ is the number operator, and we have set $\hbar = 1$. The following method was originally developed in Ref. [43] to study collective modes of 2D Wigner crystals in conventional 2DEG systems. The method has also been applied in graphene to study Wigner crystals and textured states near various integer fillings[42,44,45]. However, these models only retained the SU(4) symmetric Coulomb interaction.

The formalism is developed in Appendix D, where we work out the main result needed for our study:

$$\big(i\omega_m + \mu\big)\mathcal{G}(\alpha,\beta;i\omega_m) = \delta_{\alpha,\beta} + \sum_\gamma \Big[h^0_{\alpha,\gamma} + H_{\alpha,\gamma}\Big]\mathcal{G}(\gamma,\beta;i\omega_m), \tag{4.21}$$

again, where α,β,γ are an arbitrary set of state labels. In eq. (4.21), $H_{\alpha,\gamma} = \sum_{\rm i} H^{(\rm i)}_{\alpha,\gamma}$, with $\rm i = C, OS$, is the component of the HF matrix arising from interactions, and $h^0_{\alpha,\gamma}$ is the non-interacting component. We now insert the set of state labels, $\alpha \to \{\xi, k\},\ \beta \to \{\xi', k'\},\ \gamma \to \{\xi'', k''\}$, keeping $\xi \to (\sigma,\tau,n)$ as a composite index, in the original basis of the Hamiltonian. The equation of motion now becomes

$$(i\omega_m + \mu)\mathcal{G}_{\xi\xi'}(k,k';i\omega_m) = \delta_{\xi,\xi'}\delta_{k,k'} + \sum_{\xi''}\Big[h^0_{\xi,\xi''} + \sum_{k''}\sum_{\rm i} H^{(\rm i)}_{\xi k,\xi'' k''}\Big]\mathcal{G}_{\xi''\xi'}(k'',k';i\omega_m), \tag{4.22}$$

where we have used the fact that $h^0_{\xi k,\xi'' k''} = \delta_{k,k''}h^0_{\xi,\xi''}$.

To write the Fourier transform of the Green's functions in reciprocal lattice space, we note, using eq. (3.12) and eq. (4.18),

$$\big\langle \rho_{\xi\xi'}(\boldsymbol{G})\big\rangle = \frac{1}{g}\sum_{k,k'} e^{-iG_x(k+k')\ell^2/2}\delta_{k,k'+G_y}\mathcal{G}_{\xi'\xi}(k',k;\bar{\tau}=0^-), \tag{4.23}$$

so that

$$\mathcal{G}_{\xi\xi'}(\boldsymbol{G};\bar{\tau}=0^-) = \frac{1}{g}\sum_{k,k'} e^{-iG_x(k+k')\ell^2/2}\delta_{k,k'-G_y}\mathcal{G}_{\xi\xi'}(k,k';\bar{\tau}=0^-), \tag{4.24}$$

with

$$\mathcal{G}_{\xi\xi'}(\boldsymbol{G};\bar{\tau}=0^{-})=\left\langle \rho_{\xi'\xi}(\boldsymbol{G})\right\rangle . \tag{4.25}$$

The Green's function, written in frequency space, transforms in the same way as eq. (4.24). Multiplying eq. (4.22) by $\frac{1}{g}e^{-iG_x(k+k')\ell^2/2}\delta_{k,k'-G_y}$, and summing over k,k', then gives

$$\begin{aligned}(i\omega_m+\mu)\mathcal{G}_{\xi\xi'}(\boldsymbol{G};i\omega_m)&=\delta_{\xi,\xi'}\delta_{\boldsymbol{G},0}+\sum_{\xi''}h^0_{\xi,\xi''}\mathcal{G}_{\xi''\xi'}(\boldsymbol{G};i\omega_m)\\&\quad+\frac{1}{g}\sum_{\mathrm{i}}\sum_{\xi'',k''}\sum_{k,k'}e^{-iG_x(k+k')\ell^2/2}\delta_{k,k'-G_y}H^{(\mathrm{i})}_{\xi k,\xi'' k''}\mathcal{G}_{\xi''\xi'}(k'',k';i\omega_m).\end{aligned} \tag{4.26}$$

We now insert eq. (4.14) into the last line of eq. (4.26), to rewrite the IHFM in terms of RLV's. After evaluating the straight forward phase factor algebra, the equation of motion becomes

$$\begin{aligned}(i\omega_m+\mu)\mathcal{G}_{\xi\xi'}(\boldsymbol{G};i\omega_m)&=\delta_{\xi,\xi'}\delta_{\boldsymbol{G},0}+\sum_{\xi''}h^0_{\xi,\xi''}\mathcal{G}_{\xi''\xi'}(\boldsymbol{G};i\omega_m)\\&\quad+\sum_{\mathrm{i}}\sum_{\xi'',\boldsymbol{G}''}e^{i\boldsymbol{G}''\times\boldsymbol{G}\ell^2/2}H^{(\mathrm{i})}_{\xi,\xi''}(\boldsymbol{G}-\boldsymbol{G}'')\mathcal{G}_{\xi''\xi'}(\boldsymbol{G}'';i\omega_m)\\&=\delta_{\xi,\xi'}\delta_{\boldsymbol{G},0}+\sum_{\xi''\boldsymbol{G}''}U\big[\xi,\boldsymbol{G}\mid\xi'',\boldsymbol{G}''\big]\mathcal{G}_{\xi''\xi'}(\boldsymbol{G}'';i\omega_m),\end{aligned} \tag{4.27}$$

where we have defined the Hermitian matrix,

$$U\big[\xi,\boldsymbol{G}\mid\xi'',\boldsymbol{G}''\big]\equiv h^0_{\xi,\xi''}\delta_{\boldsymbol{G},\boldsymbol{G}''}+e^{i\boldsymbol{G}''\times\boldsymbol{G}\ell^2/2}\sum_{\mathrm{i}}H^{(\mathrm{i})}_{\xi,\xi''}(\boldsymbol{G}-\boldsymbol{G}''). \tag{4.28}$$

Our next task will be to connect the U matrix to the order parameter. In terms of the eigenvectors, V^j, which diagonalize U, and the corresponding eigenvalues, ϵ^j, we can write

$$\sum_{\xi'',\boldsymbol{G}''}U\big[\xi,\boldsymbol{G}\mid\xi'',\boldsymbol{G}''\big]V^j(\xi'',\boldsymbol{G}'')=\epsilon^jV^j(\xi,\boldsymbol{G}). \tag{4.29}$$

The Green's functions are expanded in the basis of these eigenvectors,

$$\mathcal{G}_{\xi''\xi'}(\boldsymbol{G}'';i\omega_m)=\sum_j A_j(\xi')V^j(\xi'',\mathbf{G}''), \tag{4.30}$$

for each RLV, which is then inserted into eq. (4.27) to give

$$\delta_{\xi,\xi'}\delta_{\boldsymbol{G},0}=(i\omega_m+\mu)\sum_j A_j(\xi')V^j(\xi,\boldsymbol{G})-\sum_j A_j(\xi')\epsilon^jV^j(\xi,\boldsymbol{G}). \tag{4.31}$$

We obtain the coefficients for the Green's function expansion by multiplying eq. (4.31) by $(V^{j'})^*(\xi, \boldsymbol{G})$, and summing over ξ and $\boldsymbol{G}$. The coefficients are

$$A_j(\xi') = \frac{(V^j)^*(\xi', \boldsymbol{G}=0)}{i\omega_m + \mu - \epsilon^j}, \tag{4.32}$$

so that the Green's function is written as

$$\mathcal{G}_{\xi''\xi'}(\boldsymbol{G}''; i\omega_m) = \sum_j \frac{(V^j)^*(\xi', \boldsymbol{G}=0)V^j(\xi'', \boldsymbol{G}'')}{i\omega_m + \mu - \epsilon^j}. \tag{4.33}$$

Noting eq. (4.19), we now take $\bar{\tau} \to 0^-$. Then,

$$\begin{aligned}\mathcal{G}_{\xi'\xi}(\boldsymbol{G}''; \bar{\tau}=0^-) &= \sum_j \left\{ \frac{1}{\beta_T} \lim_{\bar{\tau}\to 0^-} \sum_n \frac{e^{-i\omega_n \bar{\tau}}}{i\omega_n + \mu - \epsilon^j} \right\} (V^j)^*(\xi, \boldsymbol{G}=0)V^j(\xi', \boldsymbol{G}'') \\ &= \sum_j n_F(\epsilon^j - \mu)(V^j)^*(\xi, \boldsymbol{G}=0)V^j(\xi', \boldsymbol{G}''),\end{aligned} \tag{4.34}$$

where the frequency sum has yielded the Fermi distribution function, n_F. At zero temperature, the Fermi distribution becomes a step function. Recalling that $\langle \rho_{\xi\xi'}(\boldsymbol{G}) \rangle = \mathcal{G}_{\xi'\xi}(\boldsymbol{G}; \bar{\tau}=0^-)$, the order parameter is finally written as

$$\left\langle \rho_{\xi\xi'}(\boldsymbol{G}) \right\rangle = \sum_{j \le j_{\max}} (V^j)^*(\xi, \mathbf{G}=0)V^j(\xi', \mathbf{G}), \tag{4.35}$$

where $j_{\max}$ is the largest j which satisfies $\epsilon^j < \mu$; that is, we only sum over eigenvectors belonging to states with eigenenergies below the chemical potential. Thus, the order parameter is constructed from the eigenvectors of the U matrix.

4.4 Numerical HF loop

To obtain a HF state, we follow a similar procedure to the one outlined in Chapter 2. The main difference is that we must now diagonalize the U matrix, given by eq. (4.28), instead of the HF matrix. The HF loop begins by initializing the order parameter, which is then used to construct the U matrix. The eigenvectors are then used to construct the next iteration of the order parameter, from eq. (4.35), and the process is repeated until the order parameter is converged. The error on

the i^{th} iteration is determined in a similar way as before, and is given by

$$\text{err}(i) \equiv \frac{\sum_{\xi,\xi'} \sum_{\boldsymbol{G}} \left| \langle \rho^{i}_{\xi\xi'}(\boldsymbol{G}) \rangle - \langle \rho^{i-1}_{\xi\xi'}(\boldsymbol{G}) \rangle \right|}{\sum_{\xi,\xi'} \sum_{\boldsymbol{G}} \left| \langle \rho^{i}_{\xi\xi'}(\boldsymbol{G}) \rangle^{*} \langle \rho^{i}_{\xi\xi'}(\boldsymbol{G}) \rangle \right|^{1/2}}. \tag{4.36}$$

A state is converged when err $\leq \chi$, the tolerance value, which we take to be in the range $10^{-10} \leq \chi \leq 10^{-8}$.

In principle, there are an infinite number of RLV's in this model. However, the interactions appearing in the previous sections come with a product of form factors, given by eq. (2.26), which are proportional to a Gaussian, $F(\boldsymbol{G}) \propto e^{-G^2\ell^2/4}$. The Gaussians are highly suppressed for large magnitudes of RLV's, so we introduce a cutoff, G_{max}, and keep only the RLV's with

$$G = \frac{2\pi}{a_0}\left(m_x^2 + m_y^2\right) \leq G_{\text{max}} \equiv \frac{2\pi}{a_0} s_{\text{max}}^2 \tag{4.37}$$

in the numerical calculation. There is some trial and error involved in determining the cutoff value. It is typically chosen to give the best convergence for the order parameter; if too few RLV's are used, the error never reaches the tolerance value. Furthermore, we find that states hosting spin textures need more RLV's to reach convergence, while Wigner crystals need much fewer. For a typical trial run involving spin textures, a value of $s_{\text{max}} = 8.5$, corresponding to $N_G = 225$ RLV's, is found to give well converged solutions. Keeping three LL's, and including spin and pseudospin, the size of the U matrix in this case is 2700×2700. However, since we do not include terms in the order parameter which are off-diagonal in the pseudospin index, the problem is reduced to diagonalizing two matrices, each of size 1350×1350. For the parameters chosen in this model, we are always in the regime where the RLV cutoff is much smaller than the magnitude of the Dirac point, $G_{\text{max}} << \mathcal{K} = \frac{4\pi}{3\tilde{a}} = 17.45$ nm^{-1}, which justifies the use of the continuum approximation.

It is helpful to introduce a new measure for the filling factor. The trace of the order parameter, with $\langle \rho_{\sigma\tau n,\sigma\tau n}(\boldsymbol{G}=0) \rangle \equiv \langle \rho_{\sigma\tau n}(\boldsymbol{G}=0) \rangle$, gives the value

$$\sum_{\sigma,\tau,n} \langle \rho_{\sigma\tau n}(\boldsymbol{G}=0) \rangle = 4n_w + \bar{\nu}, \tag{4.38}$$

where $2n_w + 1$ is the number of active LL's (in this case $n_w = 1$), and $\bar{\nu} > 0$ is the filling factor for the partially filled $n = 0$ LL, in the non-interacting limit. The total filling is then given by $\nu = \bar{\nu} - 2 < 0$. For example, a value of $\bar{\nu} = 1.8$ corresponds to total filling factor, $\nu = -0.2$ of holes. When the order parameter is constructed from the eigenvectors of the U matrix, the value of $j_{\max}$, in eq. (4.35), is determined so that the trace of the order parameter yields the correct electronic filling factor, $\nu_e = 4n_w + \bar{\nu}$. To obtain the right filling factor, it is often necessary to interpolate between the eigenvector $V^{j_{\max}}$, and its adjacent eigenvector, $V^{j_{\max}-1}$ or $V^{j_{\max}+1}$. It is also possible to construct the order parameter using the Fermi distribution function at very small, non-zero temperatures. In that case, the chemical potential is chosen so that the trace of the order parameter yields the correct filling.

To better visualize a HF state, we construct the expectation value of the real space density, which is defined in terms of the (continuous) field operators. With $s = A, B$ for each sublattice, the density is given by

$$\langle n(\boldsymbol{r}, s)\rangle = \sum_{\sigma\tau} \left\langle \Psi^\dagger_{\sigma\tau}(\boldsymbol{r}, s)\Psi_{\sigma\tau}(\boldsymbol{r}, s)\right\rangle . \tag{4.39}$$

Summing over the pseudospin, and using eq. (2.7) and eq. (3.13) to expand the field operators in terms of LL's and RLV's, the density becomes

$$\langle n(\boldsymbol{r}, s)\rangle = \frac{1}{2\pi\ell^2}\sum_{\boldsymbol{G}} \big[n_K(\boldsymbol{G}, s) + n_{K'}(\boldsymbol{G}, s)\big] e^{i\boldsymbol{G}\cdot\boldsymbol{r}}. \tag{4.40}$$

The term in the square brackets above yields

$$\begin{aligned} n_K(\boldsymbol{G}, A) + n_{K'}(\boldsymbol{G}, A) = \sum_{\sigma,n,n'} \frac{\sqrt{2}^{\delta_{n,0}+\delta_{n',0}}}{2} \big[\mathrm{sgn}(nn') F_{|n|-1,\,|n'|-1}(-\boldsymbol{G})\, \langle \rho_{\sigma K n,\sigma K n'}(\boldsymbol{G})\rangle \\ + F_{|n|,\,|n'|}(-\boldsymbol{G})\, \langle \rho_{\sigma K' n,\sigma K' n'}(\boldsymbol{G})\rangle \big] \end{aligned} \tag{4.41}$$

for the A sublattice, where $F_{n,n'}(\boldsymbol{G})$ is the form factor given by eq. (2.26). For the B sublattice, $n_K(\boldsymbol{G}, B) + n_{K'}(\boldsymbol{G}, B)$ is obtained by interchanging $K \leftrightarrow K'$ on the right hand side of eq. (4.41). It is also useful to calculate the local spin density, which is given by

$$\left\langle S^i(\boldsymbol{r}, s)\right\rangle = \frac{1}{2}\sum_{\sigma,\sigma',\tau} \left\langle \Psi^\dagger_{\sigma\tau}(\boldsymbol{r}, s)\big(\sigma^i\big)_{\sigma\sigma'}\Psi_{\sigma'\tau}(\boldsymbol{r}, s)\right\rangle , \tag{4.42}$$

where σ_i is a Pauli matrix and $i = x, y, z$. In terms of LL's and RLV's, the spin density on the A sublattice is

$$\Big\langle S^i(\boldsymbol{r}, A)\Big\rangle = \frac{1}{4\pi\ell^2}\sum_{\boldsymbol{G}}\big[S^i_K(\boldsymbol{G}, A) + S^i_{K'}(\boldsymbol{G}, A)\big]e^{i\boldsymbol{G}\cdot\boldsymbol{r}}, \tag{4.43}$$

where

$$\begin{aligned} S^i_K(\boldsymbol{G}, A) + S^i_{K'}(\boldsymbol{G}, A) = \sum_{\sigma,\sigma',n}\frac{2^{\delta_{n,0}}}{2}\big(\sigma^i\big)_{\sigma\sigma'}\big[\mathrm{sgn}(n)F_{|n|-1,\,|n|-1}(-\boldsymbol{G})\,\langle\rho_{\sigma Kn,\sigma' Kn}(\boldsymbol{G})\rangle \\ +F_{n,n}(-\boldsymbol{G})\,\langle\rho_{\sigma K'n,\sigma' K'n}(\boldsymbol{G})\rangle\,\big], \end{aligned} \tag{4.44}$$

is written as a trace over the LL index. In a similar way as before, $S^i_K(\boldsymbol{G}, B) + S^i_{K'}(\boldsymbol{G}, B)$ is obtained by interchanging $K \leftrightarrow K'$ on the right hand side of eq. (4.44).

One of the motivations for this study is to determine the nature of the CAF-FM transition, when the system is doped away from integer filling. Our hope is to find spin textured HF ground states that host some kind of canting structure. For this to happen, one might expect formations of spin textures for each valley pseudospin, when the density of quasiparticles is dilute enough. Our results of the numerical HF calculation are presented in the next chapter.

Chapter 5

Numerical Results at Noninteger Filling

In this chapter, we present the numerical results of the HF study at noninteger filling. The phase diagram is shown in Fig. 5.1, plotted as a function of total filling factor, ν, and Zeeman parameter, ε_z, which relates the total field and the perpendicular field ($B_{\rm T} = \varepsilon_z B$). Throughout this study, unless stated otherwise, the perpendicular field, OS interaction parameter, and the number of RLV's for each HF trial run are all fixed at values $B = 2$T, $V_0 = 500$ eV, and $N_G = 225$, respectively. Recall that, for $V_0 > 0$, the only two ground state phases at $\nu = 0$ included the CAF and the FM; the CDW appeared only for $V_0 < 0$. As discussed in the previous chapter, we include only $N = 3$ active LL's in the main calculation, and omit the NN interaction, so that we only have on-site (OS) and Coulomb (C) interactions.

5.1 Phase diagram

A number of phases are obtained throughout the parameter space. We will first describe the phases without any spin texture. These phases consist of the FM, CAF, and the collinear-ferrimagnet (co-Fi), a new phase that did not appear at integer filling. Each phase is characterized by the orientation of its (global) spin majority, which is represented by the arrows in Fig. 5.1 for each valley pseudospin index, K and K'. If we take the Zeeman direction to be in $\hat{\mathbf{z}}$, the CAF always has in-plane (x-y) components that are anti-parallel with respect to the two valleys. Furthermore, we define θ_K ($\theta_{K'}$) to be the angle between the net spin in the K (K') valley and the polar axis of the Bloch sphere. For the CAF phase at integer filling, we always had $\theta_K = \theta_{K'}$, with $0 < \theta_K \leq \pi/2$. In that case, $\theta_K = \theta_{K'} = \pi/2$ corresponds to the situation when the Zeeman field was absent, and $\theta_K = \theta_{K'} = 0$ yielded the FM. At noninteger filling, the CAF phase is now described by polar angles with $0 < \theta_{K'} < \pi$ and $0 < \theta_K \leq \bar{\theta}_K$, where $\bar{\theta}_K$ is a function of the

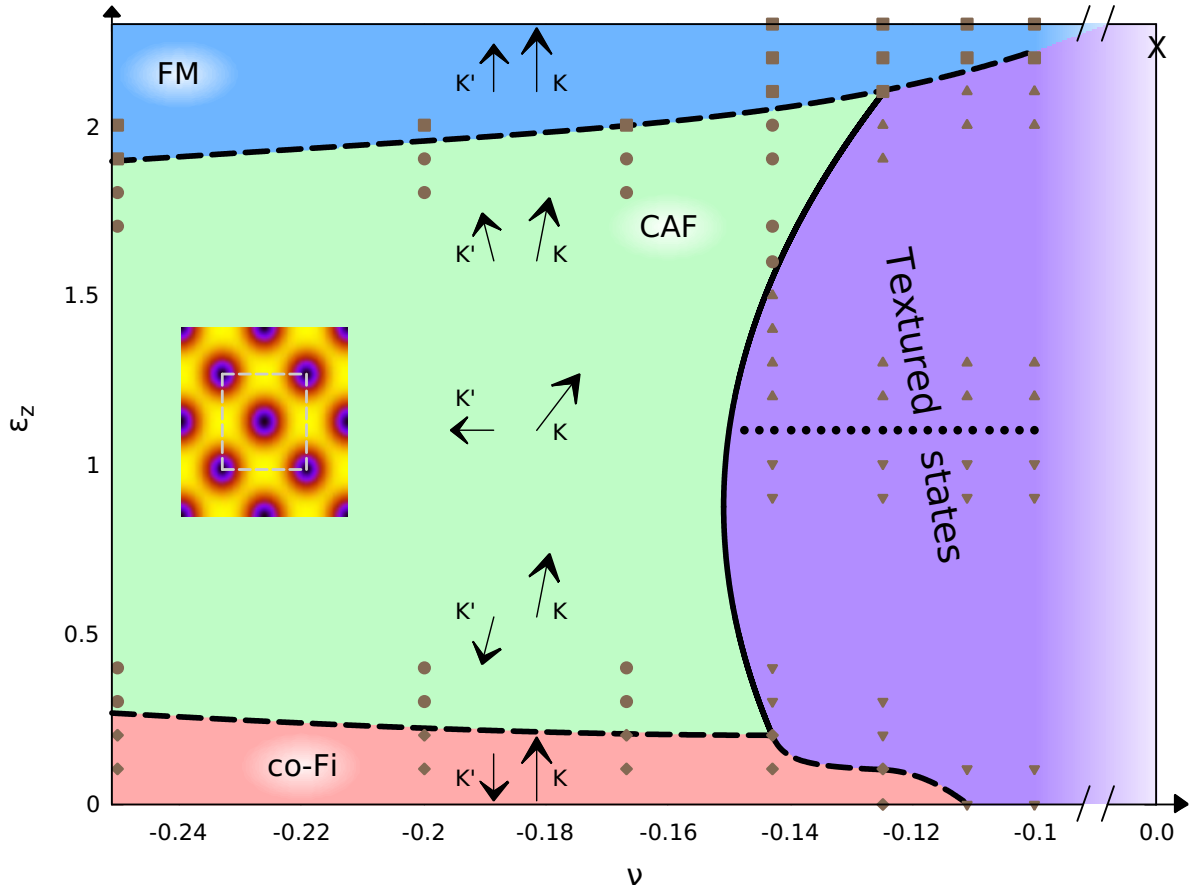

Figure 5.1: Phase diagram at noninteger filling. Solid (dashed) black lines represent first (second) order transitions. The brown symbols represent the more relevant points, around the phase boundaries, where the numerical calculation was carried out. The FM (square), CAF (brown circle), and co-Fi (diamond) phases do not host spin textures, and their spin structures are represented by the arrows, for each valley. We find spin textured skyrmions with ferromagnetic cores (upside down triangles) and anti-ferromagnetic cores (right-side up triangles), with a crossover phase resembling a meron lattice (black circles) between the two phases of skyrmions. The **X** on the vertical axis at $\nu = 0$ represents the CAF-FM transition point ($\varepsilon_z = 2.23$) at noninteger filling.

total filling factor. Furthermore, we now have $\theta_K \neq \theta_{K'}$, for the CAF. The co-Fi is obtained when $\theta_{K'} = \pi$ and $\theta_K = 0$.

One of the main results of this study is that the hole charge only forms quasiparticle crystals in a single valley, which we will refer to as the partially filled valley. The other valley is completely filled and spatially uniform, yielding HF states that are, overall, partially valley polarized. We will refer to this configuration as the "closed shell" configuration. There is also no preference as to which valley forms the quasiparticle crystal. This result is still present in the textured phases, which we will discuss in more detail shortly.

For the phases with no texture, the quasiparticles form a Wigner crystal (WC) of quasi-holes in a single valley. The inset of Fig. 5.1 illustrates such a WC on a square lattice, where the yellow contours represent ground state regions with $\nu = 0$, and the darker regions show the locations of the quasi-holes. The perimeter of the unit cell is outlined by the dashed line. Furthermore, since these states have no texture, the spin direction is uniform throughout the entire unit cell. Therefore, the unit cell drawn here is actually twice as big as it needs to be.

The magnitudes of the net spin for each valley are not equal; the length of the spin vector for the filled valley is longer than that of the spin vector for the partially filled valley. Fig. 5.2 shows a plot of the spin components as a function of the Zeeman parameter for each valley at total filling factor $\nu = -0.2$. In this case, the electronic filling for the K' (partially filled) valley is $\sum_{\sigma,n} \langle \rho_{\sigma K' n, \sigma K' n} \rangle = 2.8$, while $\sum_{\sigma,n} \langle \rho_{\sigma K n, \sigma K n} \rangle = 3$. As discussed in the next section, the Coulomb interaction, particularly the intra-valley exchange contribution, is what drives the stability of the closed shell configuration.

At smaller hole densities, we obtain spin textured HF states. These states have a square lattice of (hole) skyrmions in a single valley, while the other valley is completely filled, spatially uniform, and always spin polarized in the direction of the Zeeman field. For small values of the Zeeman parameter ($\varepsilon_z < 1.1$, below the black circles in Fig. 5.1), the skyrmions have ferromagnetic cores;

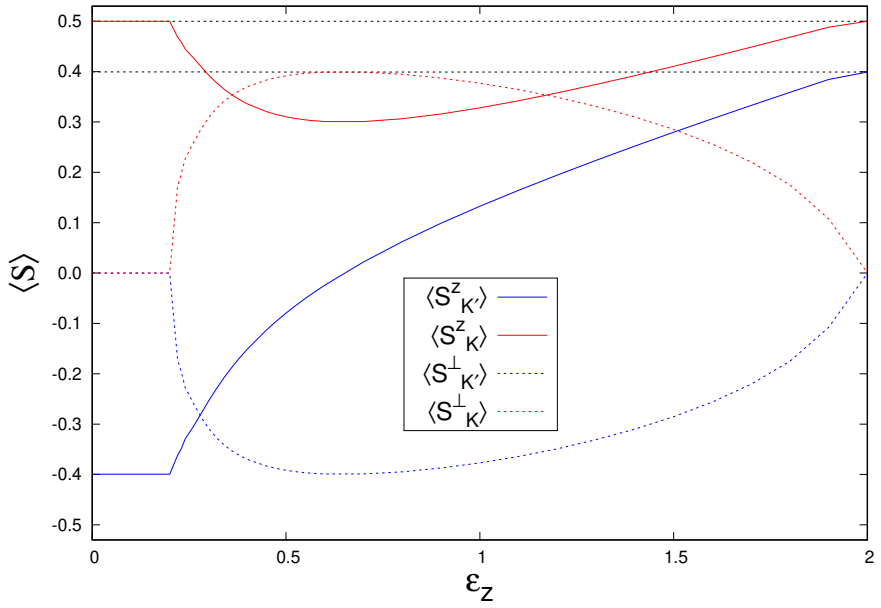

Figure 5.2: Components of spin for each valley at $\nu = -0.2$. The blue curves correspond to the K' (partially filled) valley, while the red curves correspond to the K (filled) valley. The components of spin along the Zeeman axis, taken to be in $\hat{\mathbf{z}}$, are represented by the solid lines, and the in-plane components, $\langle S^{\perp} \rangle = \pm\sqrt{\langle S^x \rangle^2 + \langle S^y \rangle^2}$, are represented by the dotted, red and blue, lines. The magnitude of the total spin, $\langle S \rangle = \sqrt{\langle S^{\perp} \rangle^2 + \langle S^z \rangle^2}$, is given by the black dotted line for each valley. Continuous transitions occur at $\varepsilon_z = 0.22$ (co-Fi-CAF) and $\varepsilon_z = 2$ (CAF-FM).

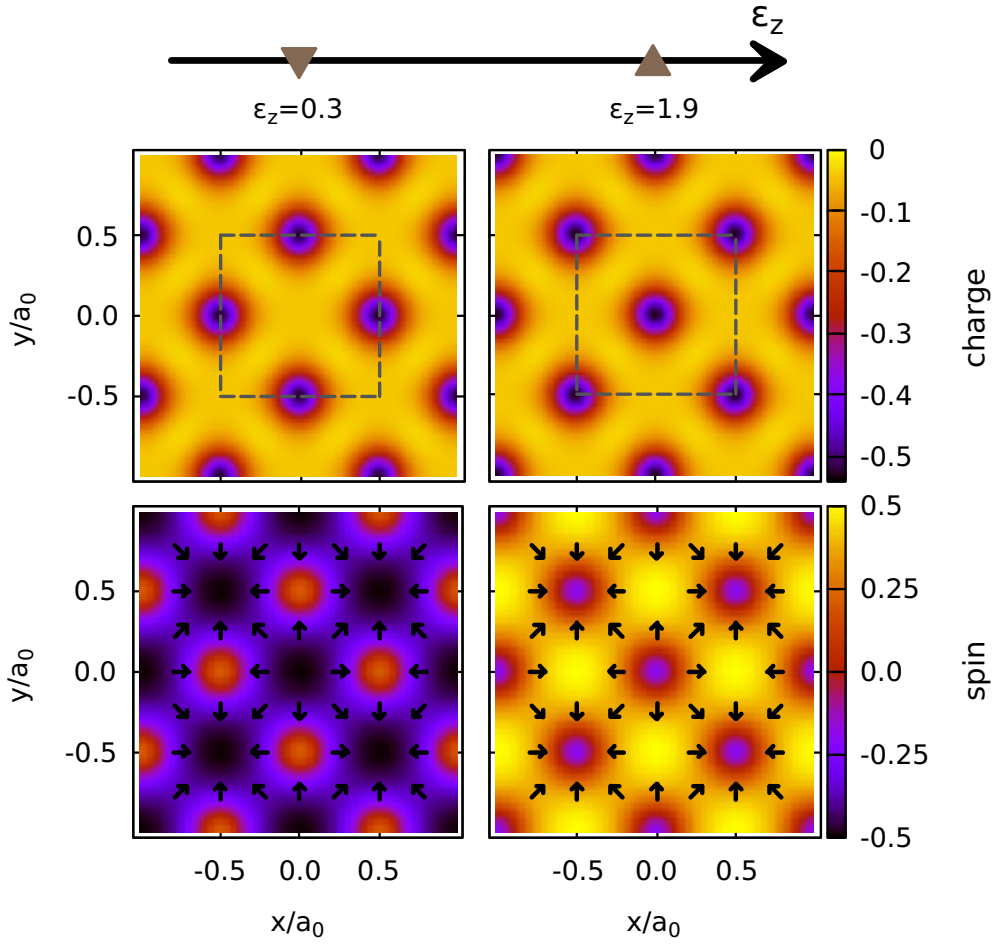

Figure 5.3: Lattice of skyrmions in the partially filled valley at filling factor $\nu = -0.11$. The colored contours shown in the top panels represent the local charge (occupation) density at $\varepsilon_z = 0.3$ (left) and $\varepsilon_z = 1.9$ (right). The perimeter of the unit cell is shown by the dashed line. Ground state regions, between the locations of the hole charge, correspond to $\nu = 0$, where the occupation of holes is zero. The bottom panels show the local spin density, where the contours represent the component of spin along the Zeeman axis, and the arrows represent in-plane spin components. For both spin plots, the Zeeman field points out of the page.

that is, the spin points in the direction of the Zeeman field at the core center. Away from the cores, the out-of-plane component of the (local) spin points in the opposite direction as the Zeeman field, yielding a spin majority that opposes the Zeeman field in the partially filled valley. Thus, the (ground state) regions between the skyrmions have the form of a co-Fi. The charge (top) and spin (bottom) densities for this type of lattice, at $\varepsilon_z = 0.3$ and $\nu = -0.11$, are shown in the left panels of Fig. 5.3. Notice that the hole charge is centered on the edges of the unit cell in this case.

For values of $\varepsilon_z > 1.1$, and below the transition to the FM, we obtain a lattice of skyrmions with anti-ferromagnetic cores. The out-of-plane components of the spin, in regions between skyrmions, now point in the same direction as the Zeeman field, yielding a HF state whose spin majority resembles the FM. Charge and spin densities of the unit cell for this state, at $\varepsilon_z = 1.9$ and $\nu = -0.11$, are shown in the right panels of Fig. 5.3. In this case, the hole charge is located at the center and corners of the unit cell. The number of skyrmions per unit cell in both of these charge figures is $N_{\rm uc} = 2$.

Near $\varepsilon_z = 1.1$, the black filled circles in the textured region of the phase diagram, we observe an interesting crossover phase resembling a lattice of merons. If we imagine starting at small values of the Zeeman parameter, say $\varepsilon_z = 0.3$, the majority of the hole charge is located on the edges of the unit cell. As we gradually increase the Zeeman parameter, the hole charge continuously migrates from the edges of the unit cell to the center and corners. The migration continues until there is an equal density of hole charge located at the center, edges, and corners of the unit cell, which occurs roughly at $\varepsilon_z = 1.1$ over a range of filling factors in the textured regions.

Furthermore, the global spin component along the Zeeman axis in the partially filled valley increases, and reaches zero at the crossover point, yielding a meron lattice. The overall, qualitative, structure of the spin density remains the same throughout this migration process. Charge and spin densities for the lattice are shown in Figs. 5.4a and 5.4b, respectively. For $\varepsilon_z > 1.1$, the hole charge continues to migrate so that the majority of the charge is located at the center and corners

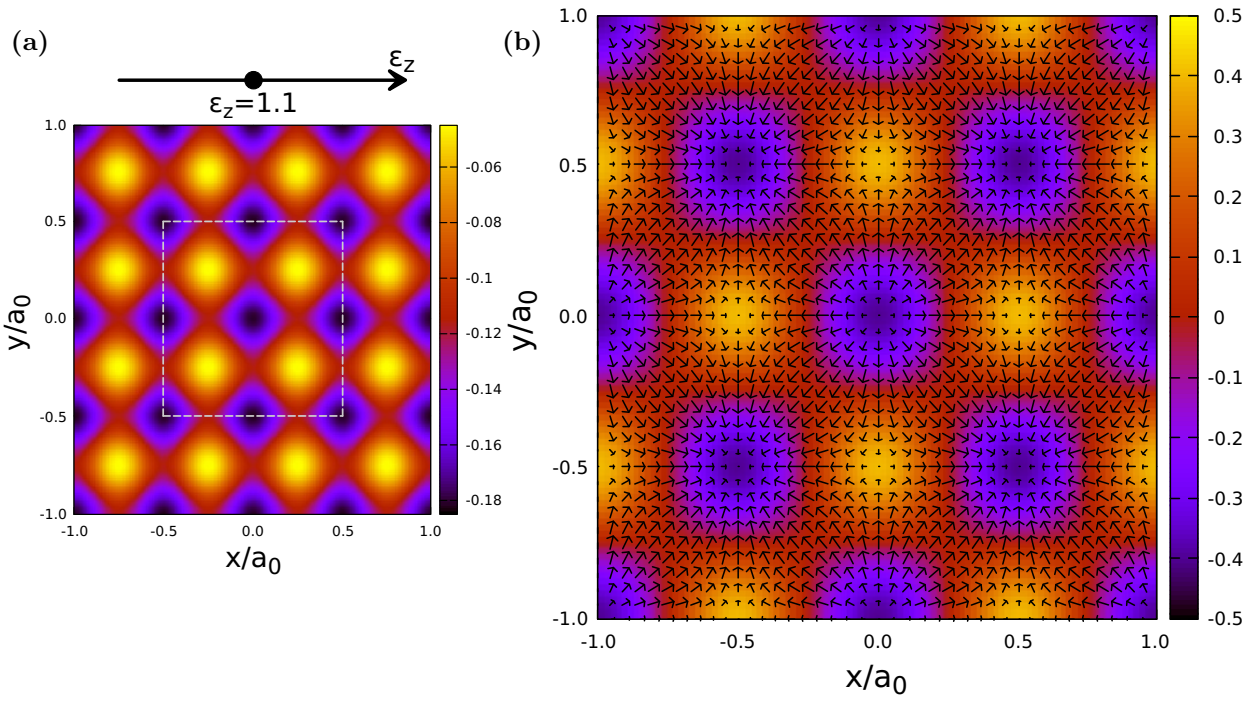

Figure 5.4: Lattice of merons in the partially filled valley at filling factor $\nu = -0.11$. (a) Charge density, represented by the colored contours, with dashed lines encompassing the unit cell. Since a meron can be essentially thought of as half of a skyrmion, there are four merons within the unit cell. (b) Spin density, with the Zeeman direction pointing out of the page. The contours represent the local spin along the Zeeman axis, while the arrows show the local in-plane spin directions.

of the unit cell, and we obtain a lattice of skyrmions with anti-ferromagnetic cores. Throughout this process, the energy is a smooth function of the Zeeman parameter. The question of whether the meron lattice signifies a phase transition will be discussed in last section of this chapter.

When the hole charge becomes very dilute, more RLV's are needed in the HF algorithm in order to reach convergence. Since the holes are very localized in real space, their density profiles become very spread out in reciprocal lattice space, and more RLV's are needed in order to fully capture the structure of the quasiparticles. For this reason, we were not able to explore the phase diagram for filling factors $-0.1 < \nu < 0$. We will discuss the states that might be present for this range of filling factors in the next section.

5.2 Stability of the closed shell configuration

Near $\nu = 0$, we would expect to see a lattice of spin textured quasiparticles (i.e., skyrmions or merons) with an underlying CAF spin structure, since the CAF is the ground state for small ε_z at $\nu = 0$. Moreover, there should be an equal density of holes with the same filling factor in each valley for such a state. Over the range of parameter space that we studied in this model, the HF algorithm was never able to stabilize a CAF state with spin textures in both valleys. The valley structure for every stable, well converged HF state always had the form of a closed shell configuration. Furthermore, a filled LL subbranch cannot host quasiparticles, and, hence, cannot form textures. An analogy can drawn here to Hund's rule for Fermions occupying sublevels of an orbital.

To better understand the stability of the closed shell configuration, we carried out a HF calculation, keeping only $\boldsymbol{G} = 0$ terms in the order parameter (terms with $\boldsymbol{G} \neq 0$ will not contribute to the energy as greatly as the uniform ones), for two types of valley configurations: closed shell and equal hole density (equally filled valleys). Keeping three LL's in the calculation, we found that the Coulomb energy contributed the largest difference in energy for these two valley configurations.

The energy difference for the OS interaction was one to two orders of magnitude smaller than the Coulomb energy difference. For $\boldsymbol{G} = 0$, only the Coulomb exchange energy is non-zero. The (divergent) Hartree energy is canceled by the uniform background. A plot of the Coulomb exchange energy, as a function of filling factor for each valley configuration, is shown in Fig. 5.5a. Indeed, the closed shell configuration is always lower in energy. Notice, however, that the two configurations become closer in energy, as we approach integer filling. For this energy calculation, we chose a spin polarized FM, although we obtain similar results for other types of spin configurations (i.e., CAF, AF, and co-Fi).

This effect can be seen analytically, even by retaining a single LL ($n = 0$) in the interaction energy. From eq. (4.7), the Coulomb exchange energy, $E_{\rm X}^{(\rm C)} \equiv -\left\langle \mathcal{H}_{\rm X}^{(\rm C)} \right\rangle$, for a given HF state is

$$E_{\rm X}^{(\rm C)} = -\frac{g}{S} \sum_{\boldsymbol{\xi}} f^{(\rm C)}(\boldsymbol{\tau}) \delta_{\sigma_1,\sigma_4} \delta_{\sigma_2,\sigma_3} \sum_{\boldsymbol{p}} \mathcal{M}^{(\rm C)}(\boldsymbol{n}, \boldsymbol{\tau}, \boldsymbol{p}) \left\langle \rho_{\xi_1\xi_3}(\boldsymbol{G} = 0) \right\rangle \left\langle \rho_{\xi_2\xi_4}(\boldsymbol{G} = 0) \right\rangle . \tag{5.1}$$

The functions, $\mathcal{M}^{(\rm C)}$, are given by eq. (2.29), and, since the Coulomb interaction is symmetric in valley, $f^{(\rm C)}(\boldsymbol{\tau}) = \delta_{\tau_1,\tau_4}\delta_{\tau_2,\tau_3}$. Keeping only the terms with $\boldsymbol{n} = 0$, converting the sum over $\boldsymbol{p}$ to an integral $\left(\frac{1}{S}\sum_{\boldsymbol{p}} \to \int \frac{d^2p}{(2\pi)^2}\right)$, and noting that

$$\begin{aligned} \int \frac{d^2p}{(2\pi)^2} \mathcal{M}^{(\rm C)}(\boldsymbol{n} = 0; \tau, \tau', \tau', \tau; \boldsymbol{p}) =& \frac{2\pi e^2}{4} \int \frac{d^2p}{(2\pi)^2} \frac{e^{-p^2\ell^2/2}}{p} \\ =& \frac{e^2\sqrt{2\pi}}{8\ell}, \end{aligned} \tag{5.2}$$

the Coulomb exchange energy reduces to

$$E_{\rm X}^{(\rm C)} = -g\frac{e^2\sqrt{2\pi}}{8\ell} \sum_{\tau} \sum_{\sigma,\sigma'} \left\langle \rho_{\sigma\tau,\sigma'\tau}(0) \right\rangle \left\langle \rho_{\sigma'\tau,\sigma\tau}(0) \right\rangle , \tag{5.3}$$

where we have excluded elements of the order parameter with $\tau \neq \tau'$, and dropped the labels on the LL index.

The two valley configurations of interest are modeled by

$$\sum_{\sigma} \left\langle \rho_{\sigma K',\sigma K'}(0) \right\rangle = \begin{cases} 1 + \frac{1}{2}\nu & \text{(equal hole density)} \\ 1 + \nu & \text{(closed shell),} \end{cases} \tag{5.4}$$

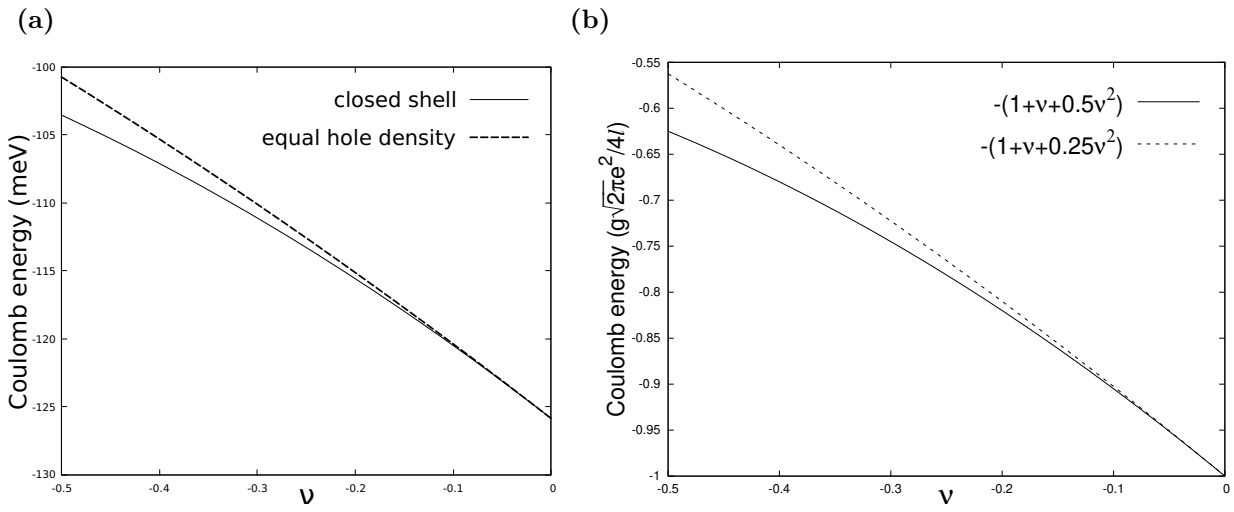

Figure 5.5: Coulomb exchange energy as a function of the total filling factor for the (a) numerical calculation with $N = 3$ and (b) the analytic calculation with $N = 1$. Terms with $\boldsymbol{G} \neq 0$ in the order parameter were not included in either of these calculations. For both plots, the dashed/dotted lines correspond to the equal hole density configuration. The closed shell configuration is represented by the solid line in both plots.

and

$$\sum_{\sigma} \langle \rho_{\sigma K,\sigma K}(0) \rangle = \begin{cases} 1 + \frac{1}{2}\nu & \text{(equal hole density)} \\ 1 & \text{(closed shell)}, \end{cases} \tag{5.5}$$

for each valley, with total filling factor $\nu < 0$. Assuming the state is spin polarized, the Coulomb exchange energy for each valley configuration becomes

$$E_{\mathrm{X}}^{(\mathrm{C})} = -g\frac{e^2\sqrt{2\pi}}{4\ell} \begin{cases} (1 + \nu + \frac{1}{4}\nu^2) & \text{(equal hole density - FM)} \\ (1 + \nu + \frac{1}{2}\nu^2) & \text{(closed shell - FM)}. \end{cases} \tag{5.6}$$

The form of the polynomials in eq. (5.6) always leads to a lower energy for the closed shell configuration, and the energy difference between the two configurations becomes larger as the hole density is increased. The energies are plotted in Fig. 5.5b, and are, qualitatively, very similar to the numerical result with three LL's (Fig. 5.5a). For the case when all LL indices are zero, and for $\boldsymbol{G} = 0$, the OS interaction only includes intra-valley terms. This ultimately leads to equal, and opposite, Hartree and exchange energies, which sum to zero, for the spin polarized case.

As we approach $\nu = 0$, the energy difference for the two configurations tends to zero, suggesting that the closed shell configuration may not be stable at hole densities that are sufficiently dilute. The large number of required RLV's for filling factors $-0.1 < \nu < 0$ makes it numerically difficult to probe the region where the quasiparticles are dilute. It is likely that textured states with underlying CAF spin structures will be present in that region. However, even at $\nu = -0.07$, with $N_G = 317$, we were not able to reach a reasonable convergence for our trial states.

5.3 Concluding remarks and connection to experiment

Throughout this study, we have only allowed for the possibility of square lattices of quasiparticles. This assumption is justified, at large filling of holes, when the charge is sufficiently dense, since square configurations accommodate textures that are lower in energy than, say, triangular lattices. However, it may be more appropriate to use a triangular or rectangular lattice when the density is more dilute. In that case, we may find that regions of the phase diagram in Fig. 5.1, closer to $\nu = 0$, are unstable to transitions to these other lattice types. Moreover, by using a rectangular lattice in the calculation, we can continuously deform the square lattice into a triangular lattice with two quasiparticles per unit cell. When the charge is dilute enough, one possible outcome is that the states in the textured regions will form a rectangular lattice of meron pairs.

The nature of the meron phase observed at the crossover point remains to be determined. There is a discrete symmetry present in the meron lattice, in which in-plane, $\pi/2$ rotations of the local spin, in addition to a translation of the unit cell by half a lattice constant, leaves the state unchanged. It also has the property that the spin component along the Zeeman axis in the partially filled valley vanishes, while the filled valley remains spin polarized.

A natural explanation for this behavior would be that the exchange interaction with the filled valley is acting like an effective Zeeman field, which is then canceling the real Zeeman interaction in the partially filled valley. If this were true, then small rotations of the spins away from the

Zeeman axis in the partially filled valley would leave the energy unchanged. However, such spin rotations lead to an increase in the state's energy. We therefore cannot classify the crossover as a phase transition using this type of rotational symmetry. In general, a ground state with a broken continuous symmetry has Goldstone modes, which means that there are excitations above the ground state that are gapless. Both types of skyrmion phases, on either side of the crossover, have a gapless collective excitation (Goldstone mode) associated with their broken U(1) symmetry. If there is an additional gapless collective mode present for the meron lattice, then the crossover point can be characterized as a phase transition. A more thorough investigation of the crossover phase would entail computing the collective excitations within the time-dependent HF approximation.

For any charged lattice, there are phonon excitations present. Furthermore, the broken U(1) symmetry for the CAF and spin textured phases support gapless, low energy spin wave excitations[46,47]. For the textured states, these spin waves are coupled to the phonon excitations, because of the spin-charge coupling arising from a non-zero Pontryagin density. The spin orientation is uniform throughout the lattice for the CAF phase, and so the Pontryagin density in that case is zero. Therefore, the phonon modes are completely decoupled from the spin waves. In principle, if it were possible to perform spin wave measurements in graphene, there should be signatures of phonons in the magnetic response and signatures of spin waves in the charge response, when the system is in one of these textured phases. Older experiments[48–50] in conventional 2DEG materials, such as GaAs heterostructures, used inelastic light scattering (Raman scattering) to measure spin wave excitations. When the sample absorbs circularly polarized light, and hence absorbs angular momentum, a spin flip excitation can occur, forming a spin wave. Unfortunately, these kinds of measurements prove much more challenging in graphene.

A more recent experiment[51] in graphene has observed signatures of spin wave excitations, built on top of the CAF ($\nu = 0$, for low enough Zeeman) and FM ($\nu = \pm 1$) bulk ground states at integer filling. For the FM ground state, the central region of a dual-gated graphene device is tuned to

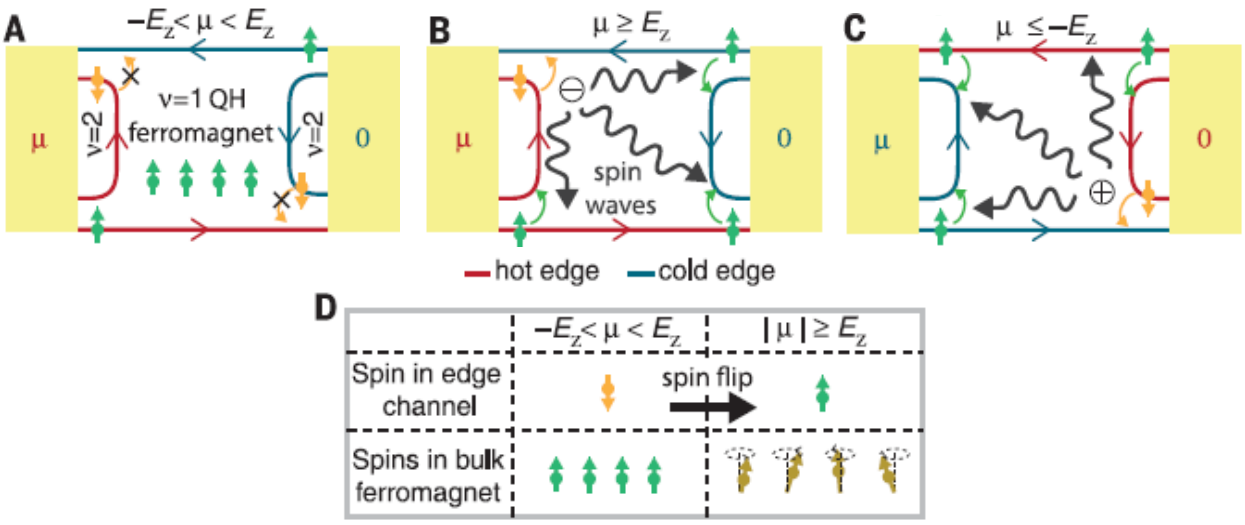

Figure 5.6: Experimental setup for generating and absorbing sipn waves. Figure reproduced from Ref. [51].

$\nu = 1$, while the adjacent sides are tuned to $\nu = 2$, corresponding to the fully filled, nonmagnetic, $n = 0$ LL (see Fig. 5.6A). Chiral edge states with opposite spin orientations propagate along the boundaries of the sample. Green arrows correspond to electrons whose spins are aligned with the external magnetic field and orange arrows are antiparallel to the field. A chemical potential difference, μ, is applied between the leads, so that edge channels labeled "hot" have a higher chemical potential than the "cold" edge channels. The Zeeman energy is given by E_z, and, as long as $|\mu| < E_z$, scattering between edge channels of opposite spin polarization is forbidden, since the system cannot absorb the resulting change in angular momentum [52,53].

When $|\mu| \geq E_z$, a spin down electron in a hot edge channel decays into a cold spin up channel. Figs. 5.6B and 5.6C show the two ways this decay process can happen. The spin flip results in the creation of a spin wave, which then propagates through the ferromagnetic bulk to a distant corner of the sample, and is absorbed by scattering an electron from a spin up channel to a spin down channel. When the spin wave is absorbed, the conductance at the edge deviates from the quantized value of e^2/h, indicating that spin and energy has been transported across the bulk of the system. Through a similar detection process, spin waves excitations were also observed for the CAF ground

state at $\nu = 0$.

When the system is doped away from integer filling, it may be challenging to distinguish between phases with and without textures. For example, in the context of our model, both the CAF and the spin textured phases, separated by a first order phase boundary (Fig. 5.1), will have spin wave excitations. The experimental geometry of Ref. [51], or other types of thermal transport experiments[54], could be one way of distinguishing the spin waves generated from these two phases. If the filling factor could be tuned in such an experiment, then, in principle, there should be some signature in the thermal conductivity when the system transitions from one phase into the other; moving through the transition should have a dramatic effect on the velocity of the spin waves, which may manifest as a cusp or a jump in the thermal conductivity, as a function of filling factor.

Chapter 6

Conclusion

6.1 Summary of thesis

In this work, multi-component phases of monolayer graphene in the quantum Hall regime near $\nu = 0$ were studied within a mean field Hartree-Fock (HF) approximation. The model was presented in the continuum limit, where the low energy physics is localized around two distinct Dirac points. The Dirac points also coincide with the two unique points, denoted K and K', in the first Brillouin zone for each of the two triangular sublattices. Collectively, the K and K' points can be thought of as a two-level pseudospin, also referred to as the valley pseudospin. Combinations of spin and valley ($\uparrow\downarrow \otimes KK'$) degrees of freedom form a single SU(4) isospin, which gives rise to a four-component sublevel structure within each Landau level (LL).

In the non-interacting picture, the cyclotron energies are degenerate with respect to both spin and valley. The model in this thesis included SU(4) symmetric electron-electron Coulomb interactions, in addition to SU(4) symmetry-breaking interactions. Spin degeneracies are lifted by the Zeeman splitting, while the microscopic on-site (OS) and nearest neighbor (NN) two-body interactions break the SU(4) symmetry with respect to valley. The microscopic interaction strengths, V_0 and V_1, for OS and NN, respectively, were treated as tunable parameters. An "active window" of LL's was explicitly retained, allowing for the possibility of LL mixing. The size of the window was left as a tunable parameter in the HF calculation. States with LL indices outside of the active window, and associated with energy levels below the chemical potential, belonged to the Dirac sea, and were "frozen" out of the calculation. We showed that only the Coulomb interaction contributed non-trivial structure to the Dirac sea, which was then included as a uniform background potential in the HF Hamiltonian.

At integer filling ($\nu = 0$), we found that LL mixing played a crucial role in determining the phase diagram; without higher order LL's ($|n| > 0$), only the ferromagnet (FM) and charge density wave (CDW) appeared in the phase diagram. Retaining a minimum of $N = 3$ ($n = -1, 0, 1$) LL's was enough to stabilize the canted anti-ferromagnet (CAF) in the phase diagram. A continuous transition between the CAF and FM phases was observed. However, for small window sizes, the transition point occurred at unphysically large values of V_0 and V_1, one to two orders of magnitude larger than their realistic values. Including more LL's in the active window greatly renormalized the phase boundaries. Using an extrapolation method, the final phase diagram (see Fig. 2.6a) showed excellent agreement with experiment [14]. The Kekulé-distortion state was never stable in the phase diagrams that we obtained.

At noninteger filling ($\nu < 0$), we focused on states with and without spin textures. The operators introduced in section **??** mapped states in the guiding center, $X = k\ell^2$, representation to states described by reciprocal lattice vectors (RLV's). The HF Hamiltonian was studied in the context of a Heisenberg equation of motion, using single particle Matsubara Green's functions to extract information about the order parameter. Three active LL's were retained in the calculation, so that all of the relevant phases present at $\nu = 0$ could be qualitatively captured.

A phase diagram was constructed within the space of the Zeeman parameter, ε_z, and total filling factor (see Fig. 5.1). Every state appearing in the phase diagram carried a valley structure resembling the "closed shell" configuration, in which one valley was completely filled and spatially uniform, while the other valley was partially filled. Quasiparticles only formed in the partially filled valley. At larger hole densities, we find states without textures, consisting of the FM, CAF, and collinear-ferrimagnet (co-Fi), which are characterized by their overall spin structure. The boundaries between the co-Fi-CAF and CAF-FM regions are described by continuous phase transitions. When the hole density is small, spin textured states appear in the phase diagram. In this region, a lattice of skyrmions are formed in a single valley, and have ferromagnetic (anti-ferromagnetic) cores

at small (large) values of ε_z. The filled valley always remains spin polarized in the direction of the Zeeman field in the textured region. The overall spin structure, i.e., the majority spin direction in the ground state region between the cores of the skyrmions, for states with ferromagnetic-core skyrmions had the form of a co-Fi. For states with skyrmions having anti-ferromagnetic cores, the overall spin structure resembled a FM. As a function of ε_z, the hole charge associated with the skrymion lattice continuously migrates to locations of the unit cell in such a way that, at some particular value of ε_z, we obtain a lattice of merons. In this crossover phase, the spin component along the Zeeman axis, in the partially filled valley, goes to zero, and there is an equal density of holes located at the center, edges, and corners of the unit cell.

6.2 Outlook

There are a number of interesting avenues for future work, as well as several areas of current research that are related to the model presented in this thesis. As discussed in the previous chapter, computing the collective modes for the HF states obtained at noninteger filling would give insight into the nature of the crossover phase in the textured region of Fig. 5.1; such a calculation would give an unbiased way of determining whether or not an additional gapless collective mode exists at the crossover. If it does exist, then the crossover could be classified as a phase transition. Additionally, the impact of quantum fluctuations on these mean field HF states may be nontrivial. For example, when quantum fluctuations are included, collective excitations can admix into the ground state. Developing quantum field theoretic models would be required to analyze such effects. Furthermore, allowing for the possibility of other lattice configurations may lead to HF states which are lower in energy, compared to square configurations, in some regions of the phase diagram.

In our study of non-uniform states, we only retained three active LL's in the calculation. Given the critical role that LL mixing played at integer filling, it is interesting to consider what effect it may have on the HF states at noninteger filling. For example, what would the effect be on the

stability of the closed shell configuration if more active LL's are included? Investigating the effects of higher order LL's is, in principle, straight forward within the context of this model. However, given the already large parameter space, including more LL's may prove numerically challenging. More sophisticated diagonalization schemes, such as exploiting symmetries of the lattice, would improve the efficiency of the algorithm.

The importance of having symmetry-breaking interactions has driven much of the theoretical research in monolayer graphene over the last several years, particularly at filling factors within the $n = 0$ LL ($\nu = -1, 0, 1$). For example, recent studies[55–57] at odd integer values, $\nu = \pm 1$, in which skyrmions are studied using exact diagonalization on spherical geometries and variational methods in a CP^3 field theory, find a rich variety of spin and pseudospin textured phases. These models include the anisotropy interactions, as discussed in Ref. [6], responsible for breaking the SU(4) symmetry. The model presented in this thesis can also be extended to study filling factors at, or in the vicinity of, other integer values. Given the four component nature of each LL in graphene, and the role of SU(4) symmetry-breaking interactions, there are a wide variety of possible ground states that could be realized at other filling factors.

In recent years, multilayer systems such as bilayer graphene (BLG) have also received considerable interest. Unlike monolayer graphene (MLG), Bernal stacked BLG has a unit cell with four atomic sites, giving rise to four energy bands that disperse quadratically about the K and K' points[58,59]. Two of these bands touch at the Dirac points (zero energy), while the other two are separated by a gap that arises from nearest neighbor interlayer hopping. The Hamiltonian can be projected into a low energy subspace, yielding the same number of discrete degrees of freedom as monolayer graphene. Furthermore, an electric field applied perpendicular to the sample induces a band gap in the low energy spectrum, leading to the possibility of tuning the relative concentration of electrons between the two layers[60]. Tuning the layer pseudospin by applying an electric field can offer insight into the nature of the ground states in the quantum Hall regime of BLG. For

example, similar to observations in MLG, an insulating state at $\nu = 0$ has recently been observed in BLG [61–65]. A mean field study [66] of this system concluded that the insulating state is likely a CAF ordered phase. More recent experiments [67–70] involving high-resolution spectroscopic measurements have revealed a rich variety of LL splittings in intermediate phases at $\nu = 0$, due to the presence of many-body effects. Beyond these findings, there are still many open questions regarding the nature of phase transitions and collective excitations in these systems.

Since the discovery of graphene in 2004, a wide variety of other 2D materials have been synthesized and studied. Monolayer 2D materials with strong in-plane covalent bonding (like graphene) and weak interlayer interactions are generally classified as van der Waals (vdW) materials. Phosphorene [71,72], the monolayer form of black phosphorus (BP), is one such example, and has a puckered honeycomb lattice composed entirely of phosphorus atoms. Few-layer BP systems have gained substantial attention in the last several years because of its wide range of physical properties. BP semiconductors have high carrier mobilities [73,74], which persists even at room temperature, and a band gap that can be tuned either by changing the number of layers or applying an external field [75–79]. In addition, the quantum Hall effect has also been has also been observed in these systems [80]. A number of recent theoretical studies [81–83] have examed the LL spectrum in monolayer and bilayer phosphorene.

Transition metal dichalcogenides (TMDs) [84] are another type of (monolayer) 2D vdW materials that have many of the same properties as BP (i.e., high carrier mobility as well as direct band gaps). These semiconductors are of the form MX_2, where M is a transition metal (Mo or W) and X denotes a chalcogen atom (S, Se, Te). The properties of TMD heterostructures (TMD-TMD, TMD-graphene, etc.) drive much of the ongoing interest in these materials. For example, the strong spin-orbit coupling exhibited by TMDs can induce strong spin-orbit interactions in graphene [85,86]. Further studies of these materials in the quantum Hall regime remains as an active field of research.

Bibliography

[1] K. S. Novoselov, A. K. Geim, S. V. Morozov, D. Jiang, Y. Zhang, S. V. Dubonos, I. V. Grigorieva, and A. A. Firsov. Electric field effect in atomically thin carbon films. *Science*, 306(5696):666–669, 2004.

[2] C Dean, A Young, I Meric, Changgu Lee, Lei Wang, S Sorgenfrei, K Watanabe, Takashi Taniguchi, Phaly Kim, K Shepard, and James Hone. Boron nitride substrates for high-quality graphene electronics. *Nature nanotechnology*, 5:722–6, 10 2010.

[3] B. Partoens and F. M. Peeters. From graphene to graphite: Electronic structure around the k point. *Phys. Rev. B*, 74:075404, Aug 2006.

[4] M. Mucha-Kruczyński, O. Tsyplyatyev, A. Grishin, E. McCann, Vladimir I. Fal'ko, Aaron Bostwick, and Eli Rotenberg. Characterization of graphene through anisotropy of constant-energy maps in angle-resolved photoemission. *Phys. Rev. B*, 77:195403, May 2008.

[5] C. W. J. Beenakker. Colloquium: Andreev reflection and klein tunneling in graphene. *Reviews of Modern Physics*, 80(4):13371354, Oct 2008.

[6] Maxim Kharitonov. Phase diagram for the $\nu = 0$ quantum hall state in monolayer graphene. *Phys. Rev. B*, 85:155439, Apr 2012.

[7] Yuanbo Zhang, Yan-Wen Tan, Horst Stormer, and Philip Kim. Experimental observation of the quantum hall effect and berry's phase in graphene. *Nature*, 438:201–4, 12 2005.

[8] K. Novoselov, A.K. Geim, S. Morozov, Dingde Jiang, Mikhail Katsnelson, Irina Grigorieva, S.V. Dubonos, and Anatoly Firsov. Two-dimensional gas of massless dirac fermions in graphene. *Nature*, 438:197–200, 12 2005.

[9] David Tong. Lectures on the quantum hall effect, 2016.

[10] Z. Jiang, Y. Zhang, H. L. Stormer, and P. Kim. Quantum hall states near the charge-neutral dirac point in graphene. *Physical Review Letters*, 99(10), Sep 2007.

[11] Kentaro Nomura and Allan H. MacDonald. Quantum hall ferromagnetism in graphene. *Physical Review Letters*, 96(25), Jun 2006.

[12] Luis Brey and H. A. Fertig. Edge states and the quantized hall effect in graphene. *Physical Review B*, 73(19), May 2006.

[13] Louis Veyrat, Corentin Déprez, Alexis Coissard, Xiaoxi Li, Frédéric Gay, Kenji Watanabe, Takashi Taniguchi, Zheng Han, Benjamin A. Piot, Hermann Sellier, and Benjamin Sacépé. Helical quantum hall phase in graphene on srtio3. *Science*, 367(6479):781–786, 2020.

[14] A. F. Young, J. D. Sanchez-Yamagishi, B. Hunt, S. H. Choi, K. Watanabe, T. Taniguchi, R. C. Ashoori, and P. Jarillo-Herrero. Tunable symmetry breaking and helical edge transport in a graphene quantum spin hall state. *Nature*, 505(7484):528532, Dec 2013.

[15] Igor F. Herbut. Theory of integer quantum hall effect in graphene. *Phys. Rev. B*, 75:165411, Apr 2007.

[16] V. P. Gusynin, V. A. Miransky, S. G. Sharapov, and I. A. Shovkovy. Excitonic gap, phase transition, and quantum hall effect in graphene. *Phys. Rev. B*, 74:195429, Nov 2006.

[17] V. P. Gusynin, V. A. Miransky, S. G. Sharapov, and I. A. Shovkovy. Edge states, mass and spin gaps, and quantum hall effect in graphene. *Phys. Rev. B*, 77:205409, May 2008.

[18] Bitan Roy, Malcolm P. Kennett, and S. Das Sarma. Chiral symmetry breaking and the quantum hall effect in monolayer graphene. *Phys. Rev. B*, 90:201409, Nov 2014.

[19] J. L. Lado and J. Fernández-Rossier. Noncollinear magnetic phases and edge states in graphene quantum hall bars. *Phys. Rev. B*, 90:165429, Oct 2014.

[20] Vinu Lukose and R. Shankar. Coulomb interactions, dirac sea polarization, and $su(4)$ symmetry breaking of the integer quantum hall states of graphene. *Phys. Rev. B*, 94:085135, Aug 2016.

[21] Jason Alicea and Matthew P. A. Fisher. Graphene integer quantum hall effect in the ferromagnetic and paramagnetic regimes. *Phys. Rev. B*, 74:075422, Aug 2006.

[22] M. O. Goerbig, R. Moessner, and B. Douçot. Electron interactions in graphene in a strong magnetic field. *Phys. Rev. B*, 74:161407, Oct 2006.

[23] Jean-Noël Fuchs and Pascal Lederer. Spontaneous parity breaking of graphene in the quantum hall regime. *Phys. Rev. Lett.*, 98:016803, Jan 2007.

[24] Csaba Tke, Paul E. Lammert, Vincent H. Crespi, and Jainendra K. Jain. Fractional quantum hall effect in graphene. *Physical Review B*, 74(23), Dec 2006.

[25] Dmitry A. Abanin, Patrick A. Lee, and Leonid S. Levitov. Spin-filtered edge states and quantum hall effect in graphene. *Phys. Rev. Lett.*, 96:176803, May 2006.

[26] H. A. Fertig and L. Brey. Luttinger liquid at the edge of undoped graphene in a strong magnetic field. *Phys. Rev. Lett.*, 97:116805, Sep 2006.

[27] E. Shimshoni, H. A. Fertig, and G. Venketeswara Pai. Onset of an insulating zero-plateau quantum hall state in graphene. *Phys. Rev. Lett.*, 102:206408, May 2009.

[28] Ganpathy Murthy, Efrat Shimshoni, and H. A. Fertig. Collective edge modes near the onset of a graphene quantum spin hall state. *Phys. Rev. B*, 90:241410, Dec 2014.

[29] Ganpathy Murthy, Efrat Shimshoni, and H. A. Fertig. Collective bulk and edge modes through the quantum phase transition in graphene at $\nu = 0$. *Phys. Rev. B*, 93:045105, Jan 2016.

[30] Pavel Tikhonov, Efrat Shimshoni, H. A. Fertig, and Ganpathy Murthy. Emergence of helical edge conduction in graphene at the $\nu = 0$ quantum hall state. *Phys. Rev. B*, 93:115137, Mar 2016.

[31] A. F. Young, C. R. Dean, L. Wang, H. Ren, P. Cadden-Zimansky, K. Watanabe, T. Taniguchi, J. Hone, K. L. Shepard, and P. Kim. Spin and valley quantum hall ferromagnetism in graphene. *Nature Physics*, 8(7):550556, May 2012.

[32] Braden Feshami and H. A. Fertig. Hartree-fock study of the $\nu = 0$ quantum hall state of monolayer graphene with short-range interactions. *Phys. Rev. B*, 94:245435, Dec 2016.

[33] T. O. Wehling, E. Şaşıoğlu, C. Friedrich, A. I. Lichtenstein, M. I. Katsnelson, and S. Blügel. Strength of effective coulomb interactions in graphene and graphite. *Phys. Rev. Lett.*, 106:236805, Jun 2011.

[34] M. O. Goerbig. Electronic properties of graphene in a strong magnetic field. *Rev. Mod. Phys.*, 83:1193–1243, Nov 2011.

[35] H. A. Fertig, L. Brey, R. Côté, and A. H. MacDonald. Charged spin-texture excitations and the hartree-fock approximation in the quantum hall effect. *Phys. Rev. B*, 50:11018–11021, Oct 1994.

[36] R. Rajaraman. *Solitons and Instantons. An Introduction to Solitons and Instantons in Quantum Field Theory.* 1982.

[37] Wenchen Luo. *Skyrmions in monolayer and bilayer graphene.* PhD thesis, UNIVERSITE DE SHERBROOKE, 2009.

[38] Steven M. Girvin. The quantum hall effect: Novel excitations and broken symmetries, 1999.

[39] S. M. Girvin and A. H. MacDonald. *Multicomponent Quantum Hall Systems: The Sum of Their Parts and More*, chapter 5, pages 161–224. John Wiley Sons, Ltd, 2007.

[40] L. Brey, H. A. Fertig, R. Côté, and A. H. MacDonald. Skyrme crystal in a two-dimensional electron gas. *Phys. Rev. Lett.*, 75:2562–2565, Sep 1995.

[41] Lynn Bonsall and A. A. Maradudin. Some static and dynamical properties of a two-dimensional wigner crystal. *Phys. Rev. B*, 15:1959–1973, Feb 1977.

[42] R. Côté, J.-F. Jobidon, and H. A. Fertig. Skyrme and wigner crystals in graphene. *Phys. Rev. B*, 78:085309, Aug 2008.

[43] R. Côté and A. H. MacDonald. Collective modes of the two-dimensional wigner crystal in a strong magnetic field. *Phys. Rev. B*, 44:8759–8773, Oct 1991.

[44] C.-H. Zhang and Yogesh N. Joglekar. Wigner crystal and bubble phases in graphene in the quantum hall regime. *Phys. Rev. B*, 75:245414, Jun 2007.

[45] Wenchen Luo and R. Côté. Zeeman coupling and screening corrections to skyrmion excitations in graphene. *Phys. Rev. B*, 88:115417, Sep 2013.

[46] So Takei, Amir Yacoby, Bertrand I. Halperin, and Yaroslav Tserkovnyak. Spin superfluidity in the $\nu = 0$ quantum hall state of graphene. *Phys. Rev. Lett.*, 116:216801, May 2016.

[47] AG Green and N. Cooper. Dissipative transport in quantum hall ferromagnets by spinwave scattering. *Phys. Rev. B*, 65, 03 2002.

[48] A. Pinczuk, B. S. Dennis, D. Heiman, C. Kallin, L. Brey, C. Tejedor, S. Schmitt-Rink, L. N. Pfeiffer, and K. W. West. Spectroscopic measurement of large exchange enhancement of a spin-polarized 2d electron gas. *Phys. Rev. Lett.*, 68:3623–3626, Jun 1992.

[49] A. Pinczuk, J. P. Valladares, D. Heiman, A. C. Gossard, J. H. English, C. W. Tu, L. Pfeiffer, and K. West. Observation of roton density of states in two-dimensional landau-level excitations. *Phys. Rev. Lett.*, 61:2701–2704, Dec 1988.

[50] M. A. Eriksson, A. Pinczuk, B. S. Dennis, S. H. Simon, L. N. Pfeiffer, and K. W. West. Collective excitations in the dilute 2d electron system. *Phys. Rev. Lett.*, 82:2163–2166, Mar 1999.

[51] Di Wei, Toeno van der Sar, Seung Lee, Kenji Watanabe, Takashi Taniguchi, Bertrand Halperin, and Amir Yacoby. Electrical generation and detection of spin waves in a quantum hall ferromagnet. *Science*, 362, 01 2018.

[52] F. Amet, J. R. Williams, K. Watanabe, T. Taniguchi, and D. Goldhaber-Gordon. Selective equilibration of spin-polarized quantum hall edge states in graphene. *Phys. Rev. Lett.*, 112:196601, May 2014.

[53] Di S. Wei, Toeno van der Sar, Javier D. Sanchez-Yamagishi, Kenji Watanabe, Takashi Taniguchi, Pablo Jarillo-Herrero, Bertrand I. Halperin, and Amir Yacoby. Mach-zehnder interferometry using spin- and valley-polarized quantum hall edge states in graphene. *Science Advances*, 3(8), 2017.

[54] Falko Pientka, Jonah Waissman, Philip Kim, and Bertrand I. Halperin. Thermal transport signatures of broken-symmetry phases in graphene. *Physical Review Letters*, 119(2), Jul 2017.

[55] Yunlong Lian and Mark O. Goerbig. Spin-valley skyrmions in graphene at filling factor $\nu = -1$. *Physical Review B*, 95(24), Jun 2017.

[56] Y. Lian, A. Rosch, and M. O. Goerbig. Su(4) skyrmions in the $\nu = \pm 1$ quantum hall state of graphene. *Phys. Rev. Lett.*, 117:056806, Jul 2016.

[57] Thierry Jolicoeur and Bradraj Pandey. Quantum hall skyrmions at $\nu = 0, \pm 1$ in monolayer graphene. *Phys. Rev. B*, 100:115422, Sep 2019.

[58] Edward McCann and Mikito Koshino. The electronic properties of bilayer graphene. *Reports on Progress in Physics*, 76(5):056503, apr 2013.

[59] Alexandr Vladimirovich Rozhkov, A. O. Sboychakov, A. L. Rakhmanov, and Franco Nori. Electronic properties of graphene-based bilayer systems. *Physics Reports*, 648:1–104, 2016.

[60] Kin Fai Mak, Chun Hung Lui, Jie Shan, and Tony F. Heinz. Observation of an electric-field-induced band gap in bilayer graphene by infrared spectroscopy. *Phys. Rev. Lett.*, 102:256405, Jun 2009.

[61] R. T. Weitz, M. T. Allen, B. E. Feldman, J. Martin, and A. Yacoby. Broken-symmetry states in doubly gated suspended bilayer graphene. *Science*, 330(6005):812–816, 2010.

[62] Benjamin E. Feldman, Jens Martin, and Amir Yacoby. Broken-symmetry states and divergent resistance in suspended bilayer graphene. *Nature Physics*, 5(12):889893, Sep 2009.

[63] Y. Zhao, P. Cadden-Zimansky, Z. Jiang, and P. Kim. Symmetry breaking in the zero-energy landau level in bilayer graphene. *Phys. Rev. Lett.*, 104:066801, Feb 2010.

[64] F. Freitag, J. Trbovic, M. Weiss, and C. Schönenberger. Spontaneously gapped ground state in suspended bilayer graphene. *Phys. Rev. Lett.*, 108:076602, Feb 2012.

[65] J. Velasco, L. Jing, W. Bao, Y. Lee, P. Kratz, V. Aji, M. Bockrath, C. N. Lau, C. Varma, R. Stillwell, and et al. Transport spectroscopy of symmetry-broken insulating states in bilayer graphene. *Nature Nanotechnology*, 7(3):156160, Jan 2012.

[66] Maxim Kharitonov. Canted antiferromagnetic phase of the=0quantum hall state in bilayer graphene. *Physical Review Letters*, 109(4), Jul 2012.

[67] Long-Jing Yin, Li-Juan Shi, Li-Zhen Yang, Ling-Hui Tong, and Lin He. Spectroscopic characterization of landau-level splitting and the intermediate $\nu = 0$ phase in bilayer graphene. *Physical Review B*, 101(16), Apr 2020.

[68] B. M. Hunt, J. I. A. Li, A. A. Zibrov, L. Wang, T. Taniguchi, K. Watanabe, J. Hone, C. R.

Dean, M. Zaletel, R. C. Ashoori, and et al. Direct measurement of discrete valley and orbital quantum numbers in bilayer graphene. *Nature Communications*, 8(1), Oct 2017.

[69] Jing Li, Hailong Fu, Zhenxi Yin, Kenji Watanabe, Takashi Taniguchi, and Jun Zhu. Metallic phase and temperature dependence of the $\nu = 0$ quantum hall state in bilayer graphene. *Phys. Rev. Lett.*, 122:097701, Mar 2019.

[70] P. Maher, C. Dean, A. Young, Takashi Taniguchi, K. Watanabe, K. Shepard, James Hone, and Phaly Kim. Evidence for a spin phase transition at charge neutrality in bilayer graphene. *Nature Physics*, 9:154–158, 03 2013.

[71] Andres Castellanos-Gomez, Leonardo Vicarelli, Elsa Prada, Joshua O Island, K L Narasimha-Acharya, Sofya I Blanter, Dirk J Groenendijk, Michele Buscema, Gary A Steele, J V Alvarez, Henny W Zandbergen, J J Palacios, and Herre S J van der Zant. Isolation and characterization of few-layer black phosphorus. *2D Materials*, 1(2):025001, jun 2014.

[72] Han Liu, Adam T. Neal, Zhen Zhu, Zhe Luo, Xianfan Xu, David Tomnek, and Peide D. Ye. Phosphorene: An unexplored 2d semiconductor with a high hole mobility. *ACS Nano*, 8(4):4033–4041, 2014. PMID: 24655084.

[73] Steven P. Koenig, Rostislav A. Doganov, Hennrik Schmidt, A. H. Castro Neto, and Barbaros zyilmaz. Electric field effect in ultrathin black phosphorus. *Applied Physics Letters*, 104(10):103106, 2014.

[74] Pengfei Chen, Neng Li, Xingzhu Chen, Wee-Jun Ong, and Xiujian Zhao. The rising star of 2d black phosphorus beyond graphene: synthesis, properties and electronic applications. *2D Materials*, 5(1):014002, oct 2017.

[75] Vy Tran, Ryan Soklaski, Yufeng Liang, and Li Yang. Layer-controlled band gap and anisotropic excitons in few-layer black phosphorus. *Phys. Rev. B*, 89:235319, Jun 2014.

[76] Likai Li, Jonghwan Kim, Chenhao Jin, Guo Jun Ye, Diana Y. Qiu, Felipe H. da Jornada, Zhiwen Shi, Long Chen, Zuocheng Zhang, Fangyuan Yang, and et al. Direct observation of the layer-dependent electronic structure in phosphorene. *Nature Nanotechnology*, 12(1):2125, Sep 2016.

[77] Guowei Zhang, Andrey Chaves, Shenyang Huang, Song Chaoyu, Tony Low, Steve Yan, and Ongun Ozcelik. Infrared fingerprints of few-layer black phosphorus. *Nature Communications*, 8:14071, 01 2017.

[78] Bingchen Deng, Vy Tran, Yujun Xie, Hao Jiang, Cheng Li, Qiushi Guo, Xiaomu Wang, He Tian, Steven J. Koester, Han Wang, and et al. Efficient electrical control of thin-film black phosphorus bandgap. *Nature Communications*, 8(1), Apr 2017.

[79] Yanpeng Liu, Zhizhan Qiu, Alexandra Carvalho, Yang Bao, Hai Xu, Sherman J. R. Tan, Wei Liu, A. H. Castro Neto, Kian Ping Loh, and Jiong Lu. Gate-tunable giant stark effect in few-layer black phosphorus. *Nano Letters*, 17(3):1970–1977, 2017. PMID: 28195492.

[80] Likai Li, Fangyuan Yang, Guo Jun Ye, Zuocheng Zhang, Zengwei Zhu, Wenkai Lou, Xiaoying Zhou, Liang Li, Kenji Watanabe, Takashi Taniguchi, and et al. Quantum hall effect in black phosphorus two-dimensional electron system. *Nature Nanotechnology*, 11(7):593597, Mar 2016.

[81] X. Y. Zhou, R. Zhang, J. P. Sun, Y. L. Zou, D. Zhang, W. K. Lou, F. Cheng, G. H. Zhou, F. Zhai, and Kai Chang. Landau levels and magneto-transport property of monolayer phosphorene. *Scientific Reports*, 5(1), Jul 2015.

[82] J. M. Pereira and M. I. Katsnelson. Landau levels of single-layer and bilayer phosphorene. *Physical Review B*, 92(7), Aug 2015.

[83] Dali Wang, Aiying Shen, Jian-Ping Lv, and Guojun Jin. Unique landau-level structure of

monolayer black phosphorus under an exponentially decaying magnetic field. *Journal of Physics: Condensed Matter*, 32(9):095301, nov 2019.

[84] Kin Fai Mak, Changgu Lee, James Hone, Jie Shan, and Tony F. Heinz. Atomically thin mos_2: A new direct-gap semiconductor. *Phys. Rev. Lett.*, 105:136805, Sep 2010.

[85] T. Wakamura, F. Reale, P. Palczynski, M. Q. Zhao, A. T. C. Johnson, S. Guéron, C. Mattevi, A. Ouerghi, and H. Bouchiat. Spin-orbit interaction induced in graphene by transition metal dichalcogenides. *Phys. Rev. B*, 99:245402, Jun 2019.

[86] C. K. Safeer, Josep Ingla-Ayns, Franz Herling, Jos H. Garcia, Marc Vila, Nerea Ontoso, M. Reyes Calvo, Stephan Roche, Luis E. Hueso, and Flix Casanova. Room-temperature spin hall effect in graphene/mos2 van der waals heterostructures. *Nano Letters*, 19(2):1074–1082, 2019.

Appendix A

Spatial Integrals

In this section, we show that

$$\int d\boldsymbol{r}\, \langle \boldsymbol{r}|\tau, n, k, s\rangle^*\, e^{i\boldsymbol{q}\cdot\boldsymbol{r}}\, \langle \boldsymbol{r}|\tau', n', k', s\rangle = e^{iq_x(k+k')\ell^2/2} T^{\tau,\tau'}_{n,n'}(\boldsymbol{q}, s)\delta_{k,k'-q_y}, \tag{A.1}$$

with

$$\begin{aligned}
\langle \boldsymbol{r}|\tau = +1, n, k, s\rangle &= \frac{\sqrt{2}^{\delta_{n,0}}}{\sqrt{2}}\big[-\mathrm{sgn}(n) h_{|n|-1,k}(\boldsymbol{r})\delta_{s,A} + h_{|n|,k}(\boldsymbol{r})\delta_{s,B}\big], \\
\langle \boldsymbol{r}|\tau = -1, n, k, s\rangle &= \frac{\sqrt{2}^{\delta_{n,0}}}{\sqrt{2}}\big[h_{|n|,k}(\boldsymbol{r})\delta_{s,A} + \mathrm{sgn}(n) h_{|n|-1,k}(\boldsymbol{r})\delta_{s,B}\big],
\end{aligned} \tag{A.2}$$

and Landau eigenstates,

$$h_{n,k}(\boldsymbol{r}) = \left(\frac{1}{\pi\ell^2 L_y^2}\right)^{1/4} \frac{1}{\sqrt{2^n n!}} e^{-iky} e^{-[(x-k\ell^2)^2/(2\ell^2)]} H_n\left(\frac{x-k\ell^2}{\ell}\right), \tag{A.3}$$

which are written in terms of Hermite polynomials, $H_n(x)$. Also, recall that the guiding center, X, is related to the momentum by $X = k\ell^2$. We begin by noting that a generic term in the integrand comes with a product of the $h_{n,k}(\boldsymbol{r})$ functions. Then, for any positive integer, m, j,

$$\begin{aligned}
&\int d\boldsymbol{r}\; e^{i\boldsymbol{q}\cdot\boldsymbol{r}} h^*_{m,k}(\boldsymbol{r}) h_{j,k'}(\boldsymbol{r}) \\
&= C_m C_j \int d\boldsymbol{r}\; e^{i\boldsymbol{q}\cdot\boldsymbol{r}} e^{i(k-k')y} e^{-[(x-X)^2/(2\ell^2)+(x-X')^2/(2\ell^2)]} H_m\left(\frac{x-X}{\ell}\right) H_j\left(\frac{x-X'}{\ell}\right) \\
&= C_m C_j L_y\; \delta_{k,k'-q_y} \int dx\; e^{iq_x x - [(x-X)^2/(2\ell^2)+(x-X')^2/(2\ell^2)]} H_m\left(\frac{x-X}{\ell}\right) H_j\left(\frac{x-X'}{\ell}\right) \\
&= C_m C_j L_y\; \delta_{k,k'-q_y} e^{iq_x(X+X')/2} e^{-q^2\ell^2/4} \\
&\qquad\qquad \times \int_{-\infty}^{\infty} dx\; e^{-[x/\ell - i(q_x - iX/\ell^2 - iX'/\ell^2)\ell/2]^2} H_m\left(\frac{x-X}{\ell}\right) H_j\left(\frac{x-X'}{\ell}\right),
\end{aligned} \tag{A.4}$$

where $C_n \equiv \left(\frac{1}{\pi\ell^2 L_y^2}\right)^{1/4}\frac{1}{\sqrt{2^n n!}}$. Making the substitution $t = x/\ell - i(q_x - iX/\ell^2 - iX'/\ell^2)\ell/2 \equiv x/\ell - A$, and noting that $\int ds\ e^{-s^2}H_m(s+y)H_j(s+z) = 2^m\sqrt{\pi}j!z^{m-j}L_j^{m-j}(-2yz)$ for $m \geq j$,

$$
\begin{aligned}
&\int d\boldsymbol{r}\ e^{i\boldsymbol{q}\cdot\boldsymbol{r}}h^*_{m,k}(\boldsymbol{r})h_{j,k'}(\boldsymbol{r}) \\
&= \ell\ C_m C_j L_y\ \delta_{k,k'-q_y}e^{iq_x(X+X')/2}e^{-q^2\ell^2/4}\int_{-\infty}^{\infty}dt\ e^{-t^2}H_m\left(\frac{\ell(t+A)-X}{\ell}\right)H_j\left(\frac{\ell(t+A)-X'}{\ell}\right) \\
&= \ell\ C_m C_j L_y\ \delta_{k,k'-q_y}e^{iq_x(X+X')/2}e^{-q^2\ell^2/4}\ 2^m\sqrt{\pi}j!\left[iq_x\ell/2 - q_y\ell/2)\right]^{m-j}L_j^{m-j}(q^2\ell^2/2) \\
&= \delta_{k,k'-q_y}e^{iq_x(X+X')/2}\left(\frac{j!}{m!}\right)^{1/2}\left[\frac{-q_y\ell + iq_x\ell}{\sqrt{2}}\right]^{m-j}e^{-q^2\ell^2/4}L_j^{m-j}(q^2\ell^2/2) \\
&\equiv \delta_{k,k'-q_y}e^{iq_x(k+k')\ell^2/2}F_{m,j}(\boldsymbol{q}),
\end{aligned}
\tag{A.5}
$$

where

$$
F_{m,j}(q_x,q_y) = \left(\frac{j!}{m!}\right)^{1/2}\left[\frac{-q_y\ell + iq_x\ell}{\sqrt{2}}\right]^{m-j}e^{-q^2\ell^2/4}L_j^{m-j}(q^2\ell^2/2). \tag{A.6}
$$

Our next task will be to tie the form factors $F_{n,n'}(\boldsymbol{q})$ to the $T^{\tau,\tau'}_{n,n'}(\boldsymbol{q},s)$ elements. With $\tau \neq \tau'$, for the A sublattice,

$$
\begin{aligned}
&\int d\boldsymbol{r}\ \langle \boldsymbol{r}|+1;,n,k,A\rangle^*\ e^{i\boldsymbol{q}\cdot\boldsymbol{r}}\ \langle \boldsymbol{r}|-1;n',k',A\rangle \\
&\quad= -\mathrm{sgn}(n)\frac{\sqrt{2}^{\delta_{n,0}+\delta_{n',0}}}{2}\int d\boldsymbol{r}\ e^{i\boldsymbol{q}\cdot\boldsymbol{r}}h^*_{|n|-1,k}(\boldsymbol{r})h_{|n'|,k'}(\boldsymbol{r}) \\
&\quad= -\mathrm{sgn}(n)\frac{\sqrt{2}^{\delta_{n,0}+\delta_{n',0}}}{2}\delta_{k,k'-q_y}e^{iq_x(k+k')\ell^2/2}F_{|n|-1,\,|n'|}(\boldsymbol{q}) \equiv T^{1,-1}_{n,n'}(\boldsymbol{q},A)\delta_{k,k'-q_y}e^{iq_x(k+k')\ell^2/2}, \\
&\int d\boldsymbol{r}\ \langle \boldsymbol{r}|-1;,n,k,A\rangle^*\ e^{i\boldsymbol{q}\cdot\boldsymbol{r}}\ \langle \boldsymbol{r}|+1;n',k',A\rangle \\
&\quad= -\mathrm{sgn}(n')\frac{\sqrt{2}^{\delta_{n,0}+\delta_{n',0}}}{2}\int d\boldsymbol{r}\ e^{i\boldsymbol{q}\cdot\boldsymbol{r}}h^*_{|n|,k}(\boldsymbol{r})h_{|n'|-1,k'}(\boldsymbol{r}) \\
&\quad= -\mathrm{sgn}(n')\frac{\sqrt{2}^{\delta_{n,0}+\delta_{n',0}}}{2}\delta_{k,k'-q_y}e^{iq_x(k+k')\ell^2/2}F_{|n|,\,|n'|-1}(\boldsymbol{q}) \equiv T^{-1,1}_{n,n'}(\boldsymbol{q},A)\delta_{k,k'-q_y}e^{iq_x(k+k')\ell^2/2}.
\end{aligned}
\tag{A.7}
$$

For the B sublattice,

$$\begin{aligned}
&\int d\boldsymbol{r}\,\langle \boldsymbol{r}|+1;,n,k,B\rangle^{*}\, e^{i\boldsymbol{q}\cdot\boldsymbol{r}}\,\langle \boldsymbol{r}|-1;n',k',B\rangle \\
&\quad=\mathrm{sgn}(n')\frac{\sqrt{2}^{\delta_{n,0}+\delta_{n',0}}}{2}\int d\boldsymbol{r}\;e^{i\boldsymbol{q}\cdot\boldsymbol{r}}h^{*}_{|n|,k}(\boldsymbol{r})h_{|n'|-1,k'}(\boldsymbol{r}) \\
&\quad=\mathrm{sgn}(n')\frac{\sqrt{2}^{\delta_{n,0}+\delta_{n',0}}}{2}\delta_{k,k'-q_y}e^{iq_x(k+k')\ell^2/2}F_{|n|,\,|n'|-1}(\boldsymbol{q})\equiv T^{1,-1}_{n,n'}(\boldsymbol{q},B)\delta_{k,k'-q_y}e^{iq_x(k+k')\ell^2/2}, \\
&\int d\boldsymbol{r}\,\langle \boldsymbol{r}|-1;,n,k,B\rangle^{*}\, e^{i\boldsymbol{q}\cdot\boldsymbol{r}}\,\langle \boldsymbol{r}|+1;n',k',B\rangle \\
&\quad=\mathrm{sgn}(n)\frac{\sqrt{2}^{\delta_{n,0}+\delta_{n',0}}}{2}\int d\boldsymbol{r}\;e^{i\boldsymbol{q}\cdot\boldsymbol{r}}h^{*}_{|n|-1,k}(\boldsymbol{r})h_{|n'|,k'}(\boldsymbol{r}) \\
&\quad=\mathrm{sgn}(n)\frac{\sqrt{2}^{\delta_{n,0}+\delta_{n',0}}}{2}\delta_{k,k'-q_y}e^{iq_x(k+k')\ell^2/2}F_{|n|-1,\,|n'|}(\boldsymbol{q})\equiv T^{-1,1}_{n,n'}(\boldsymbol{q},B)\delta_{k,k'-q_y}e^{iq_x(k+k')\ell^2/2}.
\end{aligned}\tag{A.8}$$

With $\tau=\tau'$, for the A sublattice,

$$\begin{aligned}
&\int d\boldsymbol{r}\,\langle \boldsymbol{r}|+1;,n,k,A\rangle^{*}\, e^{i\boldsymbol{q}\cdot\boldsymbol{r}}\,\langle \boldsymbol{r}|+1;n',k',A\rangle \\
&=\mathrm{sgn}(nn')\frac{\sqrt{2}^{\delta_{n,0}+\delta_{n',0}}}{2}\delta_{k,k'-q_y}e^{iq_x(k+k')\ell^2/2}F_{|n|-1,\,|n'|-1}(q_x,q_y)\equiv T^{1,1}_{n,n'}(\boldsymbol{q},A)\delta_{k,k'-q_y}e^{iq_x(k+k')\ell^2/2}, \\
&\int d\boldsymbol{r}\,\langle \boldsymbol{r}|-1;,n,k,A\rangle^{*}\, e^{i\boldsymbol{q}\cdot\boldsymbol{r}}\,\langle \boldsymbol{r}|-1;n',k',A\rangle \\
&\quad=\frac{\sqrt{2}^{\delta_{n,0}+\delta_{n',0}}}{2}\delta_{k,k'-q_y}e^{iq_x(k+k')\ell^2/2}F_{|n|,\,|n'|}(q_x,q_y)\equiv T^{-1,-1}_{n,n'}(\boldsymbol{q},A)\delta_{k,k'-q_y}e^{iq_x(k+k')\ell^2/2}.
\end{aligned}\tag{A.9}$$

For the B sublattice,

$$\begin{aligned}
&\int d\boldsymbol{r}\,\langle \boldsymbol{r}|+1;,n,k,B\rangle^{*}\, e^{i\boldsymbol{q}\cdot\boldsymbol{r}}\,\langle \boldsymbol{r}|+1;n',k',B\rangle \\
&\quad=\frac{\sqrt{2}^{\delta_{n,0}+\delta_{n',0}}}{2}\delta_{k,k'-q_y}e^{iq_x(k+k')\ell^2/2}F_{|n|,\,|n'|}(\boldsymbol{q})\equiv T^{1,1}_{n,n'}(\boldsymbol{q},B)\delta_{k,k'-q_y}e^{iq_x(k+k')\ell^2/2}, \\
&\int d\boldsymbol{r}\,\langle \boldsymbol{r}|-1;,n,k,B\rangle^{*}\, e^{i\boldsymbol{q}\cdot\boldsymbol{r}}\,\langle \boldsymbol{r}|-1;n',k',B\rangle \\
&=\mathrm{sgn}(nn')\frac{\sqrt{2}^{\delta_{n,0}+\delta_{n',0}}}{2}\delta_{k,k'-q_y}e^{iq_x(k+k')\ell^2/2}F_{|n|-1,\,|n'|-1}(\boldsymbol{q})\equiv T^{-1,-1}_{n,n'}(\boldsymbol{q},B)\delta_{k,k'-q_y}e^{iq_x(k+k')\ell^2/2}.
\end{aligned}\tag{A.10}$$

Appendix B

Effective Interactions of Dirac Sea electrons

B.1 Coulomb interactions in the sea

In this section, we work out the contributions from the Dirac sea for the Coulomb, OS, and NN interactions. Beginning with the Coulomb interaction, we have

$$\begin{aligned}
\mathcal{T}^{(\mathrm{C})}_{\mathrm{sea}}(n_2,n_4) &\equiv \sum_{n=-n_c}^{-n_w-1} \mathcal{T}^{(\mathrm{C})}(n,n_2,n,n_4) \\
&= D(n,n_2,n,n_4)\Big[I^{(\mathrm{C})}\big(|n|\,,|n_2|\,,|n|\,,|n_4|\,\big) \\
&\qquad +\mathrm{sgn}(nn_4) I^{(\mathrm{C})}\big(|n|-1,|n_2|\,,|n|\,,|n_4|-1\big) \\
&\qquad +\mathrm{sgn}(n_2 n) I^{(\mathrm{C})}\big(|n|\,,|n_2|-1,|n|-1,|n_4|\,\big) \\
&\qquad +\mathrm{sgn}(n_2 n_4 n^2) I^{(\mathrm{C})}\big(|n|-1,|n_2|-1,|n|-1,|n_4|-1\big)\Big],
\end{aligned} \tag{B.1}$$

where eq. (2.48) has been inserted into the first line above. Recall that $I^{(\mathrm{C})}(|n_1|\,,|n_2|\,,|n_3|\,,|n_4|) \propto \delta_{|n_1|-|n_4|,|n_3|-|n_2|}$ (eq. (2.40)), which will appear in the same form in all the terms above, regardless of how the LL index is shifted. Since $n_1 = n_3$, we must then have $|n_2| = |n_4|$ from this delta function constraint in all terms appearing above. This gives three possibilities: 1) $n_2 n_4 < 0$, 2) $n_2 n_4 > 0$, or 3) $n_2 = n_4 = 0$. Also, note that $n < 0$ in every term in the sum, since that index refers to LL's in the sea. For $n_2 n_4 < 0$, either $n_2 > 0$ and $n_4 < 0$, or $n_2 < 0$ and $n_4 > 0$. We can summarize both

of these subcases by writing

$$\mathcal{T}^{(\mathrm{C})}_{\mathrm{sea}}(n_2,n_4)=\sum_{n=-n_c}^{-n_w-1}D(n,n_2,n,n_4)\Big[I^{(\mathrm{C})}(|n|\,,|n_2|\,,|n|\,,|n_4|)$$
$$\pm I^{(\mathrm{C})}(|n|-1,|n_2|\,,|n|\,,|n_4|-1)$$
$$\mp I^{(\mathrm{C})}(|n|\,,|n_2|-1,|n|-1,|n_4|)$$
$$-I^{(\mathrm{C})}(|n|-1,|n_2|-1,|n|-1,|n_4|-1)\Big] \tag{B.2}$$
$$=\frac{\sqrt{2}e^2}{4\ell}\sum_{n=-n_c}^{-n_w-1}D(n,n_2,n,n_4)$$
$$\times\Big[J^{\left||n'|-|n|\right|}_{\min(|n'|,|n|),\min(|n'|,|n|)}\pm J^{\left||n'|-|n|\right|}_{\min(|n'|,|n|),\min(|n'|-1,|n|-1)}$$
$$\mp J^{\left||n'|-|n|\right|}_{\min(|n'|-1,|n|-1),\min(|n'|,|n|)}-J^{\left||n'|-|n|\right|}_{\min(|n'|-1,|n|-1),\min(|n'|-1,|n|-1)}\Big]\delta_{|n_2|,|n_4|},$$

where $\left|n'\right|=|n_2|=|n_4|$, and eq. (2.40) has been used. Note that $\left|n'\right|<|n|$, since n_2 and n_4 refer to LL indices in the active window. Using the fact that $J^{\alpha}_{n,m}=J^{\alpha}_{m,n}$, and $D(\boldsymbol{n}\neq 0)=\frac{1}{4}$ (eq. (2.30)), the above expression reduces to

$$\mathcal{T}^{(\mathrm{C})}_{\mathrm{sea}}(n_2,n_4)=\frac{\sqrt{2}e^2}{16\ell}\sum_{n=-n_c}^{-n_w-1}\Big[J^{|n|-|n'|}_{|n'|,|n'|}-J^{|n|-|n'|}_{|n'|-1,|n'|-1}\Big]\delta_{|n_2|,|n_4|}\ \text{if}\ \ n_2n_4<0. \tag{B.3}$$

For $n_2n_4>0$, we have either $n_2=n_4>0$ or $n_2=n_4<0$. For either of these two subcases, the second and third terms of eq. (B.1) will add together. The result in this case is

$$\mathcal{T}^{(\mathrm{C})}_{\mathrm{sea}}(n_2,n_4)=\frac{\sqrt{2}e^2}{16\ell}\sum_{n=-n_c}^{-n_w-1}\Big[J^{|n|-|n'|}_{|n'|,|n'|}-\mathrm{sgn}(n')\ 2J^{|n|-|n'|}_{|n'|-1,|n'|}-J^{|n|-|n'|}_{|n'|-1,|n'|-1}\Big]\delta_{|n_2|,|n_4|}\ \text{if}\ \ n_2n_4>0, \tag{B.4}$$

where $n'=n_2=n_4$. The final case is when $n_2=n_4=0$. In that case, only the first term in eq. (B.1) remains. Noting that $D(n,0,n,0)=\frac{1}{2}$, we have

$$\mathcal{T}^{(\mathrm{C})}_{\mathrm{sea}}(n_2=0,n_4=0)=\frac{\sqrt{2}e^2}{8\ell}\sum_{n=-n_c}^{-n_w-1}J^{|n|}_{0,0}. \tag{B.5}$$

We can summarize these results by writing

$$\mathcal{T}^{(\mathrm{C})}_{\mathrm{sea}}(n_2,n_4)=\frac{\sqrt{2}e^2}{4\ell}\sum_{n=-n_c}^{-n_w-1}\delta_{|n_2|,|n_4|}A(n_2,n_4,n), \tag{B.6}$$

with $A(n_2,n_4,n)$ given by eq. (2.54).

B.2 On-site and nearest neighbor interactions in the sea

Next, the OS and NN sea contributions are worked out. In the HF Hamiltonian, eq. (2.49), we have

$$\begin{aligned}&+\sum_{\boldsymbol{n},\boldsymbol{\tau}}\delta_{\tau_1-\tau_4,\tau_3-\tau_2}\left[\mathcal{T}_{\mathrm{D}}^{(\mathrm{OS})}(\boldsymbol{n},\boldsymbol{\tau})+\mathcal{T}_{\mathrm{D}}^{(\mathrm{NN})}(\boldsymbol{n},\boldsymbol{\tau})\right]\sum_{\sigma,\sigma'}\langle c^{\dagger}_{\sigma'\tau_1 n_1}c_{\sigma'\tau_4 n_4}\rangle\, c^{\dagger}_{\sigma\tau_2 n_2}c_{\sigma\tau_3 n_3}\\&-\sum_{\boldsymbol{n},\boldsymbol{\tau}}\delta_{\tau_1-\tau_4,\tau_3-\tau_2}\left[\mathcal{T}_{\mathrm{X}}^{(\mathrm{OS})}(\boldsymbol{n},\boldsymbol{\tau})+\mathcal{T}_{\mathrm{X}}^{(\mathrm{NN})}(\boldsymbol{n},\boldsymbol{\tau})\right]\sum_{\sigma,\sigma'}\langle c^{\dagger}_{\sigma\tau_1 n_1}c_{\sigma'\tau_3 n_3}\rangle\, c^{\dagger}_{\sigma'\tau_2 n_2}c_{\sigma\tau_4 n_4}.\end{aligned}\tag{B.7}$$

In what follows, we use the result for the OS and NN exchange integrals, eq. (2.42) and eq. (2.43), and define their direct counterparts, which are essentially given by eq. (2.45). We write

$$I_{\mathrm{X}}^{(\mathrm{OS})}(\boldsymbol{n})=\frac{V_0A_c}{8\pi\ell^2}\delta_{n_1,n_3}\delta_{n_2,n_4}\ ,\ I_{\mathrm{X}}^{(\mathrm{NN})}(\boldsymbol{n})=\frac{3V_1A_c}{8\pi\ell^2}\delta_{n_1,n_3}\delta_{n_2,n_4},\tag{B.8}$$

and

$$I_{\mathrm{D}}^{(\mathrm{OS})}(\boldsymbol{n})\equiv\frac{V_0A_c}{8\pi\ell^2}\delta_{n_1,n_4}\delta_{n_2,n_3}\ ,\ I_{\mathrm{D}}^{(\mathrm{NN})}(\boldsymbol{n})\equiv\frac{3V_1A_c}{8\pi\ell^2}\delta_{n_1,n_4}\delta_{n_2,n_3}.\tag{B.9}$$

For $\mathrm{j}=\mathrm{D},\mathrm{X}$, the $\mathcal{T}$ elements for the OS interaction, with $\tau_1=\tau_4=\tau$, $\tau_2=\tau_3=\tau'$, read as

$$\begin{aligned}\mathcal{T}_{\mathrm{j}}^{(\mathrm{OS})}(\boldsymbol{n};\tau,\tau',\tau',\tau)=D(\boldsymbol{n})\Big[&\Big(I_{\mathrm{j}}^{(\mathrm{OS})}(|n_1|,|n_2|,|n_3|,|n_4|)\\&+\mathrm{sgn}(n_1n_2n_3n_4)I_{\mathrm{j}}^{(\mathrm{OS})}(|n_1|-1,|n_2|-1,|n_3|-1,|n_4|-1)\Big)\delta_{\tau,\tau'}\\&+\Big(\mathrm{sgn}(n_1n_4)I_{\mathrm{j}}^{(\mathrm{OS})}(|n_1|-1,|n_2|,|n_3|,|n_4|-1)\\&+\mathrm{sgn}(n_2n_3)I_{\mathrm{j}}^{(\mathrm{OS})}(|n_1|,|n_2|-1,|n_3|-1,|n_4|)\Big)\delta_{\tau,-\tau'}\Big],\end{aligned}\tag{B.10}$$

and, for $\tau=\tau_1=\tau_3\neq\tau_2=\tau_4=\tau'$,

$$\begin{aligned}\mathcal{T}_{\mathrm{j}}^{(\mathrm{OS})}(\boldsymbol{n};\tau,\tau',\tau,\tau')=D(\boldsymbol{n})\Big[&\mathrm{sgn}(n_2n_4)I_{\mathrm{j}}^{(\mathrm{OS})}(|n_1|,|n_2|-1,|n_3|,|n_4|-1)\\&+\mathrm{sgn}(n_1n_3)I_{\mathrm{j}}^{(\mathrm{OS})}(|n_1|-1,|n_2|,|n_3|-1,|n_4|)\Big].\end{aligned}\tag{B.11}$$

For the NN term, the components with $\tau_1 = \tau_4$, $\tau_2 = \tau_3$ are

$$\begin{aligned}\mathcal{T}_{\rm j}^{(\rm NN)}(\boldsymbol{n};\tau,\tau',\tau',\tau) = D(\boldsymbol{n})\Bigg[\Bigg(&I_{\rm j}^{(\rm NN)}(|n_1|,|n_2|,|n_3|,|n_4|)\\ &+\mathrm{sgn}(n_1n_2n_3n_4)I_{\rm j}^{(\rm NN)}(|n_1|-1,|n_2|-1,|n_3|-1,|n_4|-1)\Bigg)\delta_{\tau,-\tau'}\\ &+\Bigg(\mathrm{sgn}(n_1n_4)I_{\rm j}^{(\rm NN)}(|n_1|-1,|n_2|,|n_3|,|n_4|-1)\\ &+\mathrm{sgn}(n_2n_3)I_{\rm j}^{(\rm NN)}(|n_1|,|n_2|-1,|n_3|-1,|n_4|)\Bigg)\delta_{\tau,\tau'}\Bigg].\end{aligned} \tag{B.12}$$

For the case when $\tau_1 = \tau_3 \neq \tau_2 = \tau_4$, we have

$$\begin{aligned}\mathcal{T}_{\rm j}^{(\rm NN)}(\boldsymbol{n};\tau,\tau',\tau,\tau') = -D(\boldsymbol{n})\Bigg[&\mathrm{sgn}(n_3n_4)I_{\rm j}^{(\rm NN)}(|n_1|,|n_2|,|n_3|-1,|n_4|-1)\\ &+\mathrm{sgn}(n_1n_2)I_{\rm j}^{(\rm NN)}(|n_1|-1,|n_2|-1,|n_3|,|n_4|)\Bigg],\end{aligned} \tag{B.13}$$

with $\tau \neq \tau'$.

Using the condition on states in the filled sea, eq. (2.51), the OS and NN interactions generate a term in the HF Hamiltonian of the form

$$\begin{aligned}&\mathcal{H}_{\rm HF,sea}^{(\rm OS)} + \mathcal{H}_{\rm HF,sea}^{(\rm NN)} =\\ &\quad 2\sum_{n_2,n_3=-n_w}^{n_w}\sum_{\boldsymbol{\tau}}\delta_{\tau_1,\tau_4}\delta_{\tau_2,\tau_3}\sum_{n=-n_c}^{-n_w-1}\Big[\mathcal{T}_{\rm D}^{(\rm OS)}(n,n_2,n_3,n;\boldsymbol{\tau}) + \mathcal{T}_{\rm D}^{(\rm NN)}(n,n_2,n_3,n;\boldsymbol{\tau})\Big]\\ &\quad\times\sum_{\sigma} c^\dagger_{\sigma\tau_2n_2}c_{\sigma\tau_3n_3}\\ &\quad -\sum_{n_2,n_4=-n_w}^{n_w}\sum_{\boldsymbol{\tau}}\delta_{\tau_2,\tau_4}\delta_{\tau_1,\tau_3}\sum_{n=-n_c}^{-n_w-1}\Big[\mathcal{T}_{\rm X}^{(\rm OS)}(n,n_2,n,n_4;\boldsymbol{\tau}) + \mathcal{T}_{\rm X}^{(\rm NN)}(n,n_2,n,n_4;\boldsymbol{\tau})\Big]\\ &\quad\times\sum_{\sigma} c^\dagger_{\sigma\tau_2n_2}c_{\sigma\tau_4n_4}.\end{aligned} \tag{B.14}$$

We again use n for the label on the Dirac sea LL, and note that, if n' is a LL in the active window, $|n'| < |n|$. In the last line of eq. (B.14), for the case when $\tau_1 = \tau_3, \tau_2 = \tau_4$,

$$\mathcal{T}_{\rm X}^{(\rm NN)}(n,n_2,n,n_4;\tau,\tau',\tau,\tau') = 0, \tag{B.15}$$

since $\delta_{|n|,\,|n|-1} = 0$. Tracing over the two pseudospin indices gives

$$\begin{aligned}\mathcal{H}^{(\mathrm{OS})}_{\mathrm{HF,sea}} + \mathcal{H}^{(\mathrm{NN})}_{\mathrm{HF,sea}} = \\ 2 \sum_{n_2,n_3=-n_w}^{n_w} \sum_{\tau,\tau'} \sum_{n=-n_c}^{-n_w-1} \Big[\mathcal{T}^{(\mathrm{OS})}_{\mathrm{D}}(n,n_2,n_3,n;\tau,\tau',\tau',\tau) + \mathcal{T}^{(\mathrm{NN})}_{\mathrm{D}}(n,n_2,n_3,n;\tau,\tau',\tau',\tau)\Big] \\ \times \sum_{\sigma} c^{\dagger}_{\sigma\tau' n_2} c_{\sigma\tau' n_3} \\ - \sum_{n_2,n_4=-n_w}^{n_w} \sum_{\tau,\tau'} \sum_{n=-n_c}^{-n_w-1} \mathcal{T}^{(\mathrm{OS})}_{\mathrm{X}}(n,n_2,n,n_4;\tau,\tau',\tau,\tau') \sum_{\sigma} c^{\dagger}_{\sigma\tau' n_2} c_{\sigma\tau' n_4}.\end{aligned} \tag{B.16}$$

In eq. (B.10), notice that

$$\begin{aligned}\mathcal{T}^{(\mathrm{OS})}_{\mathrm{D}}(n,n_2,n_3,n;\tau,\tau',\tau',\tau=\tau') &= \mathcal{T}^{(\mathrm{OS})}_{\mathrm{D}}(n,n_2,n_3,n;\tau,\tau',\tau',\tau\neq\tau') \\ &= \frac{V_0 A_c}{8\pi\ell^2} D(n,n_2,n_3,n)\big[1+\mathrm{sgn}(n_2 n_3)\big]\delta_{|n_2|,\,|n_3|}\end{aligned} \tag{B.17}$$

and, from eq. (B.12),

$$\begin{aligned}\mathcal{T}^{(\mathrm{NN})}_{\mathrm{D}}(n,n_2,n_3,n;\tau,\tau',\tau',\tau=\tau') &= \mathcal{T}^{(\mathrm{NN})}_{\mathrm{D}}(n,n_2,n_3,n;\tau,\tau',\tau',\tau\neq\tau') \\ &= \frac{3V_1 A_c}{8\pi\ell^2} D(n,n_2,n_3,n)\big[1+\mathrm{sgn}(n_2 n_3)\big]\delta_{|n_2|,\,|n_3|}.\end{aligned} \tag{B.18}$$

Finally, from eq. (B.11), and the term accompanying $\delta_{\tau,\tau'}$ in eq. (B.10), notice that

$$\begin{aligned}\mathcal{T}^{(\mathrm{OS})}_{\mathrm{X}}(n,n_2,n,n_4;\tau,\tau',\tau,\tau'=\tau) &= \mathcal{T}^{(\mathrm{OS})}_{\mathrm{D}}(n,n_2,n,n_4;\tau,\tau',\tau,\tau'\neq\tau) \\ &= \frac{V_0 A_c}{8\pi\ell^2} D(n,n_2,n,n_4)\big[1+\mathrm{sgn}(n_2 n_4)\big]\delta_{|n_2|,\,|n_4|}.\end{aligned} \tag{B.19}$$

We now see that the form of every $\mathcal{T}$ element appearing in eq. (B.16) is independent of whether $\tau' = 1$ or $\tau' = -1$. Relabeling LL indices $n_3 \leftrightarrow n_4$, and summing over τ, eq. (B.16) becomes

$$\begin{aligned}\mathcal{H}^{(\mathrm{OS})}_{\mathrm{HF,sea}} + \mathcal{H}^{(\mathrm{NN})}_{\mathrm{HF,sea}} = \\ \frac{A_c}{4\pi\ell^2}\big(V_0+6V_1\big) \sum_{n_2,n_3=-n_w}^{n_w} \sum_{n=-n_c}^{-n_w-1} D(n,n_2,n_3,n)\big(1+\mathrm{sgn}(n_2 n_3)\big)\delta_{|n_2|,\,|n_3|} \sum_{\sigma,\tau'} c^{\dagger}_{\sigma\tau' n_2} c_{\sigma\tau' n_3},\end{aligned} \tag{B.20}$$

where we have used the fact that $D(n,n_2,n,n_3) = D(n,n_2,n_3,n)$. If $n_2 n_3 < 0$, the whole term vanishes completely. Noting that $D(n,0,0,n) = \frac{1}{2}$ and $D(\boldsymbol{n}\neq 0) = \frac{1}{4}$, the OS and NN Dirac sea contributions yield

$$\mathcal{H}^{(\mathrm{OS})}_{\mathrm{HF,sea}} + \mathcal{H}^{(\mathrm{NN})}_{\mathrm{HF,sea}} = \frac{A_c}{8\pi\ell^2}\big(V_0+6V_1\big) N_{\mathrm{sea}} \sum_{\sigma,\tau,n} c^{\dagger}_{\sigma\tau n} c_{\sigma\tau n}, \tag{B.21}$$

where N_{sea} is the number of LL's in the Dirac sea. Thus, the OS and NN sea contributions are diagonal in all state indices.

Appendix C

Exchange Integrals

In this section, we work out the exchange integrals that appear in the HF Hamiltonian for non-uniform states. From eq. (4.9), we have

$$\begin{aligned}\mathcal{T}_{\rm X}^{(\rm i)}(\boldsymbol{n},\boldsymbol{\tau},\boldsymbol{q}) &= \frac{1}{S}\sum_{\boldsymbol{p}} e^{i\boldsymbol{p}\times\boldsymbol{q}\ell^2}\mathcal{M}^{(\rm i)}(\boldsymbol{n},\boldsymbol{\tau},\boldsymbol{p}) \\ &= \int \frac{d^2p}{(2\pi)^2} e^{i\boldsymbol{p}\times\boldsymbol{q}\ell^2}\mathcal{M}^{(\rm i)}(\boldsymbol{n},\boldsymbol{\tau},\boldsymbol{p}),\end{aligned} \tag{C.1}$$

for each interaction, i = C, OS. Recall that the $\mathcal{M}$ functions, defined in eq. (2.27), are written as a sum of products of form factors. Therefore, the integrals are essentially of form

$$I^{(\rm i)}(n,m,k,j;\boldsymbol{q}) \equiv \int \frac{d^2p}{(2\pi)^2} e^{i\boldsymbol{p}\times\boldsymbol{q}\ell^2} F_{n,m}(\boldsymbol{p})F_{k,j}(-\boldsymbol{p})\nu^{(\rm i)}(p), \tag{C.2}$$

where $n \geq m \geq 0$ and $k \geq j \geq 0$ are positive integers referring to the LL indices ($n_1 = n, n_4 = m, n_2 = k,$ and $n_3 = j$). For each interaction, $\nu^{(\rm OS)}(p) = \frac{V_0 A_c}{4}$ and $\nu^{(\rm C)}(p) = \frac{2\pi e^2}{4p}$. Inserting eq. (2.26) for the form factors, F, into the above expression, with $\tan\theta = p_y/p_x$, gives

$$\begin{aligned} I^{(\rm i)}(n,m,k,j;\boldsymbol{q}) = & \\ &\left(\frac{m!j!}{n!k!}\right)^{1/2}\int \frac{d^2p}{(2\pi)^2}\nu^{(\rm i)}(p)e^{i\boldsymbol{p}\times\boldsymbol{q}\ell^2}e^{-p^2\ell^2/2} \\ &\qquad\times L_m^{n-m}(p^2\ell^2/2)L_j^{k-j}(p^2\ell^2/2)\left[\frac{-p_y\ell+ip_x\ell}{\sqrt{2}}\right]^{n-m}\left[\frac{p_y\ell-ip_x\ell}{\sqrt{2}}\right]^{k-j} \\ &= \left(\frac{m!j!}{n!k!}\right)^{1/2}(-1)^{k-j}\left(\frac{i\ell}{\sqrt{2}}\right)^{n-m+k-j} \\ &\qquad\times\int_0^\infty dp\ \nu^{(\rm i)}(p)\ p^{n-m+k-j+1}e^{-p^2\ell^2/2}L_m^{n-m}(p^2\ell^2/2)L_j^{k-j}(p^2\ell^2/2) \\ &\qquad\times\int_0^{2\pi}\frac{d\theta}{(2\pi)^2}e^{ip[q_y\cos\theta-q_x\sin\theta]\ell^2}e^{i\theta(n-m+k-j)}. \end{aligned} \tag{C.3}$$

With $q_x \equiv q\cos\beta$, $q_y \equiv q\sin\beta$, and $a \equiv n-m+k-j$, the angular integral becomes

$$\begin{aligned}\int_0^{2\pi}\frac{d\theta}{(2\pi)^2}e^{ip[q_y\cos\theta-q_x\sin\theta]\ell^2}e^{i\theta(n-m+k-j)} &= \int_0^{2\pi}\frac{d\theta}{(2\pi)^2}e^{i[-pq\sin(\beta-\theta)\ell^2+\theta a]}\\ &= e^{i\beta a}\int_0^{2\pi}\frac{du}{(2\pi)^2}e^{i[ua-pq\ell^2\sin u]}\\ &= \frac{e^{i\beta a}}{2\pi}J_a(pq\ell^2),\end{aligned} \tag{C.4}$$

where $J_a(x)$ are the Bessel functions of the first kind. Eq. (C.3) is now written as

$$\begin{aligned}I^{(\mathrm{i})}(n,m,k,j;\boldsymbol{q}) =& \left(\frac{m!j!}{n!k!}\right)^{1/2}\frac{(-1)^{k-j}}{2\pi}\left(\frac{i\ell}{\sqrt{2}}\right)^a e^{i\beta a}\\ &\times\int_0^\infty dp\ \nu^{(\mathrm{i})}(p)\ p^{a+1}e^{-p^2\ell^2/2}L_m^{n-m}(p^2\ell^2/2)L_j^{k-j}(p^2\ell^2/2)J_a(pq\ell^2).\end{aligned} \tag{C.5}$$

The radial integral for the on-site potential (i = OS) can be done analytically. The result is

$$\begin{aligned}&I^{(\mathrm{OS})}(n,m,k,j;\boldsymbol{q}) =\\ &\qquad\frac{V_0A_c}{8\pi\ell^2}\left(\frac{m!j!}{n!k!}\right)^{1/2}(-1)^{m+k}i^a e^{i\beta a}\left(\frac{q\ell}{\sqrt{2}}\right)^a e^{-q^2\ell^2/2}L_m^{n-j}(q^2\ell^2/2)L_j^{k-m}(q^2\ell^2/2).\end{aligned} \tag{C.6}$$

For the Coulomb potential (i = C), we have

$$\begin{aligned}&I^{(\mathrm{C})}(n,m,k,j;\boldsymbol{q}) =\\ &\qquad\frac{\sqrt{2}e^2}{4\ell}\left(\frac{m!j!}{n!k!}\right)^{1/2}(-1)^{k-j}i^a e^{i\beta a}\int_0^\infty dx\ x^a e^{-x^2}L_m^{n-m}(x^2)L_j^{k-j}(x^2)J_a(\sqrt{2}q\ell x),\end{aligned} \tag{C.7}$$

where the remaining integral is computed numerically.

Appendix D

Matsubara Formalism

The fermionic Matsubara Green's function with an arbitrary set of state labels, α, β, is

$$\mathcal{G}(\alpha, \beta; \bar{\tau}) \equiv - \langle T_{\bar{\tau}} c_\alpha(\bar{\tau}) c^\dagger_\beta(0) \rangle \,, \tag{D.1}$$

where T_τ is the time ordering operator and $\bar{\tau}$ has dimensions of time. Defining the step function,

$$\theta(\bar{\tau}) = \begin{cases} 0 & \bar{\tau} < 0 \\ \frac{1}{2} & \bar{\tau} = 0 \\ 1 & \bar{\tau} > 0, \end{cases} \tag{D.2}$$

and noting that $\theta(-\bar{\tau}) = 1 - \theta(\bar{\tau})$, we can write the Green's function as

$$\begin{aligned} \mathcal{G}(\alpha, \beta; \bar{\tau}) &= -\theta(\bar{\tau}) \langle c_\alpha(\bar{\tau}) c^\dagger_\beta(0) \rangle + \theta(-\bar{\tau}) \langle c^\dagger_\beta(0) c_\alpha(\bar{\tau}) \rangle \\ &= -\theta(\bar{\tau}) \big[\langle c_\alpha(\bar{\tau}) c^\dagger_\beta(0) \rangle + \langle c^\dagger_\beta(0) c_\alpha(\bar{\tau}) \rangle \big] + \langle c^\dagger_\beta(0) c_\alpha(\bar{\tau}) \rangle \,. \end{aligned} \tag{D.3}$$

Differentiating with respect to $\bar{\tau}$ gives

$$\frac{\partial G(\alpha, \beta; \bar{\tau})}{\partial \bar{\tau}} = -\delta(\bar{\tau}) \delta_{\alpha,\beta} - \left\langle T_\tau \frac{\partial c_\alpha}{\partial \bar{\tau}} c^\dagger_\beta(0) \right\rangle , \tag{D.4}$$

and using the Heisenberg equation of motion, $\frac{\partial c_\alpha}{\partial \bar{\tau}} = [\mathcal{H} - \mu N, c_\alpha]$, we now have

$$\frac{\partial \mathcal{G}(\alpha, \beta; \bar{\tau})}{\partial \bar{\tau}} = -\delta(\bar{\tau}) \delta_{\alpha,\beta} - \left\langle T_{\bar{\tau}} [\mathcal{H} - \mu N, c_\alpha](\bar{\tau}) c^\dagger_\beta(0) \right\rangle , \tag{D.5}$$

where μ is the chemical potential, and $N = c^\dagger_\alpha c_\alpha$ is the number operator. We assume, for now, a generic form of the Hamiltonian, expressed in an arbitrary non-diagonal basis,

$$\mathcal{H} - \mu N = \sum_{\gamma_1, \gamma_2} h_{\gamma_1 \gamma_2} c^\dagger_{\gamma_1} c_{\gamma_2} + \sum_{\boldsymbol{\gamma}} V_{\gamma_1 \gamma_2 \gamma_3 \gamma_4} c^\dagger_{\gamma_1} c^\dagger_{\gamma_2} c_{\gamma_3} c_{\gamma_4}. \tag{D.6}$$

In eq. (D.6), $h_{\gamma_1 \gamma_2} = h^0_{\gamma_1 \gamma_2} - \mu \delta_{\gamma_1, \gamma_2}$, where $h^0_{\gamma_1 \gamma_2}$ is the non-interacting Hamiltonian, and $V_{\gamma_1 \gamma_2 \gamma_3 \gamma_4}$ are the elements of the two-body interaction. By using commutation properties for fermions, it can

be shown that

$$[\mathcal{H} - \mu N, c_\alpha] = -\sum_{\gamma_2} h_{\alpha\gamma_2} c_{\gamma_2} - \sum_{\gamma,\gamma_3,\gamma_4} \big(V_{\alpha\gamma\gamma_3\gamma_4} - V_{\gamma\alpha\gamma_3\gamma_4}\big) c^\dagger_\gamma c_{\gamma_3} c_{\gamma_4}, \tag{D.7}$$

so that eq. (D.5) becomes

$$\begin{aligned}\frac{\partial \mathcal{G}(\alpha,\beta;\bar\tau)}{\partial \bar\tau} = -\delta_{\alpha,\beta}\delta(\bar\tau) &+ \sum_{\gamma_2} h_{\alpha\gamma_2} \left\langle T_{\bar\tau} c_{\gamma_2}(\bar\tau) c^\dagger_\beta(0)\right\rangle \\ &+ \sum_{\gamma,\gamma_3,\gamma_4} \big(V_{\alpha\gamma\gamma_3\gamma_4} - V_{\gamma\alpha\gamma_3\gamma_4}\big) \left\langle T_{\bar\tau} c^\dagger_\gamma(\bar\tau) c_{\gamma_3}(\bar\tau) c_{\gamma_4}(\bar\tau) c^\dagger_\beta(0)\right\rangle .\end{aligned} \tag{D.8}$$

We use a Wick decomposition on the time-ordered two-particle expectation value, in the last line of eq. (D.8), to write

$$\left\langle T_{\bar\tau} c^\dagger_\gamma(\bar\tau) c_{\gamma_3}(\bar\tau) c_{\gamma_4}(\bar\tau) c^\dagger_\beta(0)\right\rangle \approx \left\langle c^\dagger_\gamma(\bar\tau) c_{\gamma_3}(\bar\tau)\right\rangle \left\langle T_{\bar\tau} c_{\gamma_4}(\bar\tau) c^\dagger_\beta(0)\right\rangle - \left\langle c^\dagger_\gamma(\bar\tau) c_{\gamma_4}(\bar\tau)\right\rangle \left\langle T_{\bar\tau} c_{\gamma_3}(\bar\tau) c^\dagger_\beta(0)\right\rangle , \tag{D.9}$$

where we have assumed that the state can be written in terms of a single Slater determinant. Inserting eq. (D.9) into eq. (D.8), interchanging $\gamma_3 \leftrightarrow \gamma_4$ in the first term of the decomposition, and simultaneously relabeling $\gamma_3 \to \gamma$ and $\gamma \to \gamma_3$, we now have

$$\begin{aligned}\frac{\partial \mathcal{G}(\alpha,\beta;\bar\tau)}{\partial \bar\tau} = -\delta_{\alpha,\beta}\delta(\bar\tau) &+ \mu \mathcal{G}(\gamma,\beta;\bar\tau) \\ &- \sum_{\gamma} \left[h^0_{\alpha\gamma} + \sum_{\gamma_3\gamma_4} \big(V_{\alpha\gamma_3\gamma_4\gamma} - V_{\gamma_3\alpha\gamma_4\gamma} - V_{\alpha\gamma_3\gamma\gamma_4} + V_{\gamma_3\alpha\gamma\gamma_4}\big) \widetilde{\rho}_{\gamma_3\gamma_4} \right] \mathcal{G}(\gamma,\beta;\bar\tau),\end{aligned} \tag{D.10}$$

where $\langle c^\dagger_3 c_4\rangle(\bar\tau) \equiv \widetilde{\rho}_{34}(\bar\tau)$ is essentially the density matrix; in the analysis in the main text, we will eventually take the limit $\bar\tau \to 0$. After we take this limit, the second term in the square brackets becomes exactly the interacting Hartree-Fock matrix, $H_{\alpha\gamma}$. The Fourier transform of the Green's functions is given by

$$\mathcal{G}(\alpha,\beta;\bar\tau) = \frac{1}{\beta_T} \sum_m e^{-i\omega_m \bar\tau} \mathcal{G}(\alpha,\beta;i\omega_m), \tag{D.11}$$

where $\beta_T = \frac{1}{k_B T}$, and $\omega_n = (2n+1)\pi/\beta_T$ are the fermionic frequencies. The frequencies are found by expanding the fermion occupation functions, $n_F(\xi_{\mathbf{p}}) = (e^{\beta_T \xi_{\mathbf{p}}} + 1)^{-1}$, in a series summation over its poles and residues, with $\xi_{\mathbf{p}} = \epsilon_{\mathbf{p}} - \mu$. The poles in this expansion occur at $\xi_{\mathbf{p}} = i\omega_n$. Noting that $\delta(\bar\tau) = \frac{1}{\beta_T}\sum_n e^{-i\omega_n \tau}$, eq. (D.10) now becomes

$$\big(i\omega_n + \mu\big)\mathcal{G}(\alpha,\beta;i\omega_n) = \delta_{\alpha,\beta} + \sum_\gamma \big[h^0_{\alpha\gamma} + H_{\alpha\gamma}\big]\mathcal{G}(\gamma,\beta;i\omega_n), \tag{D.12}$$

which is eq. (4.21) in the main text.

Curriculum Vitae – Braden R. Feshami

Personal Information

Braden R. Feshami
email: bfeshami@iu.edu

Education

Ph.D. in Physics from Indiana University (Aug 2013 - Aug 2020). Thesis advisor: Herbert A. Fertig.

Bachelor of Science, double major in Physics and Applied Mathematics from University of Arizona (Aug 2007 - Jan 2013). Research advisor: Nicholas M. Ercolani.

Teaching experience

Associate Instructor at Indiana University (Aug 2013 - June 2020).
Discussion leader and lab instructor for several introductory physics courses. Six semesters as a discussion leader for Calculus I.

Publications

B. R. Feshami and H. A. Fertig, *Hartree-Fock study of the $\nu = 0$ quantum Hall state of monolayer graphene with short-range interactions*, Phys. Rev. B **94** 245435 (2016). doi:10.1103/PhysRevB.94.245435

Conference Presentations and workshops

The following presentations were focused on my Ph.D. research.

- APS March Meeting in Baltimore, 2016.
  https://meetings.aps.org/Meeting/MAR16/Session/A15.8
- APS March Meeting in Boston, 2019.
  https://meetings.aps.org/Meeting/MAR19/Session/K14.14

Attended the Summer School on Emergent Phenomena in Quantum Materials at Cornell University, Aug 2015.

Computer skills

Operating systems Advanced experience with Linux, primarily Ubuntu, and Microsoft Windows.

Servers Experience running job scripts on the Karst and BigRed II clusters at Indiana University.

Programming and scripting languages C, GNUplot, tcsh, and AWK (daily). Latex, Mathematica, Matlab, Python (Often).

Miscellaneous Experience with LAPACK, BLAS, Intel MKL, and the GNU Science Library.

Language skills

English: Native language. **German**: High-school/College level.